MANGANESE SPINELS FOR RECHARGEABLE LITHIUM BATTERIES

Haitao Huang

A Thesis Submitted for the Degree of PhD
at the
University of St Andrews

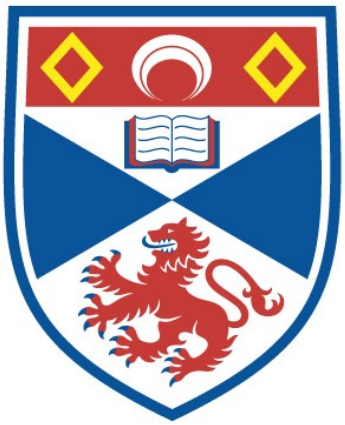

1997

Manganese Spinels for Rechargeable Lithium Batteries

A thesis presented for the degree of

Doctor of Philosophy

in the Faculty of Science of the University of St. Andrews

by

Haitao Huang, B.Sc., M.Sc.

October, 1996

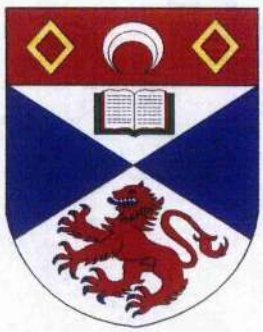

Centre for Electrochemical
and Materials Sciences
School of Chemistry
St. Andrews

ProQuest LLC.
789 East Eisenhower Parkway
P.O. Box 1346
Ann Arbor, MI 48106 – 1346

DECLARATION

I, Haitao Huang, certify that this thesis has been composed by myself, that it is a record of my own work, and has not been submitted in any previous application for a higher degree.

Signed: Date: 10/10/96

I was admitted to the Faculty of Science in the University of St. Andrews under Ordinance General No. 12 on 1 October, 1991 and as a candidate for the degree of Doctor of Philosophy on 1 October, 1992.

Signed: Date: 10/10/96

CERTIFICATION

I hereby certify that Haitao Huang, B.Sc, M.Sc, has spent twelve terms of research work under my supervision, and that she has fulfilled the conditions of the Resolution and Regulations appropriate to the degree of Doctor of Philosophy.

Signed: Date: 4/10/96

Peter G. Bruce

Director of Research

LIBRARY DECLARATION

In submitting this thesis to the University of St. Andrews, I understand that I am giving permission for it to be made available for use in accordance with regulations of the University Library for the time being in force, subject to any copyright vested in the work not being affected thereby. I also understand that the title and abstract will be published, and that a copy of the work may be made and supplied to any bona fide library or research worker.

Signed: Date: 10/10/96

ACKNOWLEDGEMENTS

I would like to thank my supervisor, Professor Peter G. Bruce, for his guidance and patience throughout my Ph.D. years. I also would like to express my appreciation to Professor Colin A. Vincent and all the members of CEMS, past and present, especially Dr. Ali Christie and Dr. Fazlil Coowar, for their many help and stimulating discussions.

My thanks must go to the technical staff at St. Andrews, whose help let me do my experimental work smoothly. In particular, Jim, Brian, Bob, and, Colin.

Particular thanks are due to Dr. John Fewster, a retired professor of biochemistry, who devoted his time to reading through the whole draft and helping me with my English.

Finally, special thanks must got to my parents, my husband and my son. Without their love and support, I could not finish my Ph.D. study.

Dedicated to Xiaolei, Lehai, and my parents

ABSTRACT

The synthesis, characterisation and performance of lithium manganese oxide spinels have been studied in terms of their application as cathode materials in rechargeable lithium batteries. A new air stable synthesis based on a solution route has been proposed. Powder X-ray diffraction demonstrates that formation of single phase spinel is possible at temperatures as low as 200 °C. Chemical analysis indicates that the compositions of the spinels prepared by the new solution route depend on the firing temperature. A temperature of 200 °C gives a composition of $LiMn_2O_{4.1}$ and the oxygen content decreases with increasing firing temperature, reaching $LiMn_2O_{4.02}$ at 600 °C and $LiMn_2O_4$ at 800 °C. TEM indicates that the solution based spinels possess small particle sizes, less than 1 μm. All these characteristics differ markedly from the highly stoichiometric and crystalline spinel prepared by traditional solid state reaction over 800 °C. Electrochemical cells based on the new spinel cathodes were constructed and subjected to galvanostatical cycling at a high discharge rate of C/2 for 300 cycles (charging at C/4). The material fired at 200 °C exhibits excellent performance at 3 V cells. An initial capacity of around 140 $mAhg^{-1}$ is obtained, very close to the theoretical capacity (148 $mAhg^{-1}$) expected for $LiMn_2O_4$. An enhancement of capacity retention by nearly 50 % after 300 cycles is obtained if < 1 wt % of carbon is added to the solution during synthesis. After 300 cycles, 64 % of the initial capacity remains. The spinel prepared by the solution route and fired at 600 °C gives excellent performance in 4 V cells. An initial capacity of 120 $mAhg^{-1}$ is obtained and around 75 % of capacity remains after 300 cycles. Ex-situ X-ray diffraction and electrochemical studies such as ac impedance and cyclic voltammetry including the use of microelectrodes were carried out to understand self-discharge and capacity loss on cycling. Spinel dissolution in the electrolyte as well as layer formed on the electrode surface may play an important part in the cycle life of the 4 V spinel cathode. The capacity loss in the 3 V cells arises from incomplete reversibility of the phase transition between cubic and tetragonal spinel which accompanies each cycle.

TABLE OF CONTENTS

CHAPTER ONE

Introduction

1-1 Rechargeable lithium batteries

1-1-1 Introduction

Batteries may be divided into two basic groups. Primary batteries are used until exhausted and then disposed of whereas secondary batteries may be recharged many times. Battery technology has a history of more than one hundred years. Well known primary batteries such as the Leclanché cell, based on Zn/MnO_2 with an ammonium chloride electrolyte, were discovered in the last century as were the lead-acid and nickel-cadmium rechargeable batteries [1, 2]. Such batteries have seen steady development throughout this century, for example the advent of alkaline Zn/MnO_2 systems, in which the solution of ammonium chloride in water is replaced by an aqueous solution of potassium hydroxide, has been an important addition to the primary battery field that was sufficient to meet the increasing demands of devices such as transistor radios in the 1970s. However, conventional batteries are facing challenges from modern electronic technologies. Advances in microelectronics have led in the 1990s to a very significant reduction in the size and weight of many portable consumer electronic products, such as mobile telephones, laptop computers and camcorders, to the point where the secondary batteries used to power them now represent a major factor limiting further product development in these multi-million dollar industries. In medicine the increasing need to develop devices such as ventricular assists (artificial heart) and active artificial limbs requires new rechargeable batteries. The demand for rechargeable electric vehicle batteries is another difficult technical challenge presented to the battery industry [3]. This can be

seen from Table 1-1-1 which indicates the requirement placed on an electric vehicle (EV) battery by USABC (US Advanced Battery Consortium), a group in USA which focus on the development of improved electric vehicle batteries. Comparison is made with the performance of present lead-acid and alternative battery systems [3]. Both present and alternative batteries do not easily match the requirement for EV.

Table 1-1-1 (quoted from [3]).

USABC battery performance goals		Battery performance goals of the US department Energy	
1995-1998	beyond 2000	Lead/acid	56 $Wh \cdot kg^{-1}$
80 $Wh \cdot Kg^{-1}$	200 $Wh \cdot Kg^{-1}$	Ni/Fe	56 $Wh \cdot kg^{-1}$
		Na/S	100 $Wh \cdot kg^{-1}$

However, the rechargeable lithium battery is a promising high power battery. It is well known that lithium is an extremely light material (6.941 $g \cdot mol^{-1}$) and hence provides very high specific capacity (3800 $Ah \cdot kg^{-1}$). Compared with the electrode materials used in conventional batteries, the capacity of the lithium electrode is 14 to 15 times higher than that of lead (260 $Ah \cdot kg^{-1}$), or 4 to 5 times higher than nickel (900 $Ah \cdot kg^{-1}$) and zinc (820 $Ah \cdot kg^{-1}$). Furthermore, lithium batteries can yield a high cell voltage because lithium is the most electropositive element (E^o = -3.04 V vs. SHE standard hydrogen electrode). Lithium batteries must use nonaqueous electrolytes, such as organic electrolytes, because of the reactivity of lithium towards water. Nonaqueous electrolytes in turn have a wider potential stability window [4] and hence allow larger cell voltage than aqueous based systems in which the thermodynamic stability range at 25 ^oC is only 1.23 V [4, 5]. For example, the output of a Ni-Cd cell is only 1.2 V, while lithium cell voltages up to 4 volts ($Li/LiCoO_2$ system) are possible depending on the cathode materials used. In general, a nonaqueous lithium cell can increase energy storage three times for the same size and weight as a Ni-Cd cells, i.e. 100-150 $Whkg^{-1}$ and 300 Whl^{-1}.

Research into lithium batteries has been going on since the 1950s. Primary lithium batteries now dominate the market in small coin cells which used to be mainly based on silver oxide technology. The primary lithium battery has been one of the most importance developments in primary technology over the last 20 years. The earlier work on rechargeable lithium batteries was often driven by the oil crisis in the 1970s and the resulting demand for electric vehicles. The technology of that time was based on a lithium-metal anode, an non-aqueous electrolyte containing a lithium-salt and a solid lithium intercalation electrode acting as the cathode. It is worth pointing out for historical completeness that rechargeable lithium batteries based on a similar technology to the sodium sulphur cell, i.e. using a solid ceramic lithium-ion conductor were also investigated as was a molten-salt battery based on a lithium anode, a mixed alkali chloride eutectic and iron sulphide as the cathode, but these have not proved to be technical feasible as commercial products.

There are several reasons why rechargeable lithium batteries did not reach commercial success in the '70s. The earliest developments at that time focused on technologies such as the titanium disulphide battery which consisted of a lithium-metal anode, a lithium-salt, typically $LiBF_4$ in an organic solvent such as 1,3-dioxylene, and TiS_2. The sulphides were more difficult to prepare than oxides and also suffered from being air sensitive although they did show rapid and highly reversible intercalation. Furthermore, because the top of the valence band edge in the sulphide is typically 1-2 eV higher than in an oxide, this limited how low a Fermi level could be obtained in such systems. Since the open circuit potential of the cell is determined by the difference in the Fermi level between the anode and cathode and since the lithium level is high, a relatively high Fermi level in the cathode results in a cell voltage which would not exceed around 2.5 V. Although better than the aqueous systems, this is still not as high as can be achieved by using oxide-based cathodes. Another key problem with the lithium battery technology of the time was the use of

lithium-metal as an anode. Despite the clear advantage of such an electrode, as mentioned above, it proved very difficult to obtain stripping and plating efficiencies which exceeded 99.5 %. Lithium is so reactive that in all solvents a surface layer rapidly forms, the composition of which depends on the solvent. As a result, on plating lithium the highly active material on the surface rapidly reacts with the solvent, furthermore, rapid plating (i.e. rapid charging) can result in the formation of lithium dendrites and in turn produce internal short circuit leading to safety problems. In most prototype lithium anode rechargeable cells, a 3-6 fold excess of lithium is required to compensate for the losses involved in the plating and stripping efficiency and this represents a significant cost of the whole device. Unquestionably the biggest single factor which contributed to the lack of commercial success for lithium anode rechargeable batteries is the safety problem associated with the lithium electrode. Whether originating from internal short circuits or otherwise, accidents with prototype systems leading to fire or explosion led to the abandonment of the Li/MoS_2 rechargeable battery in 1989 [11]. It was clear to those involved in the technology in the 1980s that despite many efforts the lithium anode had not been improved to a point when it could be used safely and efficiently. For this reason, the future of lithium batteries hung in large measure on finding a replacement for the lithium anode. The breakthrough was the development of carbon as an intercalation electrode to replace lithium. There are many books and review papers available on lithium batteries [6-11].

1-1-2 Lithium ion batteries

In the original rechargeable lithium battery, deposition and stripping of lithium during charge and discharge at the anode was accompanied by lithium intercalation/deintercalation at the cathode material acting like a "sponge" accepting or releasing lithium ions. The replacement of the lithium anode with an intercalation electrode leading to two lithium "sponges" used in a rechargeable cell was proposed

in the early 1980's [12-15]. In this approach lithium ions can be shuttled (or rocked) from one sponge to another as the cell is cycled. Such a system avoids the use of lithium metal, and consequently the safety of the system is enhanced. This battery system is known as lithium-ion, or rocking-chair [11], or a SWING battery [16]. The cathode sponge is composed of a transition metal oxide, similar to those used in the original rechargeable lithium batteries. The anode should have the lowest possible potential close to that of lithium electrode in order to ensure the cell voltage is as high as possible. In the early stages, $LiWO_2$, $Li_6Fe_2O_3$, $Li_9Mo_6Se_6$ etc. were considered [12, 17, 18]. However, the potentials of these were too close to the cathode resulting in low cell voltage. The practical benefits of Li-ion technology were not realised until the Sony corporation in the late 1980s [19-21] found that although many carbons will not accommodate lithium, certain forms will do so and hence can be used as reversible lithium intercalation materials [22-24]. Fig 1-1-1 illustrates the charge and discharge processes in a lithium ion battery based on a $LiMn_2O_4$ cathode and a graphite anode. The latter can accommodate up to one lithium for every six carbons.

$$xLi^+ + xe^- + \underbrace{C_6(graphite)}_{discharged} \leftrightarrow \underbrace{Li_xC_6}_{charged} \qquad (0 \le x \le 1)$$

The first rechargeable lithium ion battery was commercialised by Sony [19-21] and was based on a $LiCoO_2$ cathode and a coke anode which accommodate only one lithium for every twelve carbons i.e. half the gravimetric capacity of graphite. Fig 1-1-2 shows the construction of the commercial Sony cell. In contrast to conventional aqueous batteries, this cell yields an average 3.6 volt on discharge, as indicated in Fig 1-1-3, and this is three times that of a Ni-Cd battery so that three Ni-Cd cells in series are required to provide the same operating voltage. Today, research on carbon or graphite anode materials is very active, involving various aspects such as material preparation, structural characterisation, physical and chemical properties, electrode performance, electrolyte influence and so on [25-29].

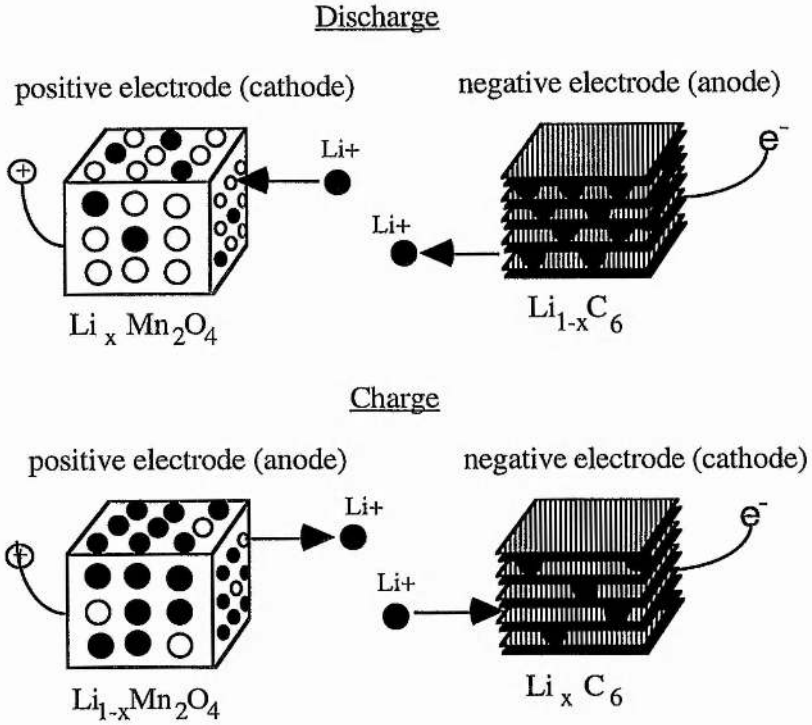

Fig 1-1-1 Schematic representation of a rocking-chair lithium battery ($1 \leq x \leq 0$).

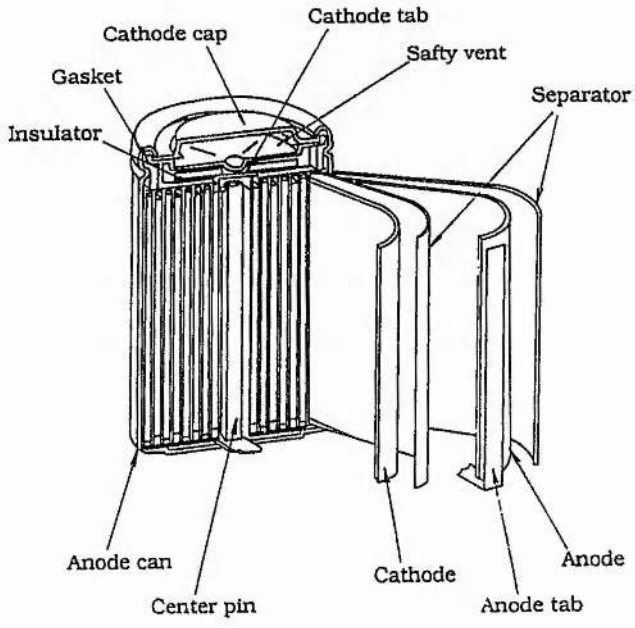

Fig 1-1-2 Sony cell construction (quoted from [21]).

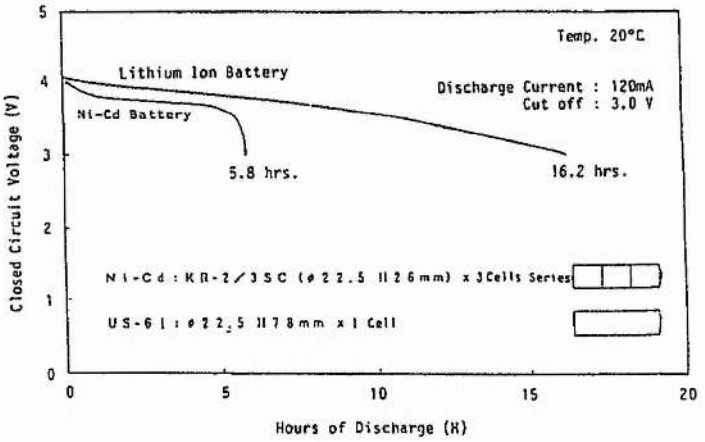

Fig 1-1-3 Comparison of discharge curves of lithium ion battery and Ni-Cd battery with same battery dimension (quoted from [20]).

1-1-3 Cathode materials

The cathode materials used in a rechargeable lithium battery or lithium ion battery are mainly transition metal oxides. A good cathode material is expected to possess a high gravimetric and volumetric capacity, a high potential, fast electrode kinetics, a highly reversible insertion reaction, etc.. [8]. Such cathodes have been studied for almost twenty years [11, 12, 21, 30-33]. The potentials of various cathodes are given in Fig 1-1-4. The relatively low potential of the systems other than oxides is evident. In order to operate in a lithium ion cell a high voltage cathode, to off-set the reduced voltage of anode, is necessary limiting materials to $LiCoO_2$, $LiNiO_2$ and $LiMn_2O_4$ in which lithium intercalation/deintercalation operate around 4 V vs Li/Li^+, see Fig 1-1-4. The first two compounds are layered in structure and the last is a cubic spinel. The reversible lithium content within the layered compounds is around 0.6 Li per formula during intercalation/deintercalation so giving a capacities of 165 $mAhg^{-1}$ slightly higher than that of $LiMn_2O_4$ spinel (148 $mAhg^{-1}$). Fig 1-1-5 shows the variations of operating voltage as a function of lithium content for the three compounds.

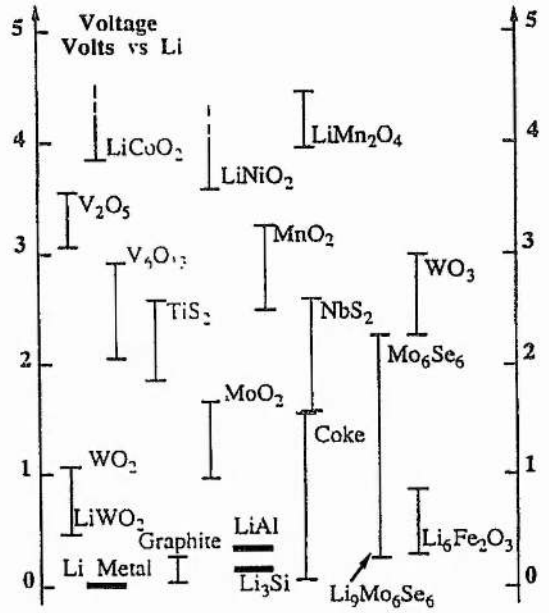

Fig 1-1-4 The range of intercalation potentials for various materials (quoted from [12]).

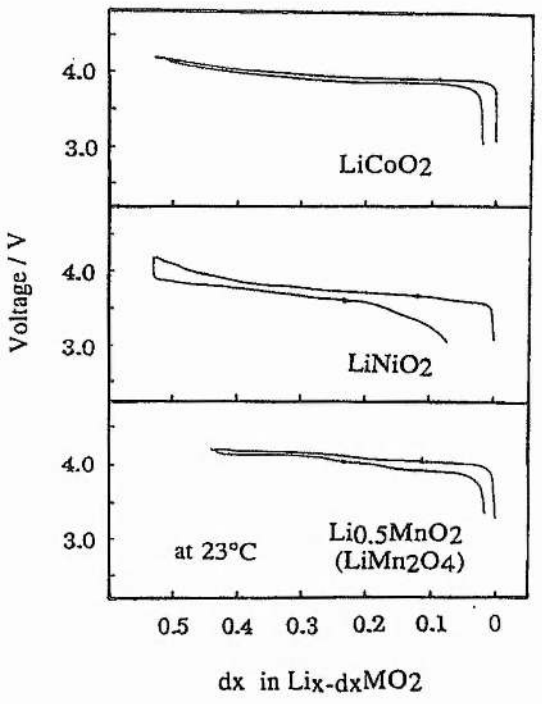

Fig 1-1-5 Charge and discharge curves of $Li/Li_{x-dx}MO_2$(M=Co, Ni and Mn) Charge maximum limit of 4.2 V; discharge: 3.3V cut-off; current density: 0.5 $mAcm^{-2}$ (quoted from [21]).

Table 1-1-2 Overview of the development of rechargeable lithium batteries in the past twenty years (quoted from [11]).

Year	Development of components			Systems
	anode	cathode	electrolyte	
1970's	Li metal Li alloys	transition metal sulphides (TiS_2, MoS_2)	liquid organic electrolytes	$Li/LE/TiS_2$
		transition metal oxides (V_2O_5, V_6O_{13})	solid inorganic electrolytes (Li_3N)	
		liquid cathodes (SO_2)		Li/SO_2
1980's	Li-intercalation ($LiWO_2$)		polymer electrolytes	
		selenides ($NbSe_3$)		$Li/LE/MoS_2$ $Li/LE/NbSe_3$
		discharged cathodes ($LiCoO_2$, $LiNiO_2$)		$Li/LE/LiCoO_2$
	Li-carbon (LiC_{12}) (coke)		plasticised polymer electrolytes	$Li/PE/V_2O_5$ $Li/PE/V_6O_{13}$
		manganese oxide (Li_xMnO_2)		$Li/LE/MnO_2$
				$C/LE/LiCoO_2$
1990's	Li-carbon (LiC_6) (graphite)	manganese oxide ($LiMn_2O_4$)		$C/LE/LiMn_2O_4$

LE stands for liquid organic electrode, PE for polymer electrolytes.

Table 1-1-2 summaries various lithium systems which have been studied intensively in the past twenty years. As can be seen, $LiMn_2O_4$, $LiCoO_2$ and $LiNiO_2$ based cells are at the forefront. In particular, the manganese material has been recognised as an excellent candidate for the new generation of lithium ion batteries in order to reduce the cost of the present lithium ion battery based on $LiCoO_2$ cathodes. This is because manganese oxides are cheaper and less toxic than the other oxides. Furthermore

manganese based oxides has been used for 100 years in primary batteries and their handling and recycling is well known making them particularly suitable for the strict environment protection legislation in the next century.

1-1-4 Polymer electrolytes

Another significant contribution to the development of lithium batteries was the discovery of polymer electrolytes [35-39]. Such materials are ionically conducting solid phases formed by the dissolution of salts in ion-coordinating polymers. They were first studied by Wright and co-workers [37], while recognition of the potential of such systems as practical materials for applied electrochemistry, and much of the early development, was due to Armand *et al.* [38]. Because of the merits of solid electrolytes, such as the absence of liquid leakage and flexibility of manufacturing processes, commercial application of solid polymer electrolytes to rechargeable batteries is very attractive.

Recently, newly-developed gels or plasticised electrolytes have permitted significant improvement in the conductivity of polymer electrolytes at room temperature [35, 36]. This new type of polymer electrolyte is prepared from a liquid gelled by a polymeric additive, or by addition of a liquid phase to a polymer. The liquids used are organic solvents such as propylene carbonate (PC) and ethylene carbonate (EC). These solvents themselves are the basis of a good conducting medium, while the polymers most likely play the part of a matrix to trap the organic liquids. For example, the poly(acrylonitrile) (PAN) based gel electrolyte has a conductivity of 1.7-1.2x10^{-3} Scm^{-1} at 20 °C [40]; the KYNAR based gel electrolyte, containing a copolymer blend of polyvinylidene fluoride/hexafluoropropylene, reaches 3x10^{-3} Scm^{-1} for the composition of $LiPF_6$ (1M)/EC:PC(1:1)/20 wt % KYNAR at room temperature [41]. These values are close to the typical conductivity of organic liquid electrolytes (10^{-3}-10^{-2} Scm^{-1}) [42].

1-2 Lithium manganese oxide spinel: literature review

There are many 3 V cathodes based on various manganese oxides [43-57]. Only lithium manganese oxide spinel $LiMn_2O_4$ can be used as both 3 V and 4 V cathodes in lithium batteries [50, 57]. The spinel oxide as cathode material was discovered in 1981 and in the 1980s the research on this spinel focused mainly on the aspects of structure and intercalation characteristics [58-64]. In this thesis work is presented on the electrochemical performance of this spinel. The following is a brief review of literature work on the compound.

1-2-1 Structural characteristics

Spinel compounds have the general formula $A[B_2]X_4$, and cubic spinel possesses prototypic symmetry Fd3m (O_h^7) (Fig 1-2-1), in which the X anions form a cubic-close-packed array occupying the 32e sites of the space group; the B cations occupy half the octahedral sites, the 16d sites, and the A cations take one-eighth of the tetrahedral sites, 8a. The interstitial octahedral sites 16 c are interconnected in 3D by sharing common edges with six like near neighbours exactly as the 16d sites, but shifted by half a lattice parameter in space. Each 16c site shares two common faces, on opposite sides, with occupied 8a sites; the other faces are shared with empty, interstitial tetrahedral sites, 48f. The final empty tetrahedral sites, 8b, share faces with four, occupied 16d octahedral sites; it would require a large energy to insert cations into the 8b sites. The lattice parameter of cubic spinel $LiMn_2O_4$ is 8.24 Å. Lithium may be removed from $LiMn_2O_4$ while retaining the Mn_2O_4 framework to yield λ-MnO_2 with a lattice constant of 8.03 Å [50]. However, it was found that the lattice parameter of $LiMn_2O_4$ varies with its preparation temperature [65].

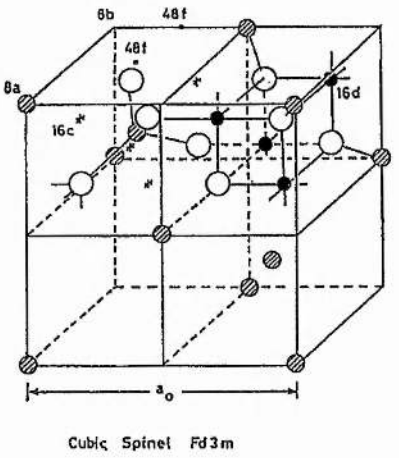

Fig 1-2-1 Two quadrants of cubic $A[B_2]X_4$ spinel, space groups Fd3m (O_h^7).

1-2-2 Lithium intercalation

Li at 8a sites can be removed from $LiMn_2O_4$ by chemical [50, 60] and electrochemical techniques [57, 60, 66], while lithium can also be inserted into $LiMn_2O_4$ occupying 16c sites. During these insertion and extraction processes the Mn_2O_4 spinel framework is unperturbed and the processes are reversible. Fig 1-2-2 shows the variation of potential of $Li_xMn_2O_4$ as a function of composition exhibiting two well separated potential plateaux in the composition range of $0 \leq x < 2$ [58, 66, 67]. Because of this characteristic, $LiMn_2O_4$ is an unique material which can be used as both 3 volt and 4 volt cathodes, the higher plateau in voltage (4 V vs. Li/Li^+) being attractive to lithium ion technology. The reason that a nearly 1 V voltage gap occurs at the critical composition $Li_{1.0}Mn_2O_4$ (Fig 1-2-2) has not been fully understood yet.

Operating at the higher potential plateau, i.e. from $LiMn_2O_4$ to λ-MnO_2, the spinel remains cubic [66]. However, the spinel will undergo a cubic/tetragonal phase transformation when operating at the lower potential plateau. This is due to a Jahn-Teller distortion. $LiMn_2O_4$ has a mixed B-site valence, $Li[Mn^{3+}Mn^{4+}]O_4$. According to crystal field theory, the fivefold-degenerate d-orbital manifold splits into three t_2 orbitals and two e orbitals in the octahedral field, so that in the high-spin state, the d^4 configuration of Mn^{3+}-ion becomes $t_2^3e^1$; and the d^3 one of Mn^{4+}-ion $t_2^3e^0$. Since

Mn^{3+} ($t_2^3e^1$) has a single electron in the e-orbital, a cooperative Jahn-Teller distortions may occurs as the result of e-orbital degeneracy [68]. When lithiation proceeds, the concentration of Mn^{3+} ions in octahedral increases and therefore the spinel $Li_{1+x}Mn_2O_4$ changes from cubic (c/a = 1.0) at x = 0 to tetragonal symmetry (c/a = 1.161) at x = 1 [58, 61, 62]. The lithiation is associated with a two-phase reaction characterised by a flat discharge curve (see Fig 1-2-2). Furthermore the phase transition increases the volume of unit cell by 6.5 % [53, 56].

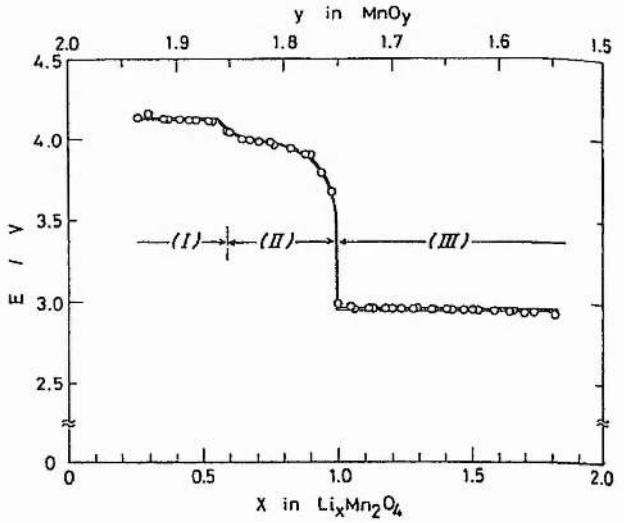

Fig 1-2-2 Open-circuit voltage curve of spinel-related $Li_xMn_2O_4$ at 30 °C (quoted from [66]).

1-3 Purpose of this research

The development of manganese oxide spinel for lithium battery cathode is of considerable importance. Although spinel manganese oxide possesses a high voltage, low cost and low toxicity, the early material displayed poor cyclability and low practical capacity. The more recent low temperature preparations improved this situation. However, the relationship between synthesis, composition, structure and performance in the 4 V and 3 V regions was not well understood. Also material exhibiting acceptable performance for commercial application had not been prepared.

Preparation conditions of solids can modify material performance as a result of the influences on particle size, morphology and crystalinity. Therefore, the preparation conditions for lithium manganese oxide spinels were investigated further and a new synthesis based on a solution route proposed. Electrochemical studies of the new lithium manganese oxide spinels have been carried out with particular attention given to the optimisation of capacity and its retention on cycling at 3 and 4 V. Both voltages remain of interest because despite the development of lithium ion technology there is still much interest in lithium anode cells because of their very high gravimetric energy density. For spinel cathodes operating at 4 V, the study of the electrochemical stability of electrolytes at these high potentials is included in this thesis. Finally the factors controlling cycle life of spinel cathodes have been investigated.

References

[1] Comprehensive Treatise of Electrochemistry, Volume 3: Electrochemical Energy Conversion and Storage, edited by Bockris, Conway, Yeager, and White, Plenum Press, 1981.

[2] C.A.Vincent, F.Bonino, M.Lazzari, and B.Scrosati, Modern Batteries an introduction to electrochemical power sources, Edward Arnold (Publishers) Ltd., 1984.

[3] D.F.Gosden, J. Power Sources, **45** 61 (1993).

[4] C.K.Mann, Nonaqueous solutions for electrochemical use, in Electroanalytical Chem., 58 Volum 3, edited by A.J.Bard, Marcel Dekker Inc., 1969.

[5] J.B.Goodenough, Solid State Ionics, **69** 184 (1994).

[6] Recent Advances in Rechargeable Li Batteries, edited by J.M.Tarascon, Solid State Ionics, **69** (Special Issue) (1994).

[7] Industrial Chemical Library, Volume 5, Lithium Batteries New materials, Development, and Perspectives, edited by G.Pistoia, ELSEVIER, (1994)

[8] Lithium Batteries, edited by J.P.Gabano, Acdemic Press. (1983).

[9] Proceedings on Symposium on Lithium batteries, Proceeding Vol. 84-1, edited by A.N.Dey, (1984).

[10] Practical Lithium Batteries, edited by Y.Matsuda, and C.R.Schlaikjer, JEC Press, (1988).

[11] K.Brandt, Solid State Ionics, **69** 173 (1994).

[12] D.Guyomard, and J.M.Tarascon, Solid state Ionics, **69** 222 (1994).

[13] D.W.Murphy, F.J.DiSalvo, J.N.Carides, and J.V.Waszczak, Mat. Res. Bull., **13** 1395 (1978).

[14] M.Lazzari, and B.Scrosati, Mat. Res. Bull., **13** 773 (1980).

[15] K.Mizushima, P.C.Johes, P.J.Wiseman, and J.B.Goodenough, Mat.Res. Bull., **15** 783 (1980).

[16] R.Bittihn, R.Herr, and D.Hoge, J. Power Sources, **43/44** 223 (1993).

[17] B.Scrosati, Proc. Electrochem. Soc., **P2-15** 70 (1992)

[18] D.Fauteux, and R.Koksbang, J. Appl. Electrochem., **23** 1 (1993).

[19] T. Nagaura, 3th International Rechargeable Battery Seminar, Deerfield Beach, FL, USA (1990).

[20] T.Nagaura and K.Tozawa, Progress in Batteries & Solar, **9** 209 (1990).

[21] K.Ozawa, Solid State Ionics, **69** 212 (1994).

[22] R.Fong, U. von Sacken, and J.R.Dahn., J. Electrochem. Soc., **137** 2009 (1990).

[23] R.Yazami, and PH.Touzain, J. Power Sources, **9** 365 (1983).

[24] M.Mohri, N.Yahagisawa, Y.Tajima, H.Tanaka, T.Mitaie, S.Nakajima, Y.Yoshimoto, T.Suzuki, and H.wada, J. Power Sources, **26** 545 (1989).

[25] J.R.Dahn, A.K.Sleigh, Hang Shi, J.N.Geimers, Q.Zhong, and B.M.Way, Electrochimica Acta, **38** 1179 (1993).

[26] K.Sawai, Y.Iwakoshi, T.Ohzuku, Solid State Ionics, **69** 273 (1994).

[27] U.von Sacken, E.Nodwell, A.Sundher, and J.R.Dahn., Solid state Ionics, **69** 284 (1994).

[28] D.Aurbach, Y.Ein-Eli, O.Chusid, Y.Carmeli, M.Babai, and H.Yamin, J. Electrochem. Soc., **141** 603 (1994).

[29] K.Tatsumi, N.Iwashita, H.Sakaebe, H.Shioyama, S.Higuchi, A.Mabuchi, and H.Fujimoto, J. Electrochem., Soc., **142** 716 (1995).

[30] T.Ohzuku, and A.Ueda, Solid State Ionis, **69** 201 (1994).

[31] J.Desilvestro, and O.Haas, J. Electrochem. Soc., **137** 5C (1990).

[32] W.Ebner, D.Fouchard, and L.Xie, Solid State Ionis, **69** 238 (1994).

[33]C.Delmas, H.Cognac-Auradou, J.M.Cocciantelli, M.Ménétrier, and J.P.Doumerc, Solid State Ionis, **69** 257 (1994).

[34] T.Nohma, T.Saito, and N.Furulkawa, J. Power Sources, **26** 389 (1989).

[35] M.Armand, Solid State Ionics, **69** 309 (1994).

[36] R.Koksbang, I.I.Olsen, and D.Shackle, Solid State Ionics, **69** 320 (1994).

[37] D.E.Fenton, J.M.Parker, and P.V.Wright, Polymer, **14** 589 (1973).

[38] M.B.Armand, J.M.Chabagno, and M.Duclot, Second Int. Conf. on Solid Electrolytes, St. Andrews, 1978, p.65.

[39] P.G.Bruce, and C.A.Vincent, J. Chem. Soc. Faraday Trans, **89** 3187 (1993).

[40] K.M.Abraham, and M.Alamgric, J. Electrochem., **136**, 1657 (1990).

[41] A.M.Christie, personal communication, St. Andrews. (1995).

[42] J.T.Dudley, D.P.Wilkinson, G.Thomas, R.LeVae, S.Woo, H.Blom, C.Horvath, M.W.Juzkow, B.Denis, P.Juric, P.Aghakian, and J.R.Dahn, J. Power Sources, **35** 59 (1991).

[43] T.Ohzuku, M.Kitagawa, and T.Hirai, J. Electrochem. Soc., **137** 40 (1990).

[44] T.Ohzuku, M.Kitagawa, and T.Hirai, J. Electrochem. Soc., **136** 3169 (1989).

[45] T.Nohma, Y.Yamamoto, I.Nakane, and N.Furukawa, J. Power Sources, **39** 51 (1992).

[46] T.Nohma, and N.Furukawa, Proc-Electrochem. Soc., **p1-3** 311 (1991).

[47] T.Ohzuku, Keijiro Sawai, and T.Hirai, Proc.-Electrochem., Soc., **p1-3** 318 (1991).

[48] T.Ohzuku, K.Sawai, and T.Hirai, Chem. Express, **4** 777 (1989).

[49] T.Ohzuku, M.Kitagawa, K.Sawai, and T.Hirai, Chem. Express, **4** 773 (1989).

[50] J.C.Hunter, J. Solid State Chem., **39** 142 (1980).

[51] M.M.Thackeray, M.H.Rossouw, A.de Kock, A.P.de la Harpe, R.J.Gummow, K.Pearce, and D.C.Liles., J. Power Sources, **43-44** 289 (1993).

[52] R.J.Gummow, A.de Kock, and M.M.Thackeray, Solid State Ionics, **69** 59 (1994).

[53] M.M.Thackeray, A de Kock, M.H.Rossouw, and D.Liles, J. Electrochem., Soc., **139** 363 (1992).

[54] A de Kock, M.H.Rossouw, L A de Picciotto, M.M.Thackeray, W I F David, and R.M.Ibberson, Mat. Res. Bull., **25** 657 (1990).

[55] M.M.Thackeray, A de Kock, M.H.Rossouw, D.Liles, R.Bittihn, and D.Hoge, Proc-Electrochem., **p1-3** 326 (1991).

[56] M.H.Rossouw, A de Kock, L A de Picciotto, M.M.Thackeray, W I F David, and R.M.Ibberson, Mat. Res. Bull., **25** 173 (1990).

[57] J.C. Hunter, and F.B.Tudron, Proc.-Electrochem. Soc., **p1-3** 445 (1991).

[58] M.M.Thackeray, W.I.F.David, P.G.Bruce, and J.B.Goodenough, Mat. Res. Bull. **18** 461 (1983).

[59] W.I.F.David, J.B.Goodenough, M.M.Thacheray, and M.G.S.R.Thomas, Revue de Chimie minérale, **20** 636 (1983).

[60] M.M.Thackeray, P.J.Johnson, L A de Picciotto, P.G.Bruce, and J.B.Goodenough, Mat. Res. Bull., **19** 179 (1984).

[61] J.B.Goodenough, M.M.Thackeray, W.I.F.David, and P.G.Bruce, Revue de Chimie minérale, **21** 435 (1984).

[62] J.B.Goodenough, Proc. -Electrochem. Soc., **85-4** 77 (1985).

[63] W.I.F.David, M.M.Thackeray, L.A.De Picciotto, and J.B.Goodenough, J. Solid State Chem., 67 316 (1987).

[64] M.M.Thackeray, L.A.DE Picciotto, A.DE Foch, P.J.Johnson, V.A.Nicholas, and K.T.Adendorff, J. Power Sources, **21** 1 (1987).

[65] G.Pistoia, and G.Wang, Solid State Ionics, **66** 135 (1993).

[66] T.Ohzuku, M.Kitagawa, and T.Hirai, J. Electrochem. Soc., **137** 769 (1990).

[67]S.Bach, J.P.Pereira-Ramos, N.Baffier, and R.Messina, Electrochimica Acta, **37** 1301 (1992).

[68] A.R.West, Solid State Chemistry, John Wiley & Sons, 1987.

CHAPTER TWO

Principles of Intercalation Compounds and Experimental Techniques

This chapter describes the fundamental principles and properties of the intercalation compounds. The measurement of these properties is an important aspect of characterising such materials and these techniques are described briefly here. More details of the fundamentals may has found in a new book of Solid State Electrochemistry [1].

2-1 Intercalation compounds

Intercalation compounds as a new class of electrode materials used in rechargeable lithium batteries was definitely proposed in 1979 [2]. Intercalation compounds are defined as being solids made of host atoms and guest atoms (or molecules). The host atoms provide a lattice or framework, the guest atoms occupy sites within this framework. Two properties distinguish intercalation compounds from other solids: the guests are mobile, moving between sites in the host lattice; and the guests can be added to the host or removed from it, so the concentration of guests can change. These two properties are the basis of the electrochemical application of intercalation compounds in battery technology. Associated with this are structural change that can accompany change in guest concentration. The thermodynamics and kinetics of the guest within the host are also a function of the concentration of the guest. All these change can have an important influence on the properties and hence application of intercalation compounds as electrodes in batteries. There are many references available [1-13].

2-1-1 Structure Characteristics

2-1-1-1 Host framework

Considerable number of transition metal oxides and chalcogenides are intercalation compounds. These transition metal compounds can exist as three, two or one dimensional hosts. According to the dimensionalities of framework structure and the connection between the sites for guests, there are four possible geometries , as shown in Fig 2-1-1.

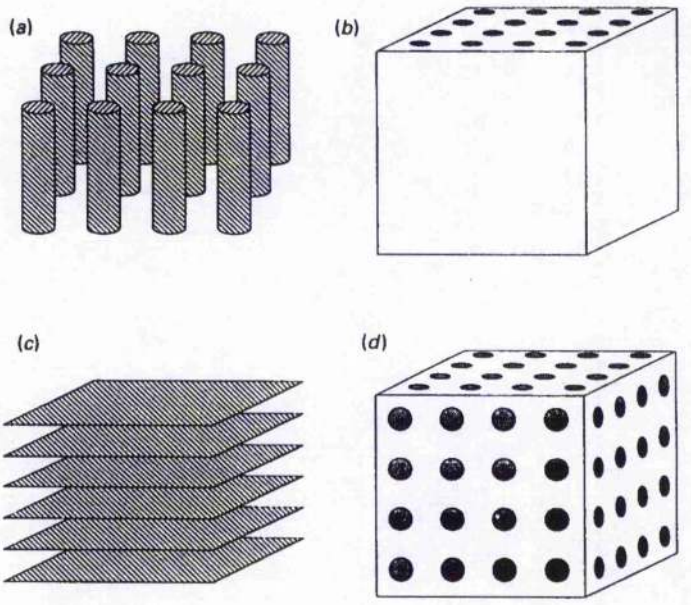

Fig 2-1-1 Schematic representation of host structures with different dimensionality: (a) one-dimensional host, three-dimensional network of sites; (b) three-dimensional structure, with one-dimensional tunnels, for example $LiMoO_2$; (c) two-dimensional systems: layered host, layers of sites for guests, TiS_2, $LiCoO_2$ and $LiNiO_2$ all belong to this type of geometric structures; (d) three-dimensional systems, such as $LiMn_2O_4$ spinel. (quoted from [1]).

2-1-1-2 Guest sites

Often the host framework is built from close packed anion planes forming cation sites that are (i) octahedral, (ii) tetrahedral or (iii) trigonal prismatic, illustrated in Fig 2-1-2.

Li^+ prefers to be located in the first two types, i.e. octahedral or tetrahedral (Fig 2-1-2 (a)), while large ions like Na^+ may occupy trigonal prismatic sites, e.g. Na_xTiS_2. Trigonal prismatic sites occur when one close-packed layer sits directly over another (Fig 2-1-2 (b)).

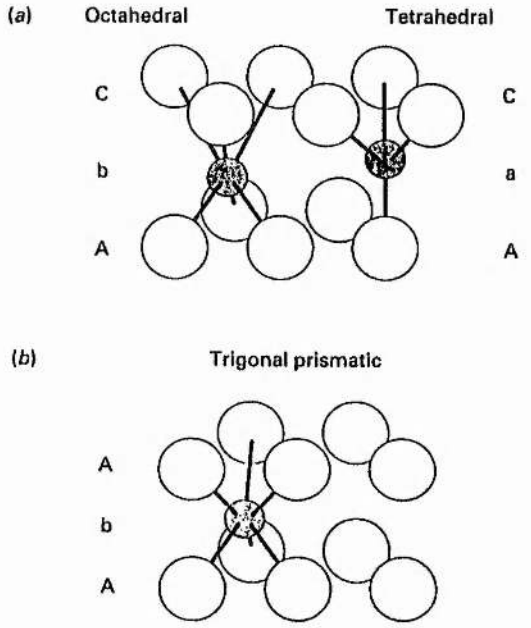

Fig 2-1-2 Sites for intercalated ions between close-packed layers of anions: (a) octahedral and tetrahedral sites; (b) trigonal prismatic sites (quoted from [1]).

2-1-1-3 Energy bands

In transition metal compounds, electron p orbitals from the anion overlap with s, p, and d orbitals from the transition metal, forming bonding and antibonding levels. The periodicity of the solid spreads these levels into bands. Although each band contains contributions from both types of atoms, it is convenient to label a band by the atom and orbital that contribute the most weight to it, and to neglect the mixed nature of the bands where possible. Fig 2-1-3 schematically shows the relevant energy bands. The anion p bands are filled, and the transition metal d bands are empty or partially occupied. The d bands split into sub-bands depending on how the anion coordinate the transition metal

(based on crystal field theory [14]), for example, the splitting in Fig 2-1-3 (a) resulting from an octahedral coordination, whereas that in Fig 2-1-3 (b) arises from a trigonal prismatic coordination. The outer s orbitals of the guest produce bands (not shown) above the transition metal states. The electrons from the guest are added to the d bands as intercalation proceeds, so the Fermi energy (the energy separating full and empty states) moves upward relative to the bottom of the d bands.

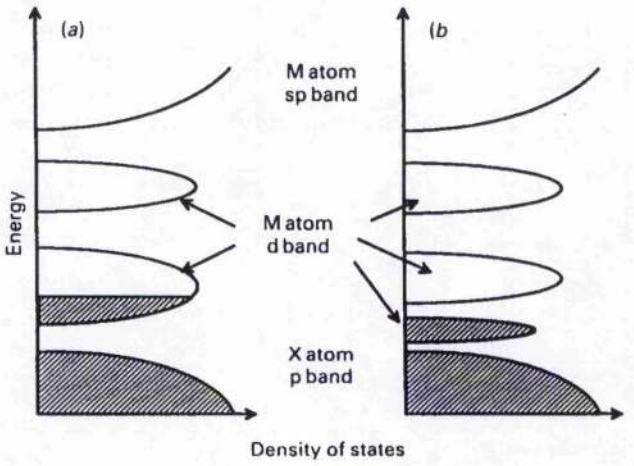

Fig 2-1-3 Electron bands for transition metal compounds. M = metal, X = anion. The filling of the bands is appropriate for MoS_2 (quoted from [1]).

2-1-2 Electrochemical intercalation

The situation that electrons directly transfer from guests to host only happens in the case of chemical intercalation. For electrochemical intercalation, electrons will transfer to the host through an external circuit, while guest ions insert into the host from the electrolyte. This process is schematically shown in Fig 2-1-4 where an electrochemical cell consists of Li and TiS_2 electrodes. A fundamental thermodynamic equation in electrochemistry

$$E = -\frac{\Delta G}{zF} \qquad \{2\text{-}1\text{-}1\}$$

describes the relation between the cell voltage and the energy change of the electrochemical reaction. In this equation F is Faraday's constant, z is the charge of the metal ions in the electrolyte, and ΔG is the change of Gibbs free energy of the electrochemical reaction, e.g. $Li + TiS_2 \xrightarrow{intercalation} LiTiS_2$. The cell voltage E at equilibrium is generally known as the open circuit voltage (OCV). Therefore, electrochemical intercalation provides not only an applicable technology for high energy density batteries, but also a tool to study the process of intercalation itself because ΔG is the difference in Gibbs free energy between lithium in lithium metal and lithium in the intercalation compound.

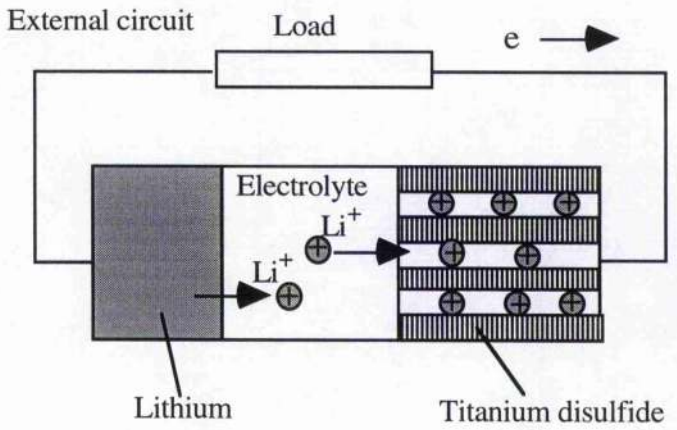

Fig 2-1-4 Schematic representation of an electrochemical cell for lithium intercalation in the layered host titanium disulfide.

2-1-3 Intercalation thermodynamics and kinetics

2-1-3-1 Thermodynamics

The difference in potential is also the difference in chemical potential μ ($\mu = \partial G / \partial n$) for lithium in the metal and in the intercalation host

$$-zeE = \mu - \mu_o. \qquad \{2\text{-}1\text{-}2\}$$

where the chemical potential of Li in the host and in Li metal are denoted by μ and μ_o, respectively. μ_o is a constant because the concentration of lithium in the metal is invariant. However, this is not the case for μ. The chemical potential of lithium in the intercalation compound can vary with the lithium concentration. E is therefore proportional to μ. Thermodynamics requires that μ increases with the concentration of guest ions, and so E decreases as ions are inserted into the host electrode.

Furthermore, the chemical potential μ can be related to the concentration of intercalated ions according to a lattice-gas model

$$\mu = \varepsilon + kT\log[x/(1-x)] + Ux \qquad \{2\text{-}1\text{-}3\}$$

where the term ε is the energy to put an isolated ion and its electrons into the lattice, the so-called site energy, the second term relates to the configurational entropy of ions in the host, by assuming a random distribution of ions over a fraction x of the available sites N_s, and the Ux term is a measure of the interaction between the ions, based on the mean field theory [1, 3, 4]. This equation is a fundamental equation of intercalation thermodynamics for a solid solution. Since E(x) can be measured accurately enough for the derivative $-\partial x/\partial E$ to be calculated, it is possible to measure thermodynamic quantities such as entropy S, enthalpy H, etc. from data of E vs. x [5, 15, 16].The equation {2-1-3} also provides a way to study the interaction between guest ions, i.e. the Ux term, from experimental data of E (x) [17].

The equation {2-1-3} implies that electrode potential, E, of an intercalation compound varies as a function of x in an s-shape. However, such a relation does not exist when there are two phases associated with intercalation. In this situation intercalation merely results in the conversion of one phase of fixed composition into another also of fixed composition. This results in a fixed change of chemical potential and hence an invariant E. In this case, the E(x) curve appears L-shaped.

2-1-3-2 Kinetics

Transport of ions within a host always govern the intercalation rate. According to the theory of a mixed ionic and electronic conductor, the transport process is characterised by two parameters, $\tilde{D}_i$ and D_i [1]. D_i is the *diffusivity* of the mobile species i (sometimes also called *component diffusion coefficient*) and is directly related to the ion mobility. When there is a concentration gradient in Li^+, however, the ions and electrons must move at the same rate because of the requirement of electroneutrality. This combined motion is associated with $\tilde{D}_i$, *chemical diffusion coefficient.* It may be defined as the proportionality constant between the flux of the combined motion and the concentration gradient of species *i*. D_i and $\tilde{D}_i$, are related to each other by

$$\tilde{D}_i = D_i W_i \qquad \{2\text{-}1\text{-}4\}$$

where W_i is called Wagner factor (or thermodynamic factor) to show the influence of one species on the mobility of the other species. If the host is predominantly an electronic conductor, then

$$W = \frac{\partial \ln a_i}{\partial \ln c_i}. \qquad \{2\text{-}1\text{-}5\}$$

Where a and c are the activity and concentration of the species i, respectively. Experimentally, the *chemical diffusion coefficient* $\tilde{D}$ may be determined by GITT [13] or the ac impedance technique [18], and W is obtained from the slope of the coulometric titration curve, i.e. EMF vs. x, and then the *diffusivity* D can be calculated from Eqn {2-1-4} [15, 18. 19].

2-2 Syntheses of intercalation compounds

Most intercalation materials are prepared directly by solid-state reaction or sol-gel process, but some of them are not, for instance, cubic TiS_2 can only be prepared in two

steps by: first synthesising $CuTiS_2$ using a solid state reaction and then removing Cu by deintercalation [20].

2-2-1 Solid-state reaction and sol-gel reaction

2-2-1-1 Solid-state reactions

Solids do not usually react together at room temperature over normal time scales and it is necessary to heat them to much higher temperatures in order for reaction to occur at an appreciable rate. Thus a solid-state reaction is often characterised by a high-temperature. Fig 2-2-1 illustrates how a solid-state reaction proceeds. The reaction starts at the interface between MgO and Al_2O_3 particles (Fig 2-2-1(a)), and then the produced phase, $MgAl_2O_4$ in this case, grows at each interface associating with the Al^{3+} and Mg^{2+} diffusion in the opposite direction to each other (Fig 2-1-1(b)) [2]. It can be seen from this process that the rate of a solid state reaction relies on the particles size of the reactants and contact area between the grains. Heating promotes ion diffusion. It is also always good practised to regrind a solid mixture during the reaction so as to maximise the surface areas of contact between the reactants. Sometimes solid reactants are pelletised to increase further the contact between grains.

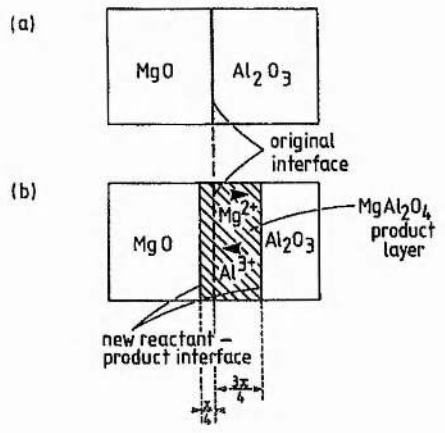

Fig 2-2-1 Schematic reaction, by interdiffusion of cations, of single crystals of MgO and Al_2O_3 to give $MgAl_2O_4$ (quoted from [21]).

2-2-1-2. Sol-gel reactions

The sol-gel method offers an approach to the synthesis of oxide materials via wet chemical reactions [22-26]. The theory and practice of sol-gel reactions are summarised in the reference 23. In general, preparation of a powdered oxide using the sol-gel technique is divided into two steps, (1) a solution reaction involving hydroxylation and condensation of molecular precursors, and (2) sintering of the gel at a suitable temperature [22]. Compared with the conventional "powder" route (solid state reaction), the sol-gel approach undoubtedly offers a high level of chemical homogeneity in multi-component materials and so sintering temperatures are usually lower. It has been widely acknowledged that the sol-gel technique is a low temperature route to the preparation of high performance intercalation materials [27]. The preparation of amorphous LiV_3O_8 via a sol-gel reaction is a typical example [28].

2-2-2 Chemical and electrochemical lithiation

2-2-2-1 Chemical lithiation

Chemical lithiation operates mostly in solution, and is classified as soft chemistry or chimie douce [22]. These terms refer to the synthesis of solids by mild, low temperature routes where control of the resulting structure is possible. In general, a soluble lithiation agent reacts with a solid host (MX_n) which does not dissolve in the solution, and meanwhile this agent also acts as a source of lithium ions. For example, lithiation by n-buthyl lithium (n-BuLi) in hexane, heptane, or acetonitrile solution [9],

$$x\text{n-BuLi} + MX_n \rightarrow Li_x\, MX_n + x/2C_8H_{18}.$$

The ability of a reagent to intercalate lithium depends on its reduction potential. From thermodynamics, a reagent can reduce (i.e. lithiate) a host (MX_n) if its redox potential

is lower than that of the host. Fig 2-2-2 presents redox potentials of various reagents. It is obvious that n-BuLi is a very strong reducing agent, and so is often used to prepare fully lithiated compounds. According to the Nernst equation

$$E_{Ox/\mathrm{Red}} = E^{o}_{Ox/\mathrm{Red}} + (RT/zF)\ln\frac{[Ox]}{[\mathrm{Red}]},$$

it is possible to adjust the reducing power of a reagent by controlling the reaction temperature and concentration when the reagent is a reversible couple. For example, Tarascon and Guyomard used LiI to lithiate $LiMn_2O_4$ to $Li_{1+x}Mn_2O_4$ ($0< x \leq 1$) at an elevated temperature (83 °C) and by controlling the amount of LiI [29].

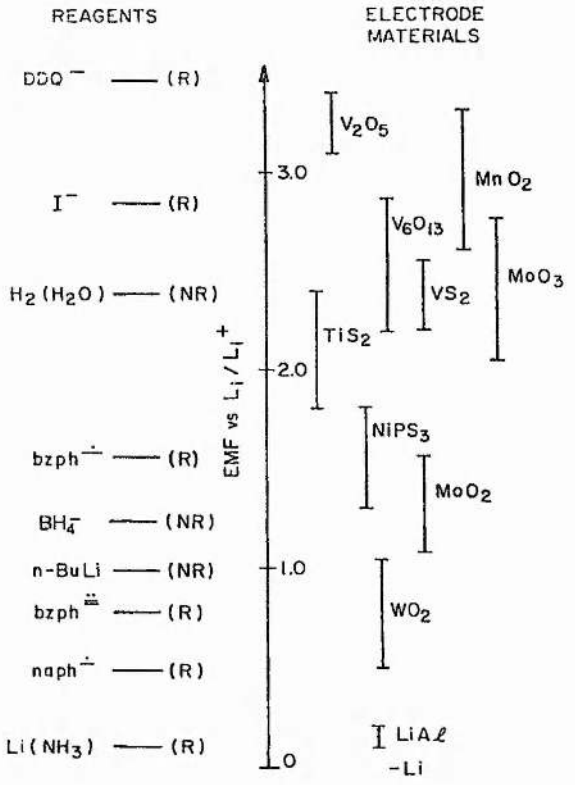

Fig 2-2-2 A comparison of the redox potentials of a variety of intercalation reagents and hosts. the scale is an estimate based on observations from Li intercalation. (R) denotes reagents for which the redox couple is reversible and (NR) denotes irreversibility (quoted from [9]).

For deintercalation the reagents must be oxidising, such as I_2 and Br_2 [3, 9]. Fig 2-2-2 shows that water itself can act as a reagent; a famous example is Hunter's method for

the preparation of spinel-related manganese oxide (λ-MnO_2) by leaching lithium from $LiMn_2O_4$ in acidic aqueous solution [30]. A more powerful oxidising agent is nitryl hexafluorouphosphate (NO_2PF_6) (2.1 V vs. NHE) [31] It has been reported that it can extract lithium from $LiNiO_2$ and $LiCoO_2$ [31, 32].

2-2-2-2 Electrochemical lithiation

Electrochemical lithiation has been described in section **2-1-2**, where lithium ions are inserted into TiS_2. The lithium content x in Li_xTiS_2 can be controlled by controlling the charge passed and by controlling the current the rate of intercalation may be fixed. The electrochemical method therefore offers advantages over chemical methods [9, 27]. However, electrochemical reactions are not ideal for preparing large quantities of samples for *ex situ* studies [9].

2-3 Powder X-ray diffraction technique

There are three main categories of physical techniques with which the structure of solids may be characterised: diffraction, microscopic and spectroscopic techniques [21]. Powder X-ray diffraction is one of the best methods for establishing the crystal structure or any change in it, particularly in the case of intercalation compounds where single crystals are often not available [21].

2-3-1 Production of X-rays and their characteristics

X-rays are a form of electromagnetic radiation with a wavelength of ~ 1 Å (10^{-10} m). X-rays are produced when high energy particles, e.g. electrons accelerated through 30000 V, collide with matter. There are two processes which give rise to *white* and *monochromatic* radiation, respectively. The white radiation results from electrons being slowed down or stopped by collision with some of their energy being converted into

electromagnetic radiation. Monochromatic X-rays are caused by electronic transitions within the atoms, as illustrated by Fig 2-3-1, where the accelerated electrons strike a metal target, often copper, to ionise some of the copper 1s (K shell) electrons, an electron in an outer orbital (2p or 3p) immediately drops down to occupy the vacant 1s level and the energy released in the transition appears as X-radiation.

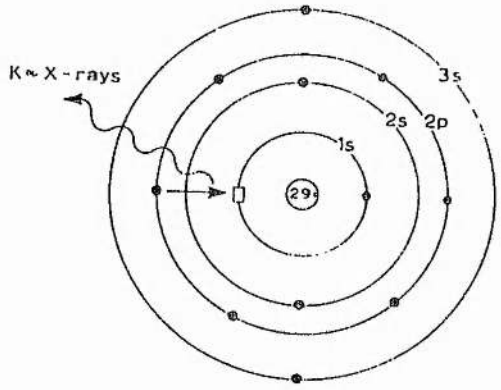

Fig 2-3-1 Generation of Cu K_α x-rays. A 2p electron falls into the empty 1s level (□) and the excess energy is released as X-rays.

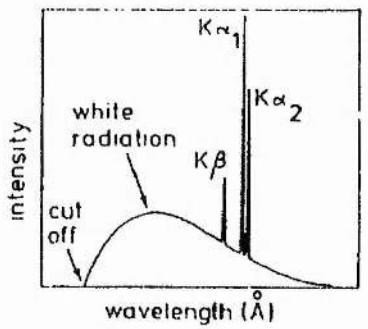

Fig 2-3-2 X-ray emission spectrum of a metal, e.g. copper.

For copper, the 2p → 1s transition is called K_α and has a wavelength of 1.5418 Å whereas the 3p → 1s transition, K_β, has a wavelength of 1.3922 Å. In fact, the K_α transition is a doublet due to two possible spin states. Fig 2-3-2 represents the features of a X-ray emission spectrum of an element such as copper, the intense monochromatic peaks superposed on a background of "white" radiation. In many X-ray diffraction

experiments, the most intense line, K_α, is selected by filtering out all other wavelengths.

2-3-2. Bragg's Law and diffraction patterns

By analogy with the diffraction of light by an optical grating, crystals, with their regularly repeating structures, are capable of diffracting X-rays. Diffracted beams from atoms in successive planes can cancel each other unless they are in phase, and to be in phase they must obey Bragg's Law (illustrated in Fig 2-3-3)

$$2d\sin\theta = \lambda n \qquad n = 1, 2, 3, \qquad \{2\text{-}3\text{-}1\}$$

where λ is the wavelength of the X-rays, d is the distance between planes, and θ is the angle of incidence of the X-ray beam to the plane. Bragg's law is fundamental to the use of the X-ray diffraction technique.

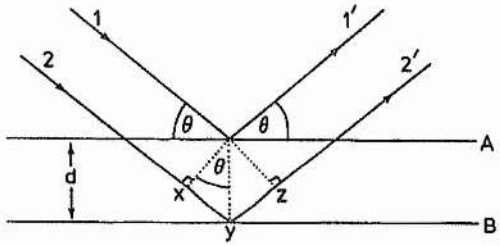

Fig 2-3-3 Derivation of Bragg's Law for X-ray diffraction.

In practice, the angle θ is continuously changed by the diffractometer and so a series of diffraction lines or peaks which follow the relationship of equation {2-3-1} are produced from a solid powder. The positions of diffraction lines are essentially fixed for a given substance and are characteristic of the substance. The intensity of each diffracted lines is related to the arrangements of atoms in the crystal structure and this is important in determining structures.

2-3-3 Crystal structure identification and determination

For identification purposes, principal note is taken of line positions together with a semiquantitative consideration of intensities. The general procedure is to compare the X-ray diffraction pattern of a sample with a standard pattern given in the Powder Diffraction File.

The lattice parameters of a unit cell can be calculated from the positions of diffraction peaks when the pattern has been indexed. The unit cell is defined as *the smallest repeating unit that shows the full symmetry of the crystal structure*. A unit cell is characterised by three edges, a, b, c, and three angles ,α, β, γ; for example, a cubic cell: $a = b = c$, $\alpha = \beta = \gamma = 90^{o}$. Since the θ values can be measured directly, then the d value for each diffraction line can be calculated by Bragg's Law. Consequently, the lattice parameters may be obtained from d-spacing formulae once Miller indices hkl are assigned for each diffraction line. Miller indices are a set of three numbers, hkl, which identify each lattice plane (i.e. diffraction plane according to Bragg's Law). For orthogonal crystals (i.e. $\alpha = \beta = \gamma = 90^{o}$), the d-spacing formula is

$$\frac{1}{d_{hkl}^2} = \frac{h^2}{a^2} + \frac{k^2}{b^2} + \frac{l^2}{c^2}. \qquad \{2\text{-}3\text{-}2\}.$$

Determining an unknown crystal structure from the measured X-ray diffraction data is complicated, quantitative measurements of intensity being necessary. Nowadays this analysis is frequently carried out by a refinement technique. For instance, if a model for the structure is known or partially known, it may be refined using the Rietveld profile fitting approach.

2-4 Electrochemical techniques

2-4-1 A brief introduction to electrochemistry

An electrochemical reaction is a heterogeneous chemical process involving the transfer of charge to or from an electrode, and current I and potential E are basic quantities to

describe the rate and energy of this reaction, respectively. Equation {2-1-1} sets up the basis of equilibrium electrochemistry, while dynamic electrochemistry studies the kinetics of an electrode reaction including reaction rate and reaction mechanism or steps. The following briefly discusses electrode kinetics.

2-4-1-1 Electron transfer

For a simple electrochemical reaction,

$$O + ne^- \rightleftharpoons R \qquad \{2\text{-}4\text{-}1\}$$

(where O and R are assumed to be soluble), there are at least two sequential steps to maintain a reaction current: (1) *electron transfer* on the surface of the electrode to transfer charge from reactant to the external circuit; (2) *mass transport* in the electrolyte to supply reactant to the electrode surface and also to remove the product.

The term of electron transfer process is also called charge transfer process. For the reaction in {2-4-1} both reduction of O and oxidation of R always take place at an electrode, and the forward and backward reactions produce the partial current densities $\vec{I}$ and $\overleftarrow{I}$, respectively. As a result, there is a net current $I = \vec{I} + \overleftarrow{I}$ at the electrode. By convention, oxidation yields a positive current, reduction a negative current; the electrode at which a net oxidation occurs is called the anode, while the reduction electrode is called the cathode. The magnitude and sign of the net current I depends on the potential E applied to the electrode.

At the equilibrium potential E_e, $\vec{I}$ and $\overleftarrow{I}$ are equal, and so no net current flows. The absolute value of the partial current density at equilibrium is known as the *exchange current density* I_0 which is an important parameter in the description of the kinetics of electrode reactions. The equilibrium potential E_e follows the Nernst equation $E_e = E_e^{\theta} + \frac{RT}{nF}\ln\frac{c_O^s}{c_R^s}$ where c_O^s and c_R^s are the concentrations of O and R on the

electrode surface (note here that the activity coefficients of O and R are assumed to be unity). E_e and I_0 together characterise the equilibrium situation at an electrode.

This equilibrium will be disturbed when the electrode is no longer fixed at E_e. Thus the *overpotential* η is defined as $\eta = E - E_e$. If a potential more negative than E_e is applied to the electrode, a net cathodic current appears ($I = \vec{I} + \overleftarrow{I} < 0$). Conversely, if the potential of the electrode is made positive to E_e, a net anodic current will flow ($I = \vec{I} + \overleftarrow{I} > 0$). Now the net current density is expressed in terms of I_0 and overpotential η:

$$I = \vec{I} + \overleftarrow{I} = I_o\left[\exp\left(\frac{\alpha_A nF\eta}{RT}\right) - \exp\left(-\frac{\alpha_C nF\eta}{RT}\right)\right] \qquad \{2\text{-}4\text{-}2\}$$

where α_A and α_C are constants known as the transfer coefficients for the anodic and the cathodic reactions, and are related to each other by $\alpha_A + \alpha_C = 1$. The Butler-Volmer equation {2-4-2} is a very important one in electrode kinetics. At high overpotential, it can be simplified to

$$\log I = \log I_o + \frac{\alpha_A nF}{2.3RT}\eta, \quad (|\overleftarrow{I}| \gg |\vec{I}|, \text{ anodic polarisation}) \qquad \{2\text{-}4\text{-}3\}$$

or

$$\log -I = \log I_o - \frac{\alpha_C nF}{2.3RT}\eta; \quad (|\vec{I}| \gg |\overleftarrow{I}|, \text{ cathodic polarisation}). \qquad \{2\text{-}4\text{-}4\}$$

Equation {2-4-3} and {2-4-4} are called Tafel equations. When η is very small ($\ll RT/\alpha_C nF$), the Butler-Volmer equation may be linearised

$$I = I_o\frac{nF}{RT}\eta. \qquad \{2\text{-}4\text{-}5\}$$

It is obvious that parameters I_0, α_A and α_C are easily determined from {2-4-3} to {2-4-5} compared with the Butler-Volmer equation {2-4-2} and in practice one usually controls experimental conditions to realise either of these extreme conditions.

2-4-1-2 Mass transport

In general, it is necessary to consider three modes of mass transport for an electrochemical system,: (1) *diffusion*, the movement of a species down a concentration gradient; (2) *migration*, the movement of charged species due to a potential gradient; (3) *convection*, the movement of a species due to mechanical forces. However, the diffusion process is the only form of mass transport for electrochemical species which need be considered when the electrochemical reaction is carried out in an unstirred solution and with the presence of a mass of supporting electrolyte.

The simplest model for the diffusion process is that of linear diffusion to a plane electrode; it is assumed that the electrode is perfectly flat and of infinite dimensions compared with the thickness of diffusion layer, so that concentration variations can only occur perpendicular to the electrode surface. Such a diffusion is described by Fick's laws in a one dimensional form:

(1) *Fick's first law* states the flux j_i of any species i through a plane parallel to the electrode surface is given by

$$-j_i = D_i \frac{\partial c_i}{\partial x} \qquad \{2\text{-}4\text{-}6\}$$

where D_i is the diffusion coefficient and typically has the value 10^{-5} $cm^{-2}s^{-1}$ for species in solution [33]. When applied at an electrode surface, Fick's first law can relate the current density to the chemical change at the electrode:

$$I = -nFD_o\left(\frac{\partial c_o}{\partial x}\right)_{x=0} \quad or \quad I = nFD_R\left(\frac{\partial c_R}{\partial x}\right)_{x=0}. \qquad \{2\text{-}4\text{-}7\}$$

(2) *Fick's second law* describes the change in the concentration of species i with time due to diffusion

$$\frac{\partial c_i}{\partial t} = D_i \frac{\partial^2 c_i}{\partial x^2}. \qquad \{2\text{-}4\text{-}8\}$$

The solution of Fick's second law {2-4-8} gives the variations of the concentrations of O and R with time as well as distance from the electrode. By substituting the solution

c(x, t) into {2-4-7} the variation of reaction current with time I(t) is given. At the extreme case of steady state, current appears as

$$I_L = -\frac{nFD(c_O^s - c_O^\infty)}{\delta} \quad or \quad I_L = -\frac{nFD(c_R^\infty - c_R^o)}{\delta} \qquad \{2\text{-}4\text{-}9\}$$

where c^∞ is the bulk concentration and δ is the diffusion layer thickness. This is called diffusion current.

In order to integrate equation {2-4-8}, initial and boundary conditions appropriate to a particular experiment must be known. This is the basis of the theory of instrumental methods such as chronopotentiometry, chronoamperometry, and cyclic voltammetry. However, one of the boundary conditions is usually semi-infinite diffusion: $c_i(\infty, t) = c_i^\infty$.

2-4-1-3 Control step

Since an electrode process consists of several steps, and even the simplest reaction involves electron transfer and mass transport, the rate of the overall reaction (i.e. current density) will depend on the slowest step. One calls this the rate controlling step. In general, there are three different kinetic characteristics depending on experimental conditions:

(1) charge transfer control, in this case mass transfer is fast and so the overall kinetics is controlled by the reaction at the surface, i.e. the Butler-Volmer equation {2-4-2};

(2) diffusion control, the surface concentration of reactant c^s decreases from c^∞ effectively to zero and consequently the current density becomes independent of potential, at this situation the equation {2-4-9}with c^s = 0 describes the electrode kinetics;

(3) mixed control, the surface concentration c^s becomes significantly less than c^∞ and so reaction current should follow the equation {2-4-8} or the modified Butler-Volmer equation $I = I_o\left[\frac{c_O^s}{c_O^\infty}\exp\left(\frac{\alpha_A nF\eta}{RT}\right) - \frac{c_R^s}{c_R^\infty}\exp\left(-\frac{\alpha_C nF\eta}{RT}\right)\right]$.

The discussion above only involves the simplest electrode process. In fact, an electrode reaction may involves other processes such as coupled chemical reactions, adsorption process, and/or phase formation, e.g. electrodeposition or metal anodic dissolution, etc.. These situations are extensively discussed in [33-35].

2-4-1-4 Characteristics of intercalation electrodes

Electrochemical intercalation is a special class of electrode reactions: the electron transfer does not involve the heterogeneous transmission of electrons across the interface of solid electrode/liquid solution [36]. Instead the electrons are supplied to the electrode from the external circuit and enter the electrode simultaneously with the ion which enter from the solution. Within the electrode and to a good first approximation the ion and electron are not closely associated but exist as separate entities. This is similar to reduction of ion form solution and formation of mercury amalgams. The electrode reaction may include the desolvation of an ion from the solvent, adsorption of the ion on the electrode surface, diffusion across the surface and then incorporation into the electrode [36]. This mechanism, which is more complicated than a simple redox reaction in solution, is more akin to the electrodeposition of metal except that there is no e^- transfer at the interface and the ions are inserted into the lattice rather than growing a further layer on it. Furthermore, diffusion of species occurs not only in the electrolyte but also within the solid electrode (see **2-1-3-2**). The chemical diffusion coefficients $\tilde{D}_{Li}$ of some intercalation compounds are listed below

	TiS_2	$LiNiO_2$	$LiCoO_2$
$\tilde{D}_{Li}$ ($cm^{-2}s^{-1}$)	$1x10^{-8}$ [37]	$2x10^{-7}$ [38]	$3.5x10^{-8}$ [39]

which may be compared with the typical value 10^{-5} $cm^{-2}s^{-1}$ for the diffusion in the liquid electrolyte [33]. Obviously, diffusion in the bulk host is much slower than that in solution electrolytes and so diffusion at the interface region is almost always limited by the diffusion process in solid host. Because electron transfer at an intercalation electrode is directly from the external circuit to the energy bands of the solid host, the electrode potential does not have a major influence on the electron transfer process [36]. However, this situation only occurs for a host material that possesses a high electronic conductivity [40]. A treatment of poor electronic conduction is more complicated [1].

2-4-2 Cyclic voltammetry

Cyclic voltammetry is a basic but useful electrochemical technique to characterise redox behaviour of a substance.

2-4-2-1 Experimental

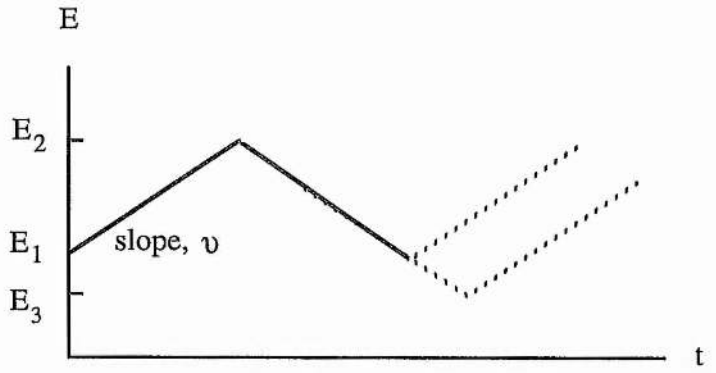

Fig 2-4-1 Potential-time profiles for sweep voltammetry

The potential-time waveforms used for sweep measurements are shown in Fig 2-4-1. The simplest of the these techniques is linear sweep voltammetry (LSV), and this involves sweeping the electrode potential between limits E_1 and E_2 at a known sweep rate, υ. A generally more useful technique is cyclic voltammetry (CV). In this case the waveform is initially the same as in LSV, but on reaching the potential E_2 the sweep is

reversed (usually at the same scan rate) rather than terminated. On again reaching the initial potential E_1, there are several possibilities. The potential sweep may be halted, again reversed, or alternatively continued further to a value E_3. In both LSV and CV experiments the cell current is recorded as a function of the applied potential.

2-4-2-2 Characterisation of electrode reaction

For the CV experimental technique, the mathematical treatment of the equation {2-4-8} with corresponding initial and boundary conditions is somewhat complicated. However, the cyclic voltammogram for a reversible reaction is characterised by the plot in Fig 2-4-2, where a pair of symmetric redox peaks with the peak currents I_p^C and I_p^A appear at the potentials of E_p^C and E_p^A, respectively. For a totally irreversible reaction, the reverse peak will be absent, see Fig 2-4-3, because the corresponding reaction cannot be completed within the timescale of the sweep when the electrode reaction is too slow. As can be seen, cyclic voltammetry readily indicates the potentials of redox reactions and the reversibility of reactions. The possible existence of other processes such as adsorption is also in the profile of cyclic voltammograms [34, 35]. Therefore, this technique is almost always the technique of choice when investigating a system for the first time.

2-4-2-3 Intercalation electrodes

For an intercalation electrode, the main difference is that the diffusion process is very much slower than in solution and hence dominates the kinetics. It is necessary to use very slow sweep rate in order to examine the intercalation reaction. In general, the rate of potential sweep falls in the range of several microvolts per second.

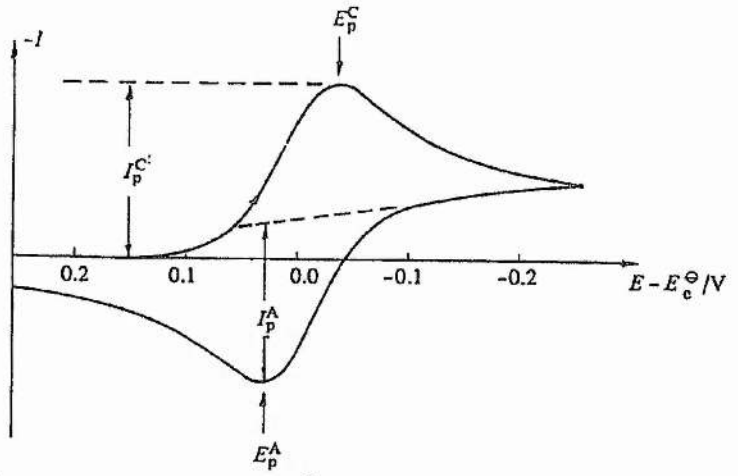

Fig 2-4-2 Cyclic voltammogram for a reversible process O + e ⇌ R. Initially only O is present in solution. E is the potential of the working electrode and E_e^o is the standard electrode potential of the reaction.

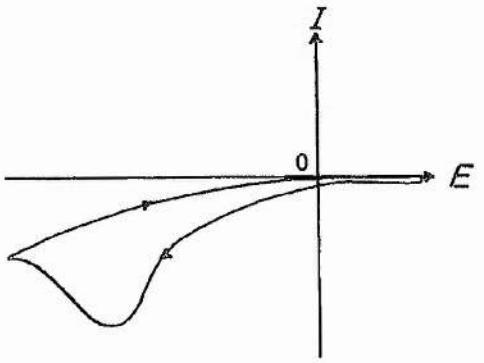

Fig 2-4-3 Schematic cyclic votammogram expected from an irreversible process of the form O + e → R. E is the potential of the working electrode.

2-4-3 Ac impedance

Ac impedance is a powerful technique which is very useful for the study of electrode processes.

2-4-3-1 Basic concepts

The ac impedance technique uses a sinusoidal electrical signal with a small amplitude, often being a voltage signal

$$E = \Delta E \sin \omega t \quad (usually, \Delta E = 10mV) \qquad \{2\text{-}4\text{-}10\}$$

to perturb the electrode reaction under investigation. The resulting current is then recorded over a frequency range

$$I = \Delta I \sin(\omega t + \phi). \qquad \{2\text{-}4\text{-}11\}$$

The relationship between V and I is known as the impedance and in such studies models for different electrochemical process, charge transfer, diffusion, adsorption, etc., are developed and their impedances calculated. The model that best fits the data is taken as the correct description for the system under study. A useful tool is to represent reaction and ion conduction by resistance and the double layer or adsorption by capacitance. Thus, an electrode process is analogised to an electronic network consisting of resistors and capacitors. This network is called equivalent circuit and described by a complex plane. Fig 2-4-4 shows two simplest circuits, RC series and RC parallel. Parallel combination of a resistor and capacitor gives rise to a semicircle in the complex plane whereas a series PC combination gives rise to a vertical spike.

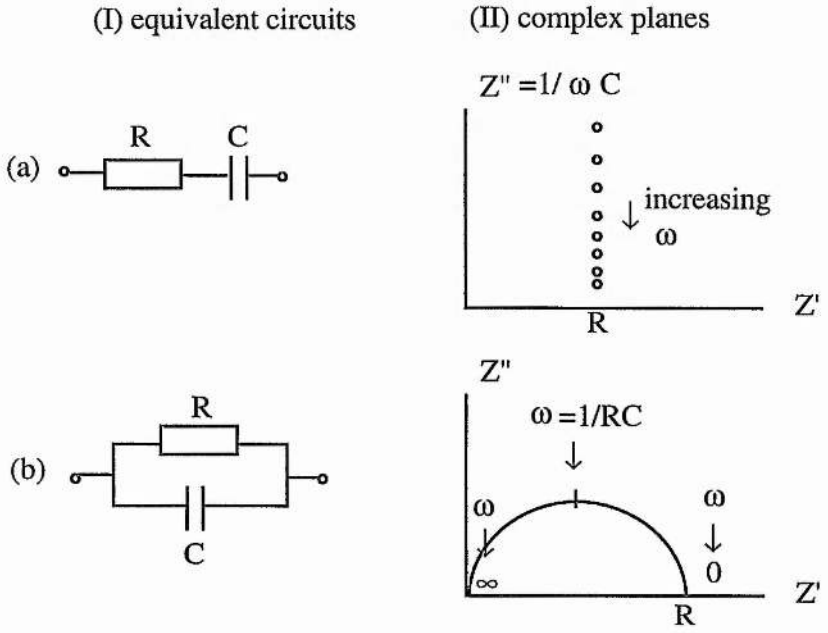

Fig 2-4-4 Two basic equivalent circuits and their complex planes.

2-3-3-2 Impedance for a simple electrode reaction

For a simple electrode reaction {2-4-1}, there are only electron transfer and mass transport processes. The electron transfer process is expressed by a resistance R_f, called as the Faradaic resistance or charge transfer resistance. For a system at dc equilibrium (i.e. only perturbed by the ac signal) then

$$R_f = \frac{RT}{nFI_o}. \qquad \{2\text{-}4\text{-}12\}$$

The mass transport process in the form of diffusion is described by a frequency-dependent resistance, Z_W, called Warburg impedance,

$$Z_w = \frac{\sigma}{\omega^{1/2}}(1-j) \qquad \{2\text{-}4\text{-}13\}$$

where $\sigma = \frac{RT}{2^{1/2}z^2F^2AD^{1/2}}\left[\frac{1}{c_O^\infty} + \frac{1}{c_R^\infty}\right]$ (A, electrode area; D, diffusion coefficient for species in solution; c_O^∞ and c_R^∞ are bulk concentrations). Because the two processes are sequential, their impedances are connected in series in the equivalent circuit. This series is known as the Faradaic process.

In addition, one must consider the effect of the double layer which is always present at the electrode/electrolyte interface [33-34]. It induces a transition current, i.e. nonfaradaic current, and is represented by C_{dl}. The faradaic current must cross this double layer and hence the faradic and nonfaradic processes are connected in parallel. Moreover, all these currents must pass through the electrolyte resistance R_l between the working and reference electrodes. Therefore, a series-parallel configuration, as shown in Fig 2-4-5, describes this simplest electrode processes. This is known as the *Randles equivalent circuit*.

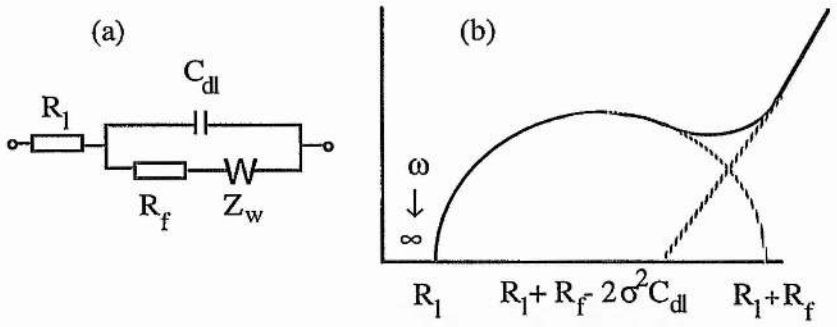

Fig 2-4-5 (a) Equivalent circuit for an electrode reaction with double layer capacitance C_{dl} and uncompensated resistance R_l . The electrode reaction impedance has been resolved into the charge transfer resistance R_f and a Warburg impedance Z_w. (b) Complex plane impedance plot for the circuit of (a).

2-4-3-3 Intercalation electrodes

An analysis similar to the above is still valid to an intercalation electrode, but as mentioned above the intercalation electrode reaction is more complex than a simple redox reaction in that desolvation, adsorption and incorporation of ion in the lattice. The appropriate equivalent circuit is shown in Fig 2-4-6 [36]. The circuit is similar to the Randles but with an extra parallel RC element corresponding to the energy stored by adsorption of the ion on the electrode surface C_{latt} and the lattice incorportion step R_{latt}. This gives rise to two semicircles in the complex impedance diagram. Note that if either R_f or R_{latt} dominates then only one semicircle may be evident and the circuit as well as the impedance resemble to that of Randles. Ionically conducting layers may grow on the surface of intercalation electrodes when in contact with liquid electrolyte or solid polymer electrolytes. Such layer may be represented by adding a parallel combination of a resistor and capacitor in series with the Randles equivalent circuit. The resistor and capacitor in the additional parallel RC element correspond to ion transport and polarisation in the surface layer, respectively. This parallel RC element gives rise to an additional semicircle at high frequency [36, 41]. There may be two separate semicircles in the complex plane depending RC constants.

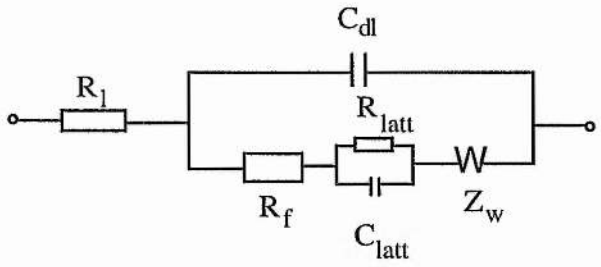

Fig 2-4-6 An equivalent circuit for an intercalation electrode.

Whether the Randles equivalent circuit or a modified circuit of the Randles are used to described the intercalation electrode, there are two special cases for the case of intercalation electrodes. (1) *Constant-phase-angle* Powdered rather than single crystal intercalation electrodes are generally used. The pressed powder electrode has a rough and porous surface. Such a surface produces an effect which can be described by a transmission-line equivalent circuit [41]. This in turn gives rise to an impedance which is expressed mathematically as constant-phase-angle (CPE) [41. 42]:

$$Z_w^{'} = A_w^{'}(j\omega)^{-m} \qquad 0 < m < 1.$$

Such equivalent circuit is then given in Fig 2-4-7.

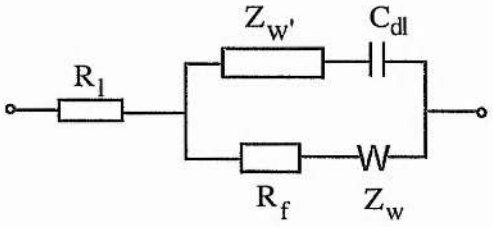

Fig. 2-4-7 A equivalent circuit for a porous electrode.

(2) *Finite diffusion within host* A practical intercalation electrode is almost always thin either because it is a thin film or because of small particle in the powder. As a result, the

diffusion process within the host is confined within a finite geometric dimension [40], illustrated as follows

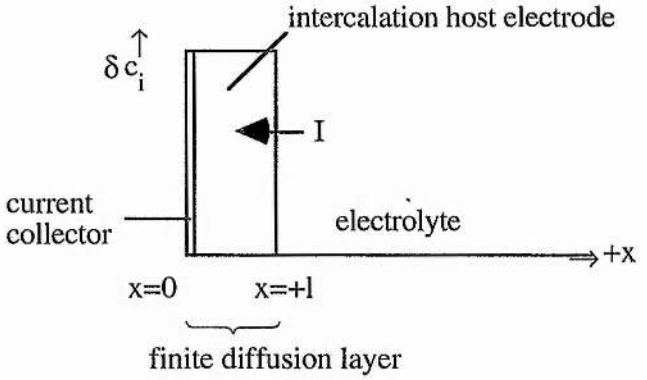

In this situation, a finite-diffusion boundary condition rather than a semi-infinite diffusion condition should be applied to equation {2-4-8}. Warburg impedance at high frequencies remains the form of equation {2-4-13}, implying that a semi-infinite diffusion is still effective within a short timescale. However, at very low frequencies and for a very thin electrode or with a large $\tilde{D}$ the Warburg impedance becomes a vertical line in complex plane [40]. Fig 2-4-8 schematically describes the complex plane of an intercalation electrode over the whole frequency range.

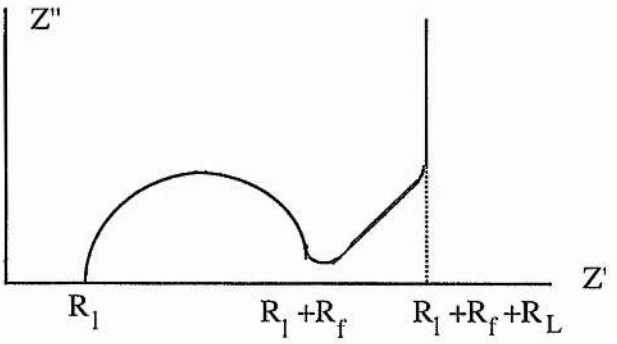

Fig 2-4-8 Schematic complex plane for a thin intercalation electrode.

2-4-3-4 Determination of chemical diffusion coefficient

Based on the Warburg impedance of an intercalation electrode at high frequencies ($\omega >> 2\tilde{D}/l^2$)

$$Z_w = \frac{\sigma}{\omega^{1/2}}(1-j) \qquad \text{with} \qquad \sigma = \frac{V_M(dE/dx)}{\sqrt{2}zF\tilde{D}^{1/2}A}, \qquad \{2\text{-}4\text{-}14\}$$

or at low frequencies ($\omega << 2\tilde{D}/l^2$)

$$R_L = \frac{V_M}{zFA}\left(\frac{dE}{dx}\right)\left(\frac{1}{3\tilde{D}}\right), \qquad \{2\text{-}4\text{-}15\}$$

where V_M is the molar volume of the intercalation compound and the value of dE/dx is measured from open circuit voltage curve, the chemical diffusion coefficient of the intercalation compound can be determined from ac impedance data [40]. Another widely used method to determine the chemical diffusion coefficient is the current pulse technique, called GITT (galvanostatic intermittent titration technique) [43].

Both methods involve knowing the parameters V_M and dE/dx [40, 43-45], but in some cases their determinations may be difficult [46]. In fact the appearance of V_M and dE/dx is to express the concentration of reactant [40, 43]. as can be seen by comparing equations {2-4-14} with {2-4-13} (assuming the concentration of R in {2-4-13} as zero). The concentration of reactant is also calculated based on the geometric volume of electrode and the weight of intercalation compound [46] and then {2-4-13} is used. The two equations have been used in many papers [37-39, 46-52]. However, the use of equation {2-4-13} does assume that the activity coefficient does not change with concentration over a range which may be a false assumption.

2-4-4 Microelectrodes

Electrodes of micrometer dimensions were little used in electrochemical research before 1980, but interest in them has increased exponentially during the past decade. A microelectrode may be defined as an electrode with properties that depend on its size, typically with dimensions comparable to the thickness of the diffusion layer [53].

2-4-4-1 Characteristic features

Owing to its micrometer size, the edge effect of a microelectrode become significant, even at a planar surface. Fig 2-4-9 schematically describes diffusion fluxes to microelectrodes. The diffusion flux at a microelectrode is convergent to the surface of electrode, so that compared with the equation {2-4-7} for a large and effectively infinite planar electrode, Fick's second law for a microelectrode becomes

$$\frac{\partial c_j}{\partial t} = D_j\left[\frac{\partial^2 c_j}{\partial r^2} + \frac{1}{r}\frac{\partial c_j}{\partial r} + \frac{\partial^2 c_j}{\partial z^2}\right] \qquad \{2\text{-}4\text{-}16\}$$

where r is the distance from the centre of the electrode in the plane of its surface, and z is the perpendicular distance from the electrode surface. As the result of reduction in size of an electrode, three major consequences arise: (1) mass transport rates to and from the electrode are increased because of nonplanar diffusion; (2) the double-layer capacitance is reduced due to the reduction in surface area; and (3) ohmic drop, which is the product of electrode current and solution resistance, is reduced due to the diminished current. These properties provide a starting point for the application of microelectrodes to electrode kinetics, electroanalytical chemistry and others. The following is going to focus on the third characteristic of the microelectrode which makes it possible to carry out electrochemical studies in highly resistive media .

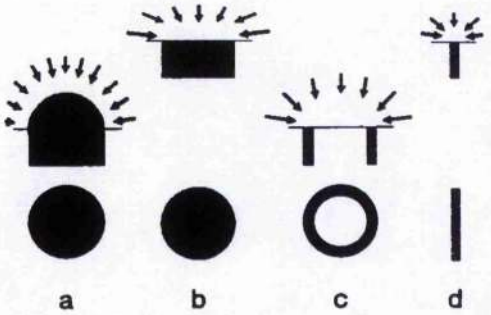

Fig 2-4-9 Convergent flux to small sphere (a), disk (b), ring (c) and band (d) electrodes. Top: side view; bottom: plane view of the microelectrodes.

2-4-4-2 iR drop at a microelectrode

The electrical resistance of a microelectrode system includes two contributions: the resistance of the body of a microelectrode itself (R_m) and the resistance in solution between the microelectrode tip and a secondary electrode (R_s). In general R_s is greater than R_m. One can calculate R_s from the (specific) conductivity of the electrolyte, κ. For a microscopic hemispherical electrode, the contribution to the resistance dR_s by an element of area $4\pi r^2$ and thickness dr is given by

$$dR_s = \frac{1}{\kappa}\frac{dr}{2\pi r^2}. \qquad \{2\text{-}4\text{-}17\}$$

If the second electrode is placed at a large and effectively infinite distance from the microelectrode, the resistance R_s is obtained by integration between r_o and ∞

$$R_s = \int_{r_o}^{\infty}\frac{dr}{2\pi\kappa r^2} = \frac{1}{2\pi\kappa r_o} \qquad \{2\text{-}4\text{-}18\}$$

Although the resistance R_s is undoubtedly high and increases as the radius of the microelectrode is made smaller, the value of R_s per unit area of electroactive surface is low and lowers with decreasing radius of the microelectrode, as shown in Table 2-4-1 which presents the values of R_s and the products of R_s and the geometric surface area A for Pt electrodes with various radii immersed in 0.1 M KNO_3 solution.

In a conventional three-electrode cell, the electrical contact between working electrode and reference electrode is often made through a Luggin capillary so as to reduce the effects of electrolyte resistance on the controlled potential. In order to eliminate the solution resistance, the tip of the Luggin capillary is better close to the working electrode. For practical reasons and to avoid deformation of the electric field near the working electrode, however, the tip of the Luggin capillary is nevertheless at a significant distance from the electrode. Thus an uncompensated resistance is present which introduces an error into the value of the controlled potential, proportional to the current passing through the call. This is called iR drop and usually needs compensating

through the electronic circuit [34, 53]. By contrast, the use of microelectrodes can make iR drop negligible. Table 2-4-1 presents an example. Since iR drop can be neglected, it is possible to use a two-electrode cell based on a microelectrode but without the interferences of iR drop on the potential of the micro-working electrode. In this type of two electrode cell, the second electrode (i.e. counter electrode) usually has a much larger area so that the current density passing through it can reduce further. As a result, the electrode maintains at equilibrium with the electrolytic solution, acting like a reference electrode in a three electrode cell. This is the basis of studying the electrochemistry of organic solvents alone without deliberately addition of a supporting electrolyte by using a microelectrode in a two-electrode cell.

Table 2-4-1 Resistance of Hemispherical Pt microelectrodes immersed in aqueous 0.1 M KNO_3 solution (quoted from [53]).

r_o (μm)	R_m (Ω)[a]	R_s (kΩ)[b]	10^3RA (Ωcm^2)[c]
∞	–	–	6.90[d]
50	0.135	2.20	0.345
25	0.542	4.39	0.172
10	3.39	11.0	0.0690
5	13.5	22.0	0.0345
1	339	110	0.00692

[a] Microwire of length 1 cm, with $\sigma_{pt} = 9.4 \times 10^4\ \Omega^{-1}\ cm^{-1}$.

[b] For hemisphere, with $\kappa = 0.0145\ \Omega^{-1}\ cm^{-1}$.

[c] Product of R and geometric surface area.

[d] Planar electrode with Luggin tip 1 mm from the surface.

2-5 Battery studies

2-5-1 Basic concepts

A battery is a device which can store chemical energy and, on demand, convert it into electrical energy to drive an external circuit [54]. The transformation between chemical energy and electrical energy follows the equation {2-1-1}. A battery consists of a single cell or several cells which are connected in parallel or series [55]. The basic elements of a cell which can act as a power source are shown in Fig 2-5-1. As indicated above, oxidation occurs at the *anode* and reduction at *cathode*. In a battery as opposed to an electrolysis cell, the anode is the *negative electrode* and the cathode the *positive electrode* because the former releases electrons (by oxidation), while the latter collects electrons from the external circuit (by reduction). The charging process is just opposite to the above.

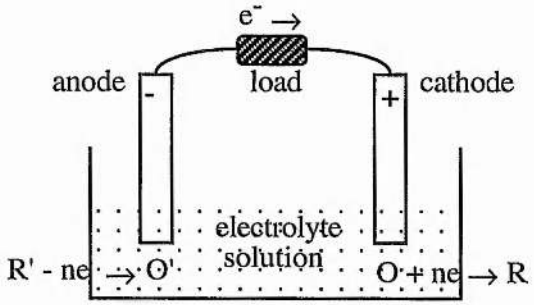

Fig 2-5-1 A schematic cell and electrode reactions at cathode and anode, respectively.

2-5-2 Battery characteristics: cell voltage, capacity, energy density and discharge rate

The energy stored in a battery is often measured by discharging the battery at an given current. The energy in Watt-hour (Wh) is the product of average operating voltage in volt (V) and discharge capacity in ampere-hour (Ah). Thus the major characteristics of a battery are cell voltage (intensive quantity) and cell capacity (extensive quantity).

Cell voltage is equal to the potential difference between the two electrodes and conventionally this is taken as the potential of the positive electrode minus the potential of the negative electrode

$$E_{cell} = E^{+} - E^{-} \qquad \{2\text{-}5\text{-}1\}$$

where the subscripts of + and - are representative of the positive and negative electrodes, respectively. If no current (or negligible current) flows, the equation {2-1-1} gives the cell voltage under equilibrium conditions, i.e. open circuit voltage (OCV) or electromotive force (EMF). This is equivalent to the difference in the Fermi levels between the positive and negative electrodes. Once a net electrochemical reaction starts, i.e. a current passing through the external circuit, the reaction deviates from thermodynamic equilibrium, as illustrated in Fig 2-5-2 where the anode's potential shifts positively from its thermodynamic value E_e^- while the cathode's potential shifts negatively from its E_e^+. In addition, there is a voltage drop associated with the current flowing through the electrolyte resistance, iR_{cell}. As a result, the cell voltage during discharging is expressed as

$$E_{cell} = E_e^+ - E_e^- - |\eta_+| - |\eta_-| - iR_{cell} \qquad \{2\text{-}5\text{-}2\}$$

where the value of $E_e^+ - E_e^-$, i.e. OCV, is determined by {2-1-1}. Obviously, a good battery should have the smallest possible overpotential when passing large current and the smallest possible electrolyte resistance.

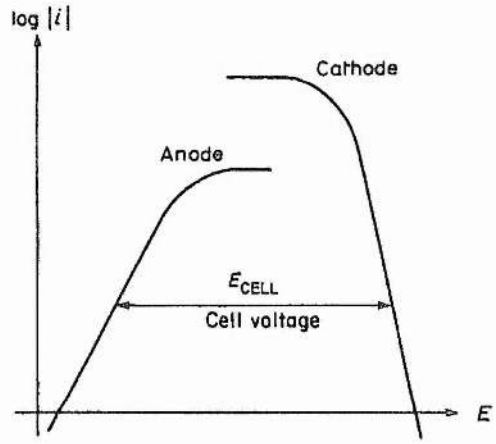

Fig 2-5-2 Plot of log $|i|$ vs. E (vs. a reference electrode) for the cathode and anode of a battery.

Capacity is the charge that may be obtained from the battery. It is usually quoted in ampere hours, Ah. The capacity depends on the size of the electrodes and the electrode of lowest capacity determines the capacity of a given cell. The nominal capacity of an electrode may be calculated from the weight w of the active material via Faraday's Law,

$$C = wnF/M \qquad \{2\text{-}5\text{-}3\}$$

where M is the molar mass of the electrode material, n is the number of electron transferred for each atom and F equal to 26.8 Ah. Sometimes the equation {2-5-3} is alternatively written as

$$C = nF/M \qquad \{2\text{-}5\text{-}4\}$$

called the *specific theoretical capacity* of the electrode material. This is a measure of a capacity per unit weight of electrode material and is thus characteristic of the type of electrode not its size.

Probably the most important characteristic of a battery is the energy stored. Since energy is an extensive quantity, i.e. double the size of the cell will double the energy stored then the most useful quantity is to divide the energy by the weight to yield the gravimetric energy density or volume to yield the volumetric energy density

$$Energy \quad density = \frac{capacity \times cell \quad voltage}{weight},$$

$$Energy \quad density = \frac{capacity \times cell \quad voltage}{volume}.$$

These are the most useful parameter when comparing different battery types.

Discharge rate is critical to cell performance. It will determine whether a cell will be useful for low or high current application. As indicated in Fig 2-5-2, the cell voltage decreases as the discharge current increases. The discharge rate is defined as C/n or n-

hour rate, which means that at a given current I the nominal capacity C of the electrode will be discharged in n hours [54].

2-5-3 Half-cell study

In a battery any electrical measurement involves the response of both electrodes. When attempting to optimise each electrode of the battery, it is essential to separate out the response of the positive and negative electrodes. This can be achieved by the use of a third , reference, electrode. The current flows through the cell continuing to be past between the positive and negative electrodes, but the voltage of the electrode under study, the working electrode, is measured with respect to the reference through which a negligible current passes. In this way the full voltage and current of only the working electrode will be measured. The reference electrode has to have a constant potential. In battery studies the use of a three electrode system is called half-cell study. This thesis concerns mainly the performance of the cathode materials based on lithium manganese oxides. It is evidently convenient to use a Li electrode as reference electrode for investigating lithium cells. Thus, two lithium electrodes along with an electrode based on lithium manganese oxides were employed to construct a three electrode cell in these studies.

A frequently carried out measurement in this thesis is the establishment of the charge and discharge capacities obtained between fixed voltage limits and at a constant current. Fig 2-5-3 shows schematically the charge and discharge curves of a working electrode. From this curve, the practical specific discharge capacity Q_d of the electrode can be determined by

$$Q_d = \frac{I \times (t_{i+2} - t_{i+1})}{w}$$

where w is the weight of the electrode material. The capacity during charging can be obtained in a similar way.

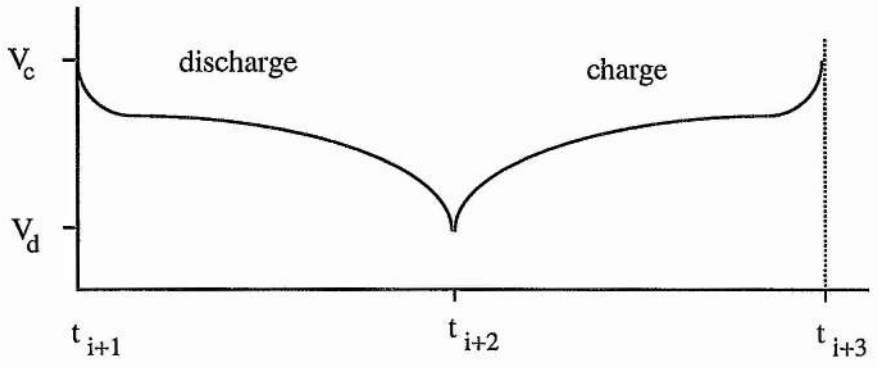

Fig 2-5-3 Schematic discharge and charge cureve at a constant current I between voltage limits V_d and V_c.

References

[1] Chemistry of Solid State Materials Solid State Electrochemistry, edited by P.G.Bruce, Cambridge University Press, 1995.

[2] D.W.Murphy, and P.A.Christian, Science, **205** 651 (1979).

[3] K.West, Intercalation Compounds—Metal ions in Chalcogenide and Oxide hosts, in High Conductivity Solid Ionic Conductors Recent Trends and applications, edited by T.Takahashi, World Scientific Publishing Co. Pre. Ltd., 1989.

[4] W.R.Mckinnon, and R.R.Haering, Physical Mechanisms of Intercalation, in Modern Aspects of Electrochemistry, edited by White, Bockris and Conway, Plenum Press, 1983.

[5] Jean-François Fauvarque, Chemical Physics of Intercalation; NATO ASI Series, Series B: Physics, **172** 291 (1987).

[6] W.R.Mckinnon, Chemical Physics of Intercalation; NATO ASI Series, Series B: Physics, **172** 181 (1987).

[7] C.Delmas, Chemical Physics of Intercalation; NATO ASI Series, Series B: Physics, **172** 209 (1987).

[8] R.Schöllhorn Chemical Physics of Intercalation; NATO ASI Series, Series B: Physics, **172** 149 (1987).

[9] D.W.Murphy, S.A.Sunshine, and S.M.Zahurak, Chemical Physics of Intercalation; NATO ASI Series, Series B: Physics, **172** 173 (1987).

[10] Recent Advances in Rechargeable Li Batteries, edited by J.M.Tarascon, Solid State Ionics, **69** (Special Issue) (1994).

[11] W.Weppner, and R.A.Huggins, Ann. Rev. Mater. Sci., **8** 269 (1978).

[12] G.J.Dudley, and B.C.H.Steele, J. Solid State Chem., **31** 233 (1980).

[13] W.Weppner, and R.A.Huggins, J. Electrochem, Soc., **124** 1569 (1977).

[14] D.M.Adams, Inorganic Solids Introduction to Concepts in Solid-State Structural Chemistry, John Wiley and Sons, (1974).

[15] S.Bach, J.P.Pereira-Ramos, N.Baffier, and R.Messina, Electrochimica Acta, **37** 1301 (1992).

[16] S.Bach, J.P.Pereira-Ramos, N.Baffier, and R.Messina, J. electrochem. Soc., **137** 1042 (1990).

[17] P.G.Bruce, and M.Y.Saidi, Electrochimica Acta, **36** 569 (1991).

[18] C.Ho, I.D.Raistrick, and R.A.Huggins, J. Electrochem. Soc., **127** 343 (1980).

[19] C.John Wen, B.A.Boukamp, and R.A.Huggins, J. Electrochem. Soc., **126** 2258 (1979).

[20] M.Y.Saidi, I.Abrahams, and P.G.Bruce, Mat. Res. Bull., **25** 533 (1990).

[21] A.R.West, Solid State Chemistry and its Application, John Wiley & Sons, (1984).

[22] A.Wold, and K.Dwight, Solid State Chemistry—Synthesis, Structure, and Properties of Selected Oxides and Sulfides, Chapman and Hall Inc., (1993).

[23] L.L.Hench, and J.K.West, Chem. Rev., **90** 33 (1990).

[24] J.Livage, C.Sanchez, M.Henry, and S.Doeuff, Solid State Ionics, **32/33** 633 (1989).

[25] J.Livage, Solid State Ionics, **50** 307 (1992).

[26] J.Livage, M.Henry, and C.Sanchez, Prog. Solid State Chem., **18** 259 (1988).

[27] J.P.Pereira-Ramos, N.Baffier, and G.Pistoia, Cathode Materials Synthesized by Low Temperature Techniques, in Lithium Batteries New Material, Developments and Perspectves, edited by G.Pistoia, Elsevier, (1994).

[28] G.Pistoia, M.Pasquali, G.Wang, and L.Li, J. Electrochem. Soc., **137** 2365 (1990).

[29] J.M.Tarascon, and D.Guyomard, J.Electrochem. Soc., **138** 2864 (1991).

[30] J.C.Hunter, J. Solid State Chem., **39** 142 (1981).

[31] R.Gupta and A.Manthiram, J. Solid State Chemistry, **121**, 483 (1996).

[32] G.Dutta, A.Manthiram, J.B.Goodenough, and J.C.Grenier, J. Solid State Chem., **96** 123 (1992).

[33] Southampton Electrochemistry Group, Instrumental Methode in Electrochemistry, Ellis Horwood, (1990).

[34] A.J.Bard, and L.R.Faulkner, Electrochemical Methods Principles and Experimental, John Wiley & Sons, (1980).

[35] J.Koryta, J.Dvorák, and L.Kavan, Principles of Electrochemistry, (Second Edition), John Wiley &Sons, (1993).

[36] P.G.Bruce, and M.Y.Saidi, J.Electroanal. Chem., **322** 93 (1992).

[37] K.Kanehori, F.Kirino, T.Kudo, and K.Miyauchi, J. Electrochem. Soc., **138** 2216 (1991).

[38] P.G.Bruce, A.Lisowska-Oleksiak, M.Y.Saidi, and C.A.Vincent, Solid State Ionics, **57** 353 (1992).

[39] A.Honders, J.M.der Kinderen, A.H.von Heeren, J.H.W.de Wit, and G.H.J.Broers, Solid State Ionics, **15** 265 (1985).

[40] C.Ho, I.D.Raistrick, and R.A.Huggins, J. Electrochem. Soc., **127** 343 (1980).

[41] M.G.S.R.Thomas, P.G.Bruce, and J.B.Goodenough, J. Electrochem. Soc., **132** 1521 (1985).

[42] J.Ross Macdonald, Solid State Ionics, **13** 147 (1984).

[43] W.Weppner, and R.A.Huggins, J. Electrochem. Soc., **124** 1569 (1977).

[44] A.Honders, and G.H.J.Broers, Solid State Ionics, **15** 173 (1985).

[45] A.Honders, E.W.A.Young, A.H.van Heeren, J.H.W.de Wit, and G.H.J.Broers, Solid State Ionics, **9/10** 375 (1983).

[46] N.Takami, A.Satoh, M.Hara, and T.Ohsaki, J. Electrochem. Soc., **142** 511 (1995).

[47] P.G.Bruce, and M.Y.Saidi, Electrochemica Acta, **36** 569 (1991).

[48] J.Faray, R.Messina, and J.Perichon, J. Electrochem. Soc., **137** 1337 (1990).

[49] A.C.W.P.James, and J.B.Goodenough, Solid State Ionics, **27** 37 (1988).

[50] A.C.W.P.James, B.Ellis, and J.B.Goodenough, Solid State Ionics, **27** 45 (1988).

[51] C.John Wen, B.A.Boukamp, and R.A.Huggins, J. Electrochem. Soc., **126** 2258 (1979).

[52] B.V.Ratnakumar, G.Nagasubramanian, S.Di Stefano, and C.P.Bankston, J. Electrochem. Soc., **139** 1513 (1992).

[53] B.R.Scharifker, Microelectrode techniques in electrochemistry, in Modern Aspects of Electrochemistry, edited by J.O.M.Bockris *at al.*, Plenum Press, 467 (1992).

[54] D.Pletcher and F.C.Walsh, Industrial Electrochemistry (second edition), Chapman and Hall Ltd., (1990).

[55] C.A.Vincent, F.Bonino, M.Lazzari, and B.Scrosati, Modern Batteries-an introduction to electrochemical power sources, Edward Arnold (Publishers) Ltd., 1984.

CHAPTER THREE

Experimental

3-1 $LiMn_2O_4$ preparation by conventional solid state reaction

Spinel $LiMn_2O_4$ was prepared by the solid state reaction of Mn_2O_3 and Li_2CO_3 [1]. A mixture of Mn_2O_3 (Alfra 98%) and Li_2CO_3 (BDH 99.5%) with a mole ratio of 2:1 was ground in an agate mortar and pestle for 15-30 minutes and then heated in air in an alumina crucible. The heating procedure involved first calcining samples at 650 °C for 48 hours and then annealing at 850 °C for another 48 hours.

3-2 Physical and chemical characterisations

3-2-1 X-ray diffraction experiments

Lithium manganese oxide powders were analysed by X-ray diffraction using a Phillips diffractometer with Bragg-Brentano geometry and operating with CuK_α radiation (λ = 1.5418 Å). The two Theta (2θ) range over which data were collected was typically from 10° to 80°.

3-2-2 Chemical analysis: potentiometric titration

The oxidation state of lithium manganese oxide spinels was determined using a potentiometric titration method based on that proposed by Vetter and Jeager [2]. The titrating agent was a potassium permanganate solution. The concentration of $KMnO_4$ (M&B AR) solution used was 0.01 M. The apparatus for the potentiometric titration is illustrated in Fig 3-2-1.

The experiment was divided into three steps: firstly, spinel samples were dissolved in Fe(II) acidic solution which consisted of approximate 0.05 M of $FeSO_4$ (Aldrich 99+ %) and 0.05 M of $(NH_4)_2SO_4$ (BDH AnalaR) in a dilute H_2SO_4 solution (10 ml of 98 % H_2SO_4 for 1 litre of solution). Typically, 20 -40 mg of oxide sample were placed in a 250 ml beaker containing 20 ml of the Fe(II)/acid solution and the dissolution reaction permitted to continue with magnetic stirring for about one hour. After this time, dissolution was completed and two titrations using $KMnO_4$ were performed. In the first step, the solution resulting from dissolution was titrated directly with the $KMnO_4$ solution. In the subsequent titration, $Na_4P_2O_7$ (Aldrich a.c.s.Reagent) was added to the solution (typically around 150 ml of saturated $Na_4P_2O_7$ solution was used) before reacting again with the $KMnO_4$ solution. Note that the pH of the solution used in the second titration should be adjusted to between 6 and 7 with H_2SO_4. A pH meter was used for this purpose.

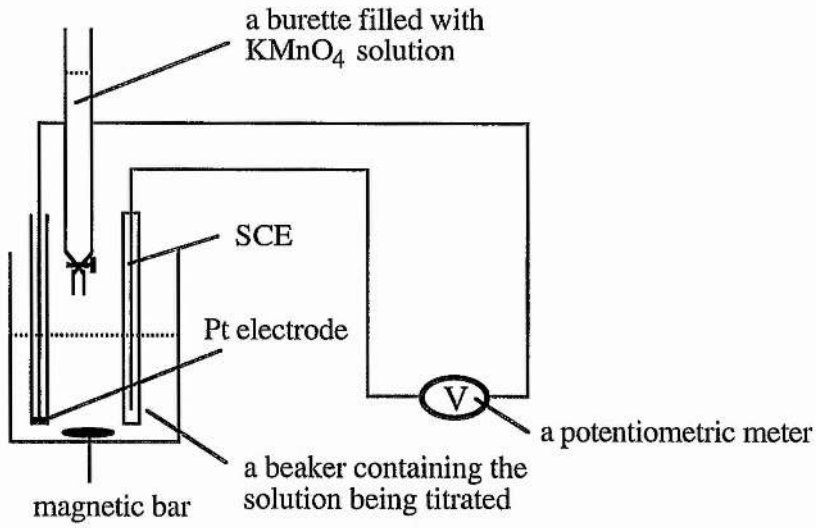

Fig 3-2-1 A schematic diagram of a device for potentiometric titration.

3-2-3 FTIR measurements

FTIR measurements were curried out using a PERKIN ELMER 1710 Infrared Fouriour Transform Spectrometer. All powder samples were diluted with KBr powder (Aldrich 99+% Infrared Grade) by grinding in an agate mortar and pestle, and then pressed into pellets at 10 tons per 1.1 cm^2. The pellets were sandwiched between two KBr plates in a sample holder for FTIR measurements.

3-3 Electrolyte solutions

3-3-1 Purification of solvents and salts

Propylene carbonate (PC) (Aldrich 99+ %, bp: 240 °C) – purified using a Fischer HMS 500 C distillation apparatus with 90 theoretical plates. The temperature of the distillation flask was 120 °C and the head temperature was 57 °C during vacuum distillation. The rate of distillation was about 25 $cm^3 \cdot h^{-1}$.

Ethylene carbonate (EC) (Aldrich 98 %, bp: 243-244 °C / 740 mm) – distilled under reduced pressure (about 20 mm Hg) with a small argon flow. The length of the distilling column was 400 mm. Before distillation, EC was dried over P_2O_5 (Aldrich) for 3 days above its melting point (37-39 °C). The distillation apparatus and the solvent were degassed by 3 pump / refill cycles using argon. The temperature of the column head was 93 °C during distillation. Due to the melting point of EC being above room temperature, it is sometime necessary to warm the end of the condenser in order to avoid crystallisation.

Dimethyl carbonate (DMC) (Aldrich 99 %, bp: 90 °C) – distilled under an argon atmosphere. The length of the column was 400 mm. DMC was dried over 4 Å molecular sieves for 2 days before distillation. The 4 Å molecular sieves were dried at 300 °C under dynamic vacuum for 2 days before use.

Tetraethylene glycol dimethyl ether (Tetraglyme) (Aldrich 99+ %, bp: 275-276 °C) – purified using a Fischer HMS 500 C distillation apparatus with 90 theoretical plates. The temperature of the distillation flask was 147 °C and the head temperature was 90 °C under vacuum distillation. The rate of distillation was about 50 $cm^3 \cdot h^{-1}$.

$LiAsF_6$ (Battery Grade, LITHCO) – used as received.

$LiPF_6$ (Battery Grade, Advance Research Chemical Ltd.) – used as received.

$LiClO_4$ (Aldrich A.C.S. reagent) – dried at 130 °C under dynamic vacuum for 48 hours before use.

$LiSO_3CF_3$ (Aldrich 98 %) – dried at 150 °C under dynamic vacuum for 4 days before use.

3-3-2 Solution preparations

Lithium salts were slowly added to a known volume of organic solvent up to a concentration of 1 molar, for example, 2.1288 g of $LiClO_4$ added to 20 ml of PC solvent. In order to prevent absorption of moisture from the air, all solution preparations were carried out in a MBraun argon filled glove box.

3-4 Cell constructions

3-4-1 Three electrode cell

The three electrode cell used for cell cycling is showed schematically in Fig 3-4-1. Three electrodes are separated from one another by interleaving Whatman GF/F filter pads soaked with electrolyte solution. The cell is tightly pack together by pressing the spigots at the two ends of the cell. The spigots are also used as electrical connectors for the working electrode and counter electrode, respectively. The spigot which contacts

with working electrode is made from stainless steel (SS) or aluminium metal. The electrical connection to an electrochemical instrument for reference electrode is a piece of stainless steel wire on which a lithium ring is pressed. The counter electrode used in this work was also made from lithium metal. The working electrode was a composite containing the intercalation compound, e.g. lithium manganese oxide spinel as well as carbon black and a binder e.g. Teflon. Alternatively, a piece of stainless steel or aluminium gauze was used as the working electrode when studying electrolyte oxidation on substrates.

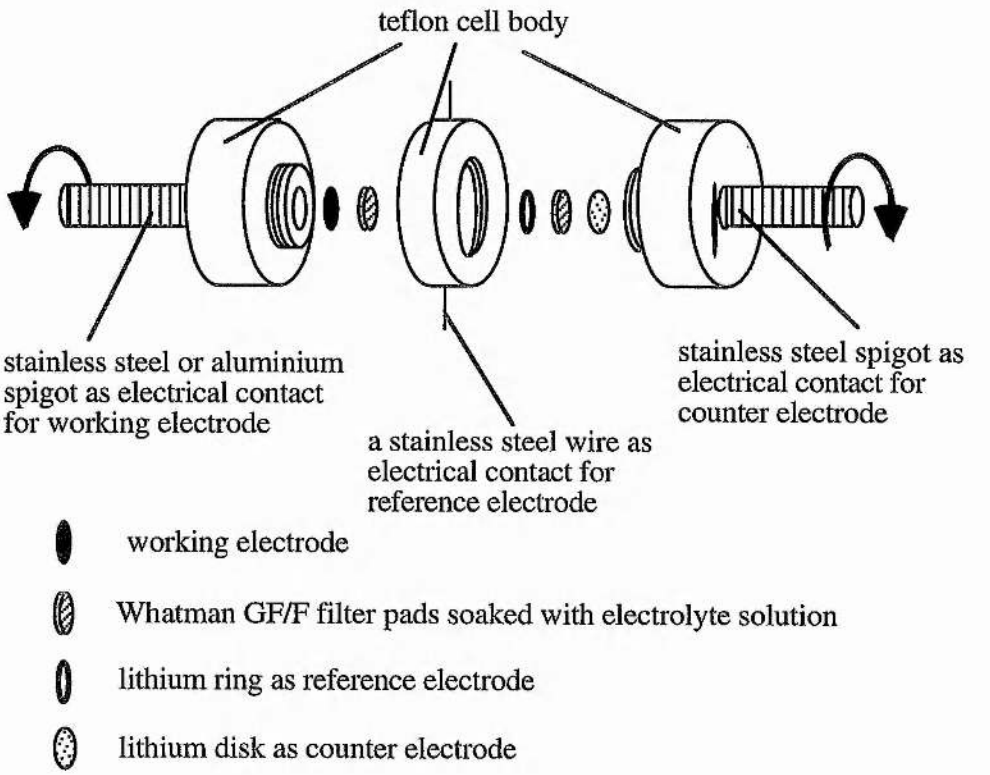

Fig 3-4-1 A three electrode cell

3-4-2 Two electrode cells

Fig 3-4-2 shows a two electrode cell which was used for ex-situ X-ray diffraction. The working electrode was made from the appropriate lithium manganese oxide spinel and this was transferred between the cell and a sample holder for X-ray diffraction.

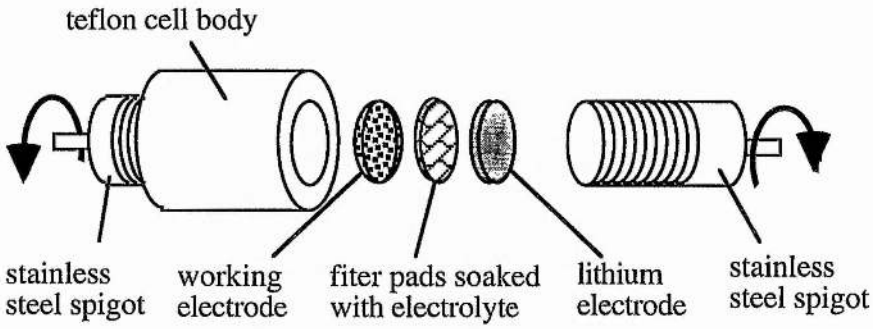

Fig 3-4-2 A two-electrode cell for electrochemical delithiation.

3-4-3 Two electrode cell with microelectrode

A two electrode cell with a microelectrode is shown in Fig 3-4-3.

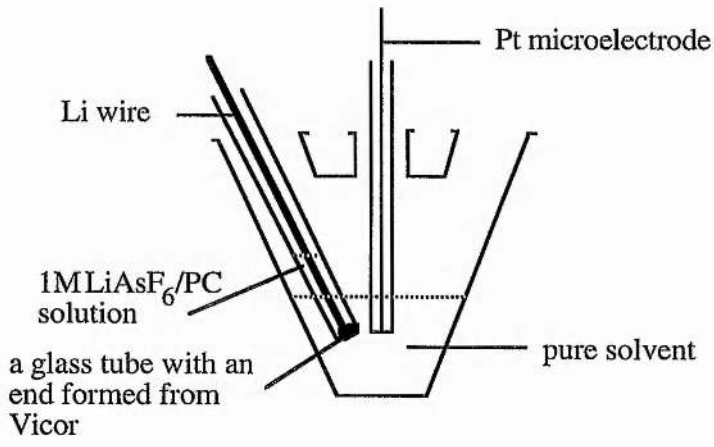

Fig 3-4-3 A two electrode cell for microelectrode electrochemical measurements.

The cell body was made from a glass flask. The working electrode was a 25 μm diameter Pt microdisc sealed in glass. The reference electrode, which also served as the counter electrode, was based upon the model of a Ag / Ag^+ reference electrode design by Kirowa-Eisner and Gileadi [3]. A Vicor disc was sealed onto the end of a glass tube using PTFE heat-shrink tubing. A 1 M $LiAsF_6$/PC solution was placed in the tube and a Li wire was dipped into this electrolyte. The Vicor disc allowed electrochemical

contact between the two electrodes whilst minimising cross-contamination of the different electrolyte substances.

3-5 Composite electrodes and cell assembly

3-5-1 Preparation of composite electrodes

A composite electrode usually contains an intercalation compound, as active material, carbon black, as conducting additive, and some binder, such as PTFE. Except where specifically noted, the composite electrode in the this work was fabricated by dry mixing the appropriate lithium manganese oxide, carbon black and PTFE in the weight ratios 80:13.3:6.7. The weighed mixtures were ground in an agate mortar and pestle and then pressed onto aluminium or stainless steel gauze at a pressure of 5 tons for aluminium gauze or 10 tons for stainless steel gauze. The geometric area of composite electrode was 0.8-0.9 cm^{-2}. The loading on the composite electrode was typically 16 $mg \cdot cm^{-2}$. Finally the entire assembly was dried under vacuum at 80 °C for 12 hours before use.

In addition, another type of composite electrode was fabricated in the same way as the above except for the absence of pressing the composite film onto a metal substrate. A composite film results with ~ 21 mg of active material per square centimetre. These composite films were used for ex-situ X-ray diffraction experiments.

3-5-2 Assembly of two and three electrode cells

A three electrode cell (Fig 3-4-1) was constructed from a composite electrode or metal electrodes such as aluminium and stainless steel as working electrode and two lithium metal electrodes as reference and counter electrodes, respectively. Li^+ electrolyte was soaked into Whatman GF/F filter pads, which acts as separators between the electrodes. Whatman GF/F filter pads were dried at 200 °C under dynamic vacuum for

2 days before used. All manipulations of air sensitive materials as well as the cell assembly used were carried out in a MBraun argon filled glove box from which H_2O and O_2 are continuously removed maintaining levels of less than 1 ppm especially. The cells were placed in an air tight stainless steel can, see Fig 3-5-1, and then moved from the glove box to carry out cycling tests or other electrochemical experiments.

Since all reference electrodes used in this work were formed from lithium metal, the potentials indicated in the thesis all refer to Li/Li^+ (1M).

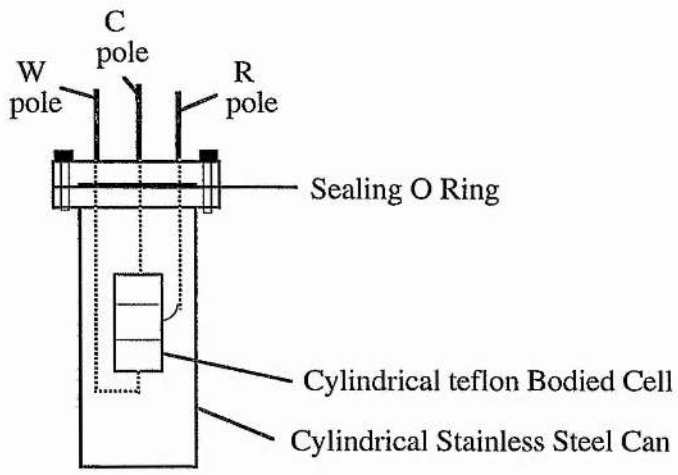

Fig 3-5-1 A schematic stainless steel can to seal a teflon body cell from air.

3-6 Electrochemical experiments

3-6-1 Cycling

Cells were galvanostatically cycled between potential limits; the main potential limits were 4.4 to 3.3 V for 4 volt cells or 3.7 to 2.0 V for 3 volt cells except where specifically noted. Cycling tests were carried out using a Sycopel Scientific Multistat under the control of an IBM PC. All tests were carried out at room temperature.

The specific discharge capacity was calculated from the product of discharge current and discharge time on the basis of the weight of lithium manganese oxide contained in a

given composite cathode. The theoretical capacity of $LiMn_2O_4$ for the two discharge plateaux:

$$\lambda - MnO_2 \xrightarrow{4V} LiMn_2O_4 \quad or \quad LiMn_2O_4 \xrightarrow{3V} Li_2Mn_2O_4$$

can be calculated as

$$Q_T = \frac{1 \times 26800}{180.82} = 148 mAhg^{-1}$$

where the number of electrons transferred is one for each discharge plateau and the molar mass of $LiMn_2O_4$ is 180.82.

3-6-2 Cyclic voltammetry and ac impedance

A three electrode cell was employed for voltammetric and ac impedance experiments. Cyclic voltammetry was carried out using a Biologic MacPile for slow scan experiments, e.g. 10 $\mu V \cdot s^{-1}$, otherwise a Solartron 1286 potentiostat connected with a X-Y chart recorder was used. Ac impedance measurements were carried out using a Solartron 1286 potentiostat and 1250 frequency response analyser, both devices under the control of an IBM PC. Data were collected over the frequency range from $5x10^{-2}$ (or $1x10^{-2}$) to $6.5x10^4$ Hz.

3-6-3 Microelectrode experiments

Voltammetric experiments with microelectrodes were performed by a Solartron 1286 electrochemical interface controlled by an IBM PC computer with Corrware software. The two electrode cell with Pt microelectrode in Fig 3-4-3 was placed in an argon glove box for carrying out these measurements.

References

[1] J.C.Hunter, J.Solid state Chem., **39** 142 (1981).

[2] K.J.Vetter, N.Jeager, Electrochemica Acta, **11** 401 (1966)

[3] E.Kirowa-Eisner, and E.Gileadi, J. Electroanal. Chem., **25** 481 (1970)

CHAPTER FOUR

Electrochemical Stability of Some Liquid Electrolytes for Use in 4V Rechargeable Lithium Batteries

4-1 Introduction

Lithium batteries demand the use of non-aqueous electrolytes. These have been under study since lithium battery research started in the 1950's [1]. Several good reviews are available that give the history of organic electrolyte development [2-3]. Rechargeable lithium batteries place more stringent requirements on organic electrolytes and this has been further heightened by introduction of highly oxidising (i.e. 4 V vs. Li/Li^+) intercalation compounds as cathode materials, such as $LiMn_2O_4$, $LiCoO_2$ and $LiNiO_2$, in the 1980's [1, 4]. Use of these electrodes is essential in lithium ion cells to avoid the otherwise lower cell voltage due to the use of carbon as an anode. For 4 V cathodes and hence lithium ion batteries the issue of electrolyte stability is critical. A stable electrolyte must resist the very oxidising conditions at the cathode and reducing conditions at the anode. Electrolyte oxidation can jeopardise the capacity and cycle life of the cell, as well as compromise the safety of the system by generating, for instance, gaseous reaction products that increase the internal pressure of the cell. However, electrolyte stability at the anode has been extensively studied at lithium and more recently carbon. Since we focus on cathodes in this thesis and since stability to high voltage cathodes is a relatively new requirement, we concentrate mainly on this aspect in the present chapter.

It is known that the voltage at which lithium can be extracted from lithiated Mn, Co, Ni oxide materials exceeds + 4.0 V (Fig 1-3-2) and so a competitive electrolyte should possess a stable anodic window comparable to this voltage. Of the electrolytes

traditionally favoured in 3 V lithium cells, i.e. tetrahydrofuran (THF), 2-methyltetrahydrofuran (2-MeTHF) and propylene carbonate (PC) solvents [6-15], only PC is suitable for 4 V lithium batteries because of its high resistance against oxidation at high voltage. Because of the interest in 4 V cathodes there is now much research on alternatives to PC including alkyl carbonates and ether based electrolytes, e.g. ethylene carbonate (EC), dimethyl carbonate (DMC), diethyl carbonate (DEC), diethoxyethane (DEE), as well as their mixtures, such as PC+EC, EC+DMC and EC+DEE [4, 5, 16-22]. Mixed solvents also offer improvements in other physical and chemical properties such as conductivity and operating temperature[4].

The electrochemical stability of an electrolyte includes contributions from the solvent and salt. In order to study the electrochemical stability of organic solvents it is normal to add salts such as $LiClO_4$, KPF_6 or tetrabutylammonium perchlorate (TBAP) to overcome the high resistivity of the solvents. Unfortunately, these salts can often limit the extent of the electrochemical window due to metal deposition, reduction of the cation or oxidation of the anion. These reactions make it difficult to determine the electrochemical behaviour of the solvents alone. Microelectrode techniques can solve this problem. The use of microelectrodes minimise the effect of solution resistance (i.e. iR drop) in an electrochemical cell [23, 24] and hence permit electrochemical investigation of highly resistive media. This technique has recently been applied to the study of solvents in the absence of added salts [6, 7].

Traditionally [10-16], platinum has been used as the working electrode material in the study of electrolyte stability often in the belief that this is an inert source or sink of electrons. Of course all electrodes add some chemical specificity so that the problem of determining electrolyte stability will always depend to some extent on the electrode material. Metals other than platinum, e.g. stainless steel (SS) and aluminium, are employed as substrate materials (i.e. current collectors in lithium batteries, on which active electrode materials are mounted) because of cost, mechanical property and relative stability. The influence of these metal electrodes on electrolyte decomposition

must not be neglected [12, 25-28]. As an essential component of the cells, however, the role of metal current collectors on electrolyte stability window has not been given sufficient emphasis.

In this chapter, several Li^+ electrolyte solutions are investigated, studies include (1) determination of the electrochemical stability windows of solvents by means of Pt microelectrodes; (2) the anodic behaviour of electrolytes on Al and SS electrodes; and (3) the influence of lithium manganese oxide spinels on electrolyte decomposition. The ultimate purpose of these studies is to determine the potentials corresponding to anodic breakdown of these electrolyte solutions at composite electrodes containing lithium manganese oxide spinel mounted on SS or Al substrates, and hence to establish cut-off potentials for the cycling of cells.

4-2 Electrochemical stability windows of some solvents

The molecular formulae for PC, EC and DMC presented in Fig 4-2-1, the first two possess a five member ring. In this section the electrochemical stability of these solvents without addition of salt is explored using microelectrodes. The voltammetric experiments were run at a sweep rate of 200 $mV \cdot s^{-1}$ and at a 25 μm diameter Pt microelectrode in a two electrode cell. The two electrode cell consists of a Pt microelectrode and a Li electrode as described in CHAPTER THREE (Fig 3-4-3). Potentials were first scanned anodically and then reversed ending at -2 V versus Li^+ (1M)/Li. Fig 4-2-2 shows voltammograms for pure PC, EC, DMC and tetraglyme ($CH_3O(CH_2\text{-}CH_2O)_4\text{-}CH_3$) solvents. The voltammograms in Fig 4-2-3 correspond to mixtures of EC with PC and DMC in a 50 : 50 ratio by volume, respectively.

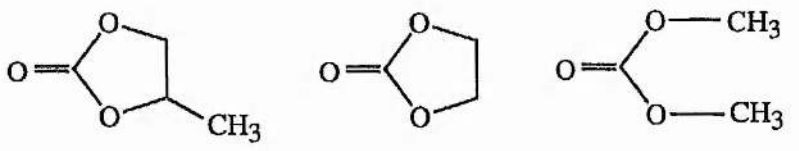

propylene carbonate ethylene carbonate dimethyl carbonate

Fig 4-2-1 Molecular formulae.

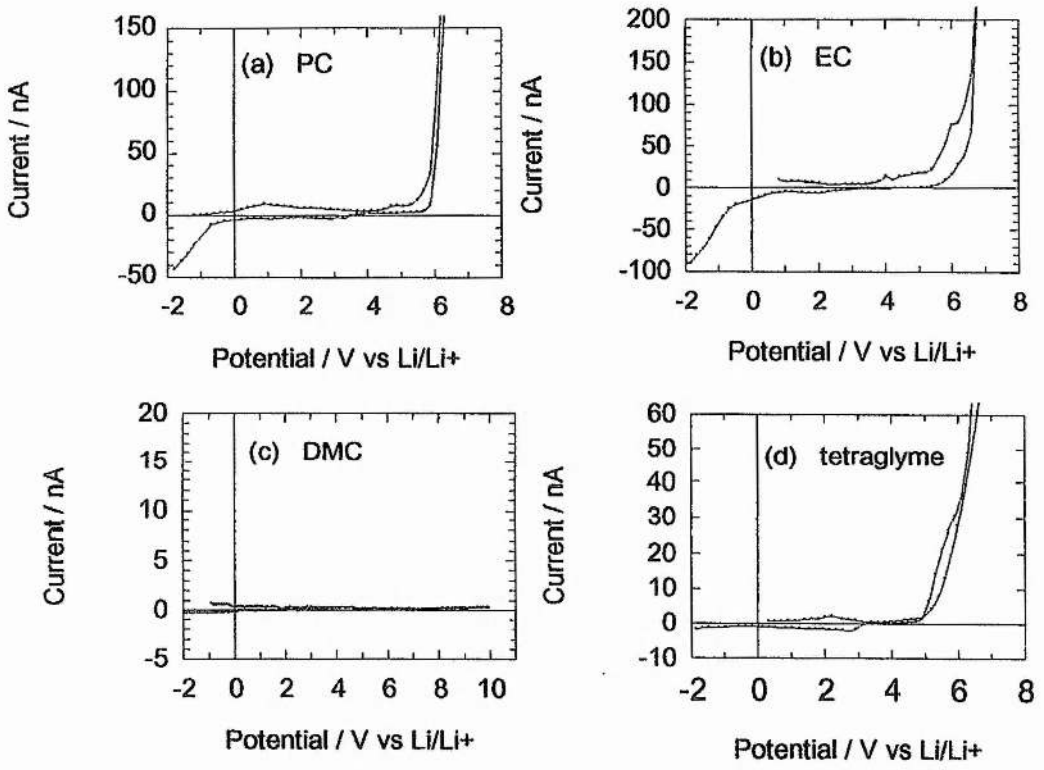

Fig 4-2-2 Cyclic voltammograms of (a) PC, (b) EC, (c) DMC and (d) tetraglyme solvents using a 25 μm diameter Pt microelectrode and at a scan rate of 200 $mV \cdot s^{-1}$.

4-2-1 Propylene carbonate

Propylene carbonate was first purified as described in CHAPTER THREE. As shown in Fig 4-2-2 (a), pure PC breaks down anodically at a potential of +5.6 V, and reduces apparently around –0.7 V. There is a very small cathodic current between +0.5 V and -0.7V. The cathodic behaviour at potentials positive of -0.7 V does not agree with that reported in references 6 and 15. According to the work of Campbell *et al.* [6], a cathodic current starts at around +1 V, and the current increases in magnitude and even shifts to more positive potentials on adding H_2O and / or 1,2-propanediol, common impurities even in distilled PC. The reduction of PC electrolytes at +1 V has been reported to yield propene and alkyl carbonate anions as the major products [15, 29, 30]. Jansta *et al.* [31] pointed out that this reducing current occurred only in the

presence of trace water (1-100 ppm). It therefore appears that the products of water reduction (OH^- and H^o_{ads}) are involved in the reduction of PC at +1 V [6, 11, 12]. In other words, the cathodic current starting at +1 V is an indication of the presence and quantity of water and impurities. We may conclude from our results that the PC used in this work is of a substantially higher purity than previously so-called pure PC. Evidently when sufficiently pure, PC possesses an electrochemical stability window in excess of 5.5 V and is relatively stable to oxidation beyond 5 V and reduction below 0 V vs. $Li/Li^+(1M)$.

4-2-2 Ethylene carbonate

Ethylene carbonate was purified as described in CHAPTER THREE. Cyclic voltammetric studies of EC, Fig 4-2-2 (b), were carried out at a temperature above its melt point (around 40 °C). This is the first investigation of EC using microelectrode technique. The anodic breakdown of EC occurs above +5 V, in this sense it is similar to PC. However, the cathodic current commenced at approximately +1.0 V and developed slowly until -0.5 V where upon the cathodic current increased rapidly. The onset and magnitude of the cathodic current indicates that EC is more susceptible to electroreduction than PC [32]. The reducing current at +1 V in EC is so small that it may be concluded that little water exists in the distilled EC. We may conclude that our purification procedure for EC is satisfactory. The electrochemical stability window for purified EC is similar to PC, i.e. around 5 V.

4-2-3 Dimethyl carbonate

Purification of dimethyl carbonate is described in CHAPTER THREE. This is the first microelectrode study of DMC. As is evident from Fig 4-2-2 (c), there is no evidence of electrochemical activity between +10 and -2 volts. It is difficult to believe that this or any other solvent would not be susceptible to oxidation and reduction at these

potentials, therefore another explanation must be sought for the apparent inactivity. One possibility is that the conductivity of the pure DMC is too low, even for a microelectrode, to permit sufficient passage of current for electrochemistry to take place. In order to answer this question, the conductivities of our pure PC, EC and DMC were measured using a high impedance Wayne KERR Autobalance Universal Bridge B641 connected to a commercial platinum black dipcell (ORION L/A = 1 cm-1). All measurements were carried out in an M Braun argon-filled glove box. Measurements on PC and DMC were carried out at room temperature whereas those for EC were carried out at a temperature of 40 °C, i.e. just above the melting point of this solvent. The results of these measurements are presented in Table 4-2-1 which clearly shows that the conductivities of the solvents measured at the temperatures used for the cyclic voltammetric experiments varies by an order of magnitude. In particular DMC possesses the lowest conductivity. However, although lower than PC by an order of magnitude, it seems unlikely that the conductivity of DMC could explain the lack of electrochemical activity. Instead, we are drawn to the view that a highly resistive layer may form on the working electrode during cycling which effectively inhibits any further electrochemical response. However, this must remain speculation until further evidence for the existence of such a layer can be obtained.

Table 4-2-1: Conductivities (~20 °C)

Solvents	Conductivity $\sigma \cdot cm^{-1}$
PC	7.1×10^{-7}
EC*	2.6×10^{-7}
DMC	4.7×10^{-8}

* measured at the point where solid EC transfers to liquid EC.

4-2-4 Tetraglyme

This solvent was purified as described in CHAPTER THREE. Fig 4-2-2 (d) shows anodic breakdown below 5 V, lower than the above carbonate solvents and hence this solvent is less favoured for use in 4 V lithium batteries.

4-2-5 Mixed solvents

As shown in Fig 4-2-3, the electroreduction of EC is inhibited somewhat by mixing with DMC or PC even taking into account the dilution by 50 %. Anodic stability of EC is improved to a minor extent by mixing with DMC. As can be seen, the use of mixed solvents improves not only ionic conductivity [4] but also electrochemical properties.

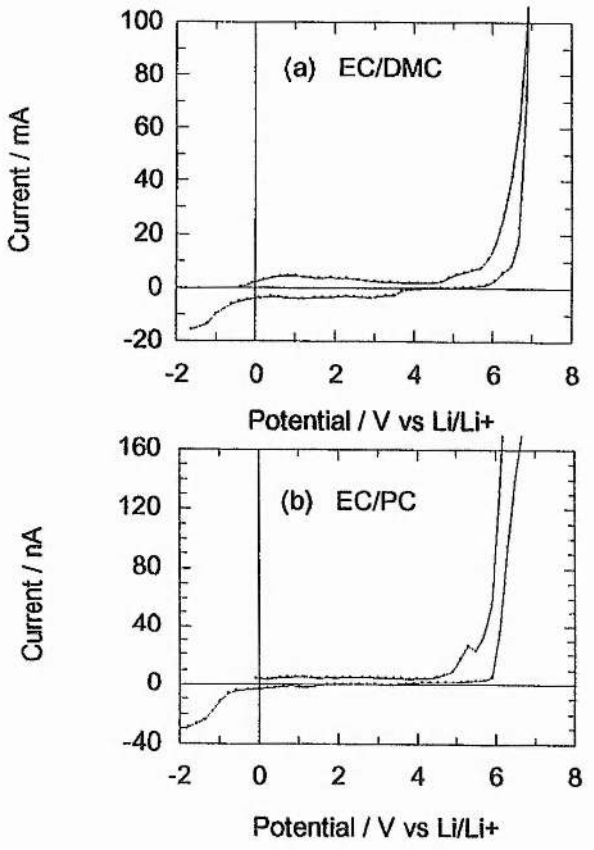

Fig 4-2-3 Cyclic voltammograms of mixed solvents: EC/PC and EC/DMC, at a 25 μm diameter Pt microelectrode and at a scan rate of 200 $mV \cdot s^{-1}$.

4-3 Anodic behaviours of Li^+ electrolytes at stainless steel and aluminium electrodes

Having looked at the stability of the pure solvents in the previous section we now turn to the stability of electrolytes themselves. It is known that when salts are added to the solvents the anodic stability of the resulting electrolytes may be reduced. However an aspect which has received much less attention is the influence of the substrate, on which the cathode material is mounted, on the electrochemical stability of various electrolytes. In lithium batteries various non-precious metals such as aluminium, stainless, copper, nickel, etc. have been used as substrates. No metal electrode is inert and therefore the concept of absolute electrochemical stability is at best an approximation. Different electrode materials can catalyse the decomposition of electrolytes. Here two electrolytes, PC and EC+DMC are considered along with four salts, $LiClO_4$, $LiAsF_6$, $LiPF_6$, and $LiCF_3SO_3$. The first three salts are usually considered to be stable up to at least 4 V whereas triflate salt is suitable for operation in 3 V batteries only. All experiments in the following were performed in a three electrode cell, as described in CHAPTER THREE (Fig 3-4-1), where the working electrode was stainless steel or aluminium metal.

4-3-1 $LiCF_3SO_3$, $LiClO_4$ and $LiAsF_6$ in PC solutions

The electrochemical stability of $LiClO_4$, $LiAsF_6$ and $LiCF_3SO_3$ in PC solutions have been studied using a Pt working electrode by numerous authors [11-25, 18]. However, the cyclic voltammograms (at 1 $mV \cdot s^{-1}$) of the three electrolyte solutions at stainless steel (denoted as SS) and aluminium electrodes (Fig 4-3-1) indicate that their anodic behaviour is related to the electrode material used.

$LiCF_3SO_3$ in PC is the decent example demonstrating the catalytic action of different electrode materials (Fig 4-3-1(a) and (d)). At Al electrodes, the anodic scan had to be

limited to +3.6 V to avoid a massive and irreversible anodic current occurring and once potential scanning exceeded the limit of 3.6 V in the first scan, the anodic current shifted negatively and increased in magnitude in subsequent cycles. In marked contrast, the potential can be safely scanned to +4 V at SS electrodes. It has been reported that oxidation of $CF_3SO_3^-$ commences with formation of $CF_3SO_3\cdot$ [33]. Once the radical is started, the reaction proceeds rapidly. It is possible that Al acts to aid radical formation although further studies would be necessary to probe this hypothesis..

The onset of the anodic oxidation for $LiClO_4$/PC and $LiAsF_6$/PC solutions are all beyond +4 V whether SS or Al electrodes are used, but the effect of the different metals on electrolyte oxidation is evident. At the Al electrode, $LiAsF_6$/PC is stable up to +5 V (Fig 4-3-1 (c)), whereas $LiClO_4$/PC oxidises at +4.2 V (Fig 4-3-1(b)). At the SS electrode, however, the situation is reversed: $LiClO_4$/PC is more stable than $LiAsF_6$/PC, Fig 4-3-1 (e) and Fig 4-3-1-(f). The relative instability of AsF_6^- based electrolytes at SS electrodes is due to the formation of soluble $Fe(AsF_6)_2$ whereas an insoluble layer is formed on the electrode in the case of ClO_4^- based electrolytes [25, 34]. This fact that SS electrodes are not stable in the presence of AsF_6^- is an excellent illustration of the importance role of the electrode material in controlling the electrolyte stability window.

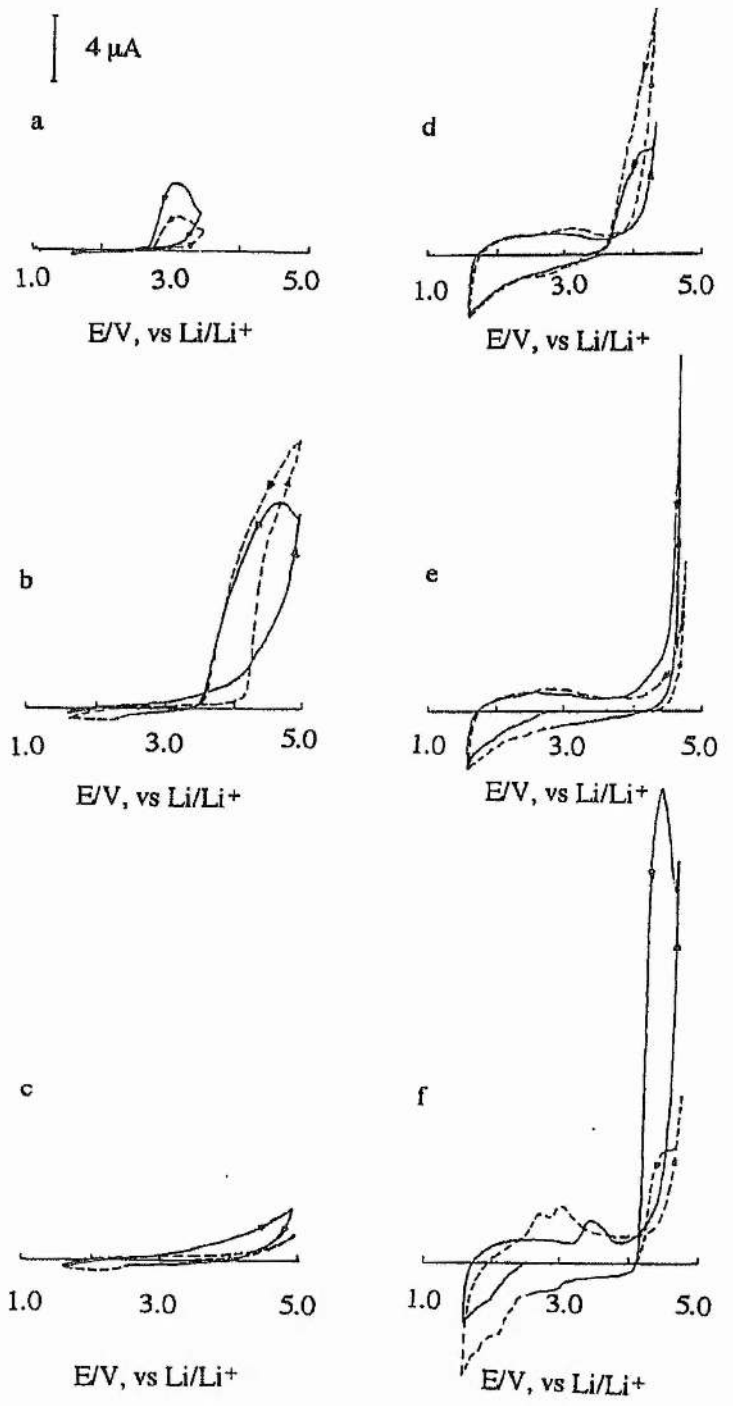

Fig. 4-3-1 Cyclic voltammograms for $LiCF_3SO_3$/PC (a, d), $LiClO_4$/PC (b, e) and $LiAsF_6$/PC (c, f) electrolyte solutions, respectively, at Al (a-c) and SS (d-f) electrodes (~ 1.1 cm^2) with a scan rate of 1 $mV \cdot s^{-1}$:
— the first cycle, ---- the second cycle.

4-3-2 $LiClO_4$, $LiAsF_6$, and $LiPF_6$ in EC + DMC solutions

A new electrolyte composition, $LiPF_6$ dissolved in mixture of EC and DMC, has recently been proposed and patented by Guyomard and Tarascon [4, 16]. This electrolyte is considered to be one of the best candidates for use in 4 V Li and Li-ion cells due to its stability against oxidation extending up to +5 V at 25 °C and +4.8 V at 55 °C [4, 16, 17, 35] as well as its other physical and chemical properties [4, 16]. In order to observe further the limitation of substrate metals on the anodic window of electrolytes, $LiAsF_6$/EC+DMC, $LiClO_4$/ EC+DMC and $LiPF_6$/EC+DMC solutions were studied in contact with SS and Al electrodes. EC and DMC solvents were mixed in a ratio of 50:50 by volume. Voltammetric experiments commenced by first scanning anodically from the open circuit potential to 5 V followed by cycling between 5 V and 4 V, or between 5 V and 3V at a scan rate of 10 $\mu V \cdot s^{-1}$.

Fig 4-3-2 presents the variation of anodic current with potential for the 1st, 2nd, or 3th cycles at an Al electrode. The $LiPF_6$ solution exhibited no anodic breakdown up to +5 V, consistent with the report by Guyomard and Tarascon. However, the solution of $LiAsF_6$/EC+DMC is also resistant to oxidation up to +5V. Only the solution containing $LiClO_4$ behaved somewhat differently; it produced a small but well-defined steeply rising at around 4.8 V in the 1st anodic scan and its oxidation current gradually increased in subsequent cycles. Clearly, the $LiClO_4$ based electrolyte is not stable at Al electrodes compared with fluorinated salts based electrolytes.

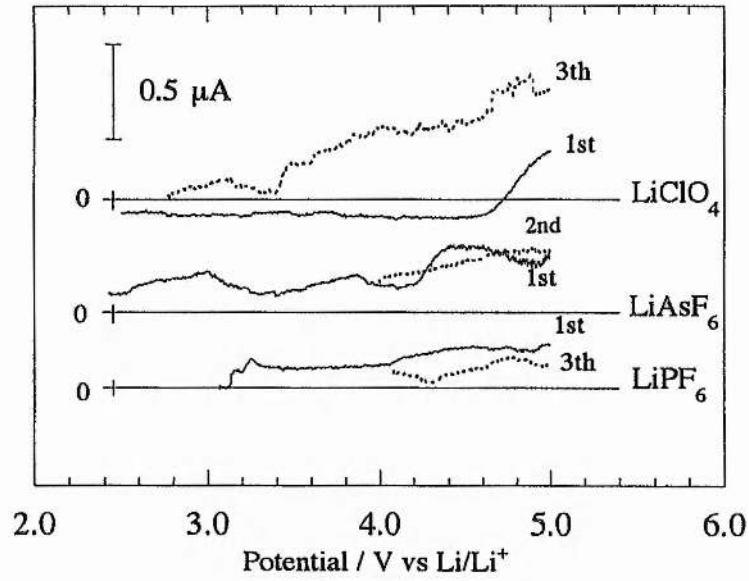

Fig 4-3-2 Curves of anodic current against potential for $LiPF_6$/EC+DMC, $LiAsF_6$/EC+DMC and $LiClO_4$/EC+DMC solutions at Al electrodes (~1.1 cm^2) with 10 $\mu V \cdot s^{-1}$ scan rate. The digits in the figure represent the cycle number.

The same electrolytes were studied at SS electrode under similar conditions. Fig 4-3-3 again indicates that the $LiAsF_6$ electrolyte is unsuitable for use with SS electrodes; at potentials beyond +4.5 V, the anodic current rose rapidly and oscillated violently. Furthermore, the anodic breakdown of the $LiAsF_6$ electrolyte shifted from +4.5 V in the first scan to +4.1 V in the second scan, possibly as the result of removal of a protective film on the SS surface. In contrast, $LiClO_4$ in EC+DMC solution proved to be very stable nearly to +5V. Comparing the $LiPF_6$ based electrolyte in contact with Al (Fig 4-3-2) and SS (Fig 4-3-3) anodic stability is somewhat reduced in contact with the latter electrode.

In summary the highest stability to oxidation is to be found with $LiPF_6$ in EC+DMC at a Al electrode. Other fluorinated salts are also stable in contact with Al. $LiClO_4$ based electrolytes are most stable at SS electrodes.

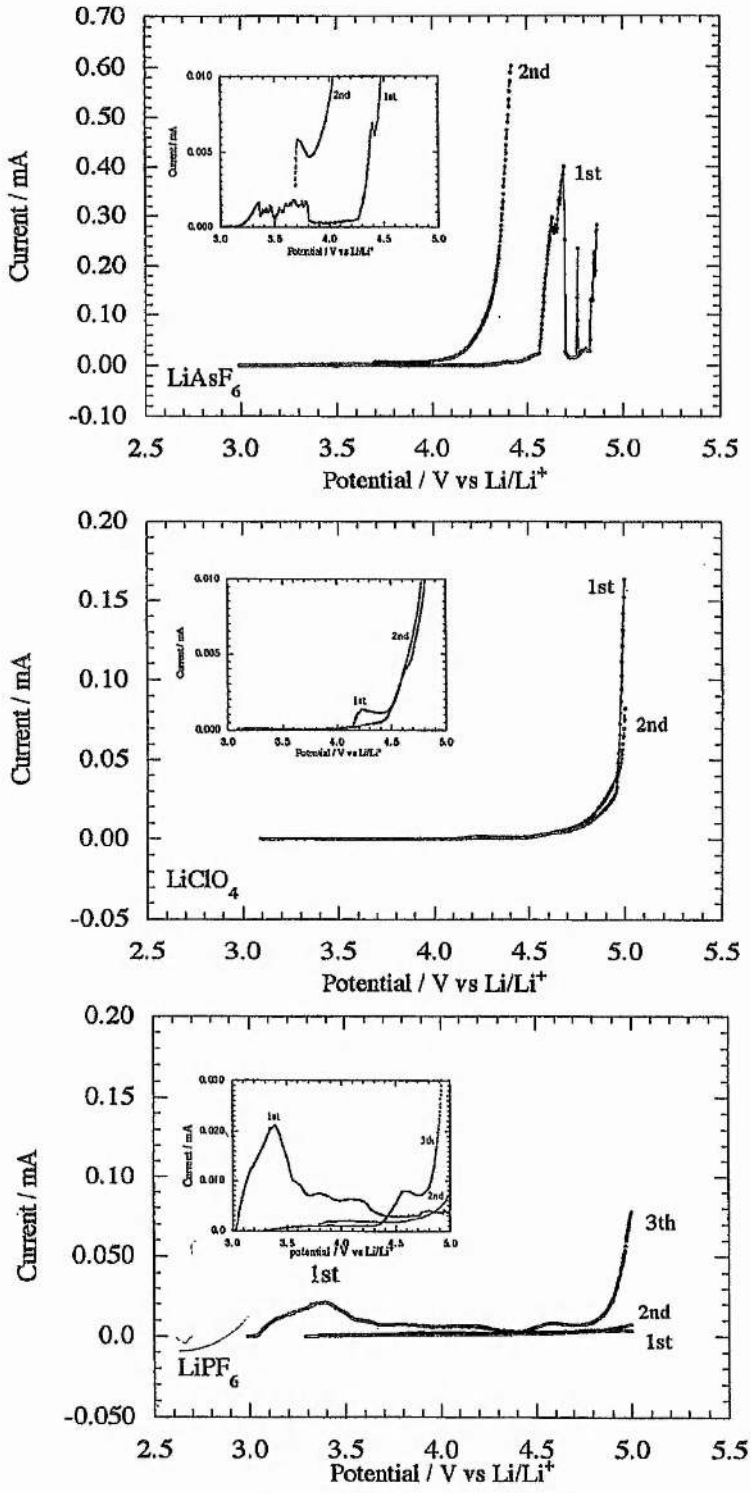

Fig 4-3-3 Anodic voltammetric curves for $LiAsF_6$/EC+DMC, $LiClO_4$/EC+DMC and $LiPF_6$/EC+DMC solutions at SS electrodes (~ 1.1 cm^2) with a scan rate of 10 $\mu V \cdot s^{-1}$). The digits in the figure represent cycle number.

4-4 Electroxidations of Li^+ electrolytes at composite electrodes containing lithium manganese oxide spinels

In order to examine the electrochemical oxidation of $LiClO_4$, $LiAsF_6$ and $LiPF_6$ electrolytes on the surface of lithium manganese oxide spinels, composite electrodes were fabricated by pressing a mixture of the spinel oxides with carbon black and PTFE onto metal substrate such as aluminium or stainless steel (see CHAPTER THREE for further details). The composite electrodes were used as working electrode in a three-electrode cell (Fig 3-4-1). In the experiments below, the working electrodes were first oxidised by a slow potential sweep (10 $\mu V \cdot s^{-1}$) from their open-circuit potentials to +4.4 V versus Li^+/Li. This ensured that the electrodes studied reached to a high degree of deintercalation, so that in the subsequent cycles between +4.2 V and +4.7 V or +5V (2.7 $\mu V \cdot s^{-1}$ or 10 $\mu V \cdot s^{-1}$), the resulting current could be considered to involve electrolyte oxidation only.

4-4-1 Limitations of metal substrates

Firstly, two working electrodes, differing only in that one was based on an Al substrate and the other a SS substrate, were tested in 1 M $LiClO_4$/PC and 1 M $LiAsF_6$/PC solutions, respectively. Fig 4-4-1 presents the cyclic voltammograms for the two types of composite electrode which contained the spinel prepared by solid state reaction, clearly showing the effect of metal substrate on the onset of anodic breakdown. $LiAsF_6$/PC is stable up to 5 V at Al substrate and $LiClO_4$/PC is stable to 4.92 V at SS substrate. This results agree with the behaviour of $LiAsF_6$ in EC/DMC at an Al electrode (Fig 4-3-2) and $LiClO_4$ in EC/DMC at a SS electrode (Fig 4-3-3), respectively, except for the magnitude of background current. The same $LiAsF_6$/PC electrolyte however breaks down at less than 4.5 V in the case of a SS substrate. Although the surface of the composite electrode is the main location for electrochemical reactions, electrolyte decomposition may take place on the metal

substrate/electrolyte interface due to only partial coverage of the substrate by the composite electrode or by liquid penetration through the porous composite electrode. The different results for $LiAsF_6$/PC oxidation at SS and Al substrates in Fig 4-4-1 indicates the importance of choosing an appropriate metal as the current collector in the construction of 4 V cells depending on the electrolyte used.

Note that there are a pair of small peaks at ~4.5 V in Fig 4-4-1. They are attributed to the reaction of the spinel itself and are discussed further in CHAPTER SIX.

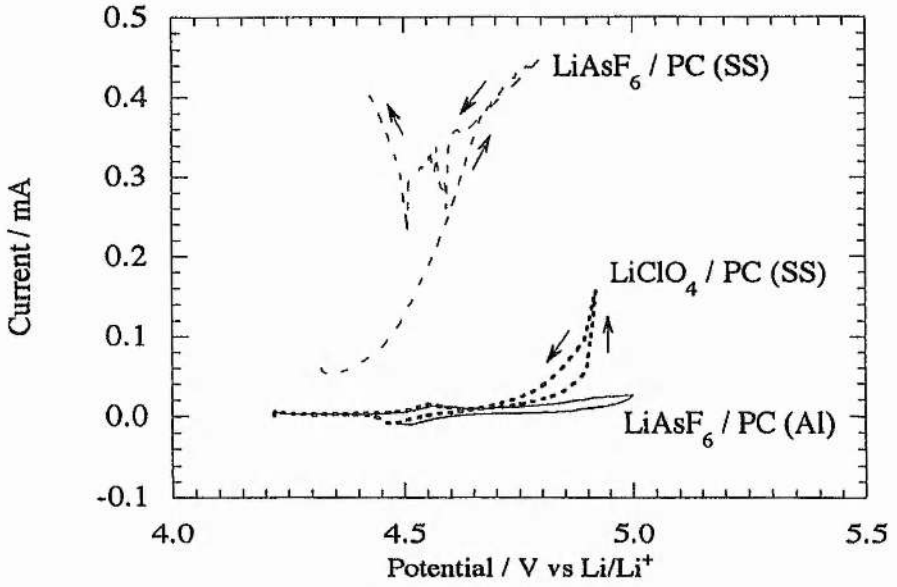

Fig 4-4-1 Cyclic voltammograms for $LiAsF_6$/PC and $LiClO_4$/PC electrolytes at the composite electrodes containing the spinel prepared by solid state reaction at 850 °C (2.7 $\mu V \cdot s^{-1}$, ~0.9 cm^{-2}). The SS and Al in brackets represent the metal substrates used on which composite electrodes were pressed.

4-4-2 Influence of different spinels

Various lithium manganese oxide spinels have been synthesised in this work to provide material optimised for operation in different voltage regions. The different spinels vary in composition, particle morphology and possibly in surface composition and structure. These differences may influence electrolyte decomposition. Two lithium manganese oxide spinels, prepared by the solution route (see CHAPTER FIVE

for further details) but fired at 200 °C and 600 °C, respectively, were tested in $LiClO_4$/PC electrolyte to examine the influence of the different spinels. Since $LiClO_4$/PC was used, the composite electrodes were prepared on stainless steel substrates. Fig 4-4-2 presents the oxidising currents in the first and second cycles against potential, showing that $LiClO_4$/PC oxidises more easily at the 200 °C spinel electrode than at the 600 °C spinel electrode despite similar particle sizes and hence surface areas (see CHAPTER FIVE).

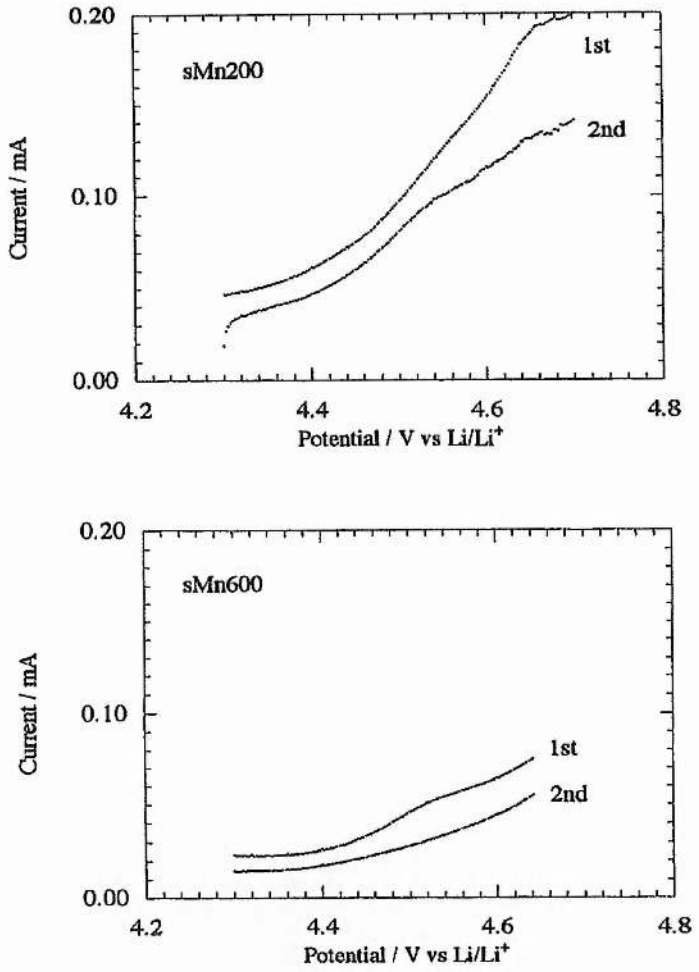

Fig 4-4-2 Curves of anodic current against potential for the 1 M $LiClO_4$/PC electrolyte at composite electrodes containing the spinels prepared by solution synthesis fired at 200 °C and 600 °C, respectively. The numbers in the figure present the cycle number. (scan rate: 10 $\mu V \cdot s^{-1}$, electrode area: ~ 0.9 cm^{-2}).

In contrast to the results in Fig 4-4-1, the spinels in Fig 4-4-2 have no redox peaks between 4.2 V and 4.7 V. This is again associated with the electrochemical behaviour of the spinels and will be discussed in the relevant section of CHAPTER SIX.

4-4-3 $LiPF_6$ and $LiAsF_6$ based electrolytes

Fluorinated salt based electrolytes, such as $LiAsF_6$/PC, $LiAsF_6$/PC+EC and $LiPF_6$/EC+DMC, were further studied on the 600 °C spinel which is a good 4 V cathode material. Composite electrodes were prepared on Al substrates. Fig 4-4-3 shows that all electrolytes have a similar anodic behaviour but differ somewhat in the magnitude of currents which reflect ease of electrolyte oxidation. Cyclic voltammetry is useful for the determination of the electrochemical stability window of electrolytes, but is not so well suitable to establish the rate of electrolyte decomposition. To answer this question time dependent experiments, such as chronoamperometry, are needed. In comparison with the magnitude of the current obtained with spinel electrodes when operated within their working range from 3.8 V to 4.2 V (see CHAPTER SIX) the current associated with electrolyte decomposition (Fig 4-4-3) are much smaller. However, at higher potential in particular above 4.7 V the current increases significantly. This rapidly increasing current may arise from the electrolytes themselves or the spinel. Corresponding to the latter possibility, Tarrescon et al [34] reported that there is further oxidation of spinel associated with an anodic current at 4.9 V vs. Li/Li^+. Our spinel however does not exhibit this, see Fig 6-3-2, indicating that the higher current above 4.7 V are associated with the electrolytes. The fact that cycling to 4,7 V is detrimental to the capacity retention (see CHAPTER SIX) further suggests that the high voltage oxidation is due to electrolyte decomposition. Thus the voltage limit for charging a spinel based composite electrode should be set at 4.7 V vs. Li/Li^+ despite the fact that these electrolytes containing fluorinated salts are stable up to 5V Li/Li^+ at an aluminium electrode.

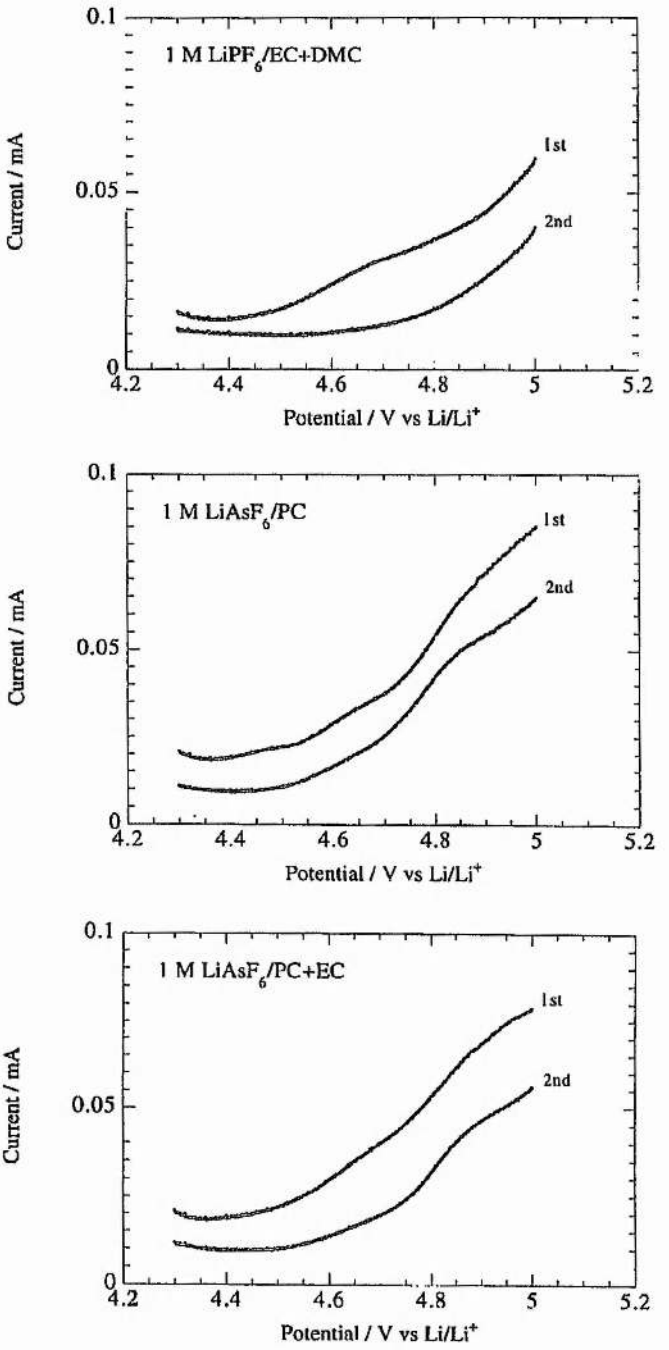

Fig 4-4-3 Electrochemical behaviours of $LiAsF_6$/PC, $LiAsF_6$/PC+EC, and $LiPF_6$/EC+DMC solutions on the composite electrode containing the spinel prepared by solution route and fired at 600 °C in the potential range from 4.2 V to 5 V. (sweep rate: 10 $\mu V \cdot s^{-1}$, electrode area: ~0.9 cm^{-2}).

4-5 Conclusions

Propylene carbonate, ethylene carbonate and dimethyl carbonate are very stable solvents for use in 4 V lithium batteries. Their anodic limits can be beyond 5.5 V vs. Li/Li^+. Of them dimethyl carbonate has the lowest anodic current up to high potential. Mixing this solvent with ethylene carbonate further improves the anodic stability. $LiClO_4$, $LiAsF_6$ and $LiPF_6$ all possess a high resistance to oxidation at high voltage and so are able to be used in 4 V lithium batteries. However, the metal current collector used in cells should be compatible to these salts. For example, use of a stainless steel substrate substantially reduces the anodic stability of $LiAsF_6$ based electrolytes, and $LiPF_6$/EC+DMC, which is a very stable electrolyte used for 4 V lithium batteries, must be used in conjunction with aluminium current collector. At room temperature, $LiClO_4$ based electrolytes can resist oxidation up to +4.9 V at stainless steel electrodes, while $LiPF_6$ and $LiAsF_6$ based electrolytes have an anodic stability up to +5 V on Al electrodes. Because $LiClO_4$ is unacceptable for battery applications due to reasons of safety, only the fluorinated salts such as $LiPF_6$ and $LiAsF_6$ can be chosen for 4 V lithium cells and hence we are limited to aluminium metal as the current collector. It is evident that at room temperature potentials below +4.7 V or 4.5 V are safe cut-offs for charging spinel cathodes in electrolytes such as $LiPF_6$/EC+DMC and $LiClO_4$/PC, respectively.

References

[1] K.Brandt, Solid State Ionics, **69** 173 (1994).

[2] R.Koksbang, I.I.Olsen, and D.Shackle, Solid State Ionics, **69** 320 (1994).

[3] M.Armand, Solid State Ionics, **69** 309 (1994).

[4] J.M.Tarascon, and D.Guyomard, Solid State Ionics, **69** 293 (1994).

[5] J.T.Dudley, D.P.Wilkinson, G.Thomas, R.Levae, S.Woo, H.Blom, C.Horvath, M.W.Juzkow, B.Denis, P.Juric, P.Aghakian, and J.R.Dahn, J. Power Sources, **35** 59 (1991).

[6] S.A.Campbell, C.Bowes, and R.S.McMillan, J. Electrochem. Soc., **284** 195 (1990).

[7] D.Baril, M.Gauthier, and A.Lasia, J. Electroanal. Chem., in press.

[8] K.M.Abraham and S.B.Brummer in J.PGabano (Ed.), Lithium Batteries, Academic Press, London, 371 (1983)

[9] J.B.Kerr, J. Electrochem. Soc., **132** 2839 (1985).

[10] Masayasu Arakawa and Jun-Ichi Yamaki, J. Electroanal. Chem., **219** 273 (1987).

[11] B.Rasch, E.Cattaneo, P.Novak, and W.Vielstich, Electrochimica Acta, **36** 1397 (1991).

[12] E.Cattaneo, B.Rasch, and W.Vielstich, J. Appl. Electrochem., **21** 885 (1991).

[13] F.Ossola, G.Pistoia, R.Seeber, and P.Ugo, Electrochimica. Acta, **33** 47 (1988).

[14] S.Tobishima, and T.Okada, Electrochimica. Acta, **30** 1715 (1985).

[15] G. Eggert, and J.Heitbaum, Electrochim. Acta, **31** 1443 (1986).

[16] D.Guyomard, and J.M.Tarascon, J. Electrochem. Soc., **140** 3071 (1993).

[17] D.Guyomard, and J.M.Tarascon, Extended Abstracts, 6th International Meeting on Lithium Batteries, 92.

[18] D.Guyomard, and J.M.Tarascon, J. Electrochem. Soc., **139** 937 (1992).

[19] M.Takahashi, S.Yoshimara, I.Nakane, T.Nohma, K.Nishio, T.Saito, M.Fujimoto, S.Narukawa, M.Hara, and N.Furukawa, J. Power Sources, **43-44** 253 (1993).

[20] H.Watanabe, T.Nohma, I.Nakane, S.Yoshimura, K.Nishio, and T.Saito, J. Power Sources, **43-44** 217 (1993).

[21] S.S.Prabhu, T.Prem Kumar, P.N.N.Namboodiri, R.Gangadharan, J. Appl. Electrochem., **23** 151 (1993).

[22] D.Aurbach, A.Zaban, Y.Gofer, Y.Ein Ely, I.Weissman, O.Chusid, and O.Abramzon, Extended Abstracts, 7th International Meeting on Lithium Batteries, 97 (1994).

[23] M.J.Pena, M.Fleischmann, and N.Garrard, J. Electroanal. Chem., **220** 31 (1987).

[24] B. R.Scharifker, Microelectrode Techniques in Electrochemistry, in Modern Aspects of Electrochemistry No. 22, Edited by J.O.M.Bockris et al., Plenum Press, (1992).

[25] D.A.Shifler, P.J.Moran, and J.Kruger, J. Electrochem. Soc., **139** 54 (1992).

[26] D.A.Shifler, P.J.Moran, and J.Kruger, Electrochimica Acta, **38** 881 (1993).

[27] F.W.Dampier, J. Electrochem. Soc., **126** 507 (1979).

[28] K.Kanamura, S.Tariyama, S.Shiraishi, and Z.Takehara, J. Electrochem. Soc., **142** 1383 (1995).

[29] D.Aurbach, and H.Gottlieb, Electrochimica Acta, **34** 141 (1989).

[30] D.Aurbach, J. Electrochem. Soc., **136** 906 (1989).

[31] J.Jansta, F.P.Dousek, and J.Riha, J. Electroanal. Chem., **44** 263 (1973).

[32] D.Aurbach, Y.Gofer, M.Ben-Zion, and P.Aped, J. Electroanal. Chem., 339 451 (1992).

[33] F.M.Gray, Solid Polymer Electrolytes: Fundamental Properties and Technological Applications, VCH Publishers, Inc., (1991).

[34] R.G.Kelly, P.J.Moran, and J.Kruger, J.Electrochem. Soc., **136** 3262 (1984).

[35] J.M.Tarascon, and D.Guyomard, Eelectrochimica Acta, **38** 1221 (1993).

CHAPTER FIVE

A New Solution Synthesis for Preparing Spinel Lithium Manganese Oxides
— Preparation and Characterisation

5-1 Introduction

The original $LiMn_2O_4$ compound was prepared, based on Wickham and Croft's work [1], by the high temperature solid-state reaction of Mn_2O_3 and Li_2CO_3 at 850 °C in air. The study of this compound as a cathode material for use of lithium batteries started in 1981 when Hunter first reported the preparation of a spinel-related manganese oxide, denoted as λ-MnO_2, by leaching lithium from $LiMn_2O_4$ with aqueous acid [2], and studied the electrochemical redox reversibility of this oxide [3]. Following this work, the structure relationship and electrochemistry associated with $LiMn_2O_4$ were studied by numerous authors in 1980's [4-10]. At that time, $LiMn_2O_4$ preparation was almost always based on the conventional solid-state method. However, it was found that when cycled on either the 3 V or 4 V plateau the practical capacity of this high-temperature material was low (e.g. < 80 $mAh \cdot g^{-1}$ for 4 volt Li cells) and declined markedly on cycling, although possessing a satisfactory theoretical specific capacity (148 $mAhg^{-1}$) and open circuit voltage. The materials obtained by solid state reaction were highly stoichiometric and possessed relatively large particles (typically averaging 10 μm in diameter [11]). The poor cycling performance could be related to these factors. It was realised that the solution to this problem was to develop low temperature routes capable of yielding small particle size. It turns out that these routes also optimise composition something that was not understood or reported at the time.

In the late 1980's, Nohma *et al.* first reported a solid-state reaction of MnO_2 and either LiOH, $LiNO_3$, or Li_2CO_3 at below 400 °C [12-16]. They denoted the product as CDMO (composite dimensional manganese oxides). This oxide is a 3 volt cathode material which can give a practical capacity of 200 $mAhg^{-1}$ when prepared at 250 °C [12]. CDMO is poorly crystalline. Nohma *et al.* considered CDMO as a composite structure of γ/β-MnO_2 and Li_2MnO_3 with included lithium [12, 14], while a different interpretation was offered by Thackeray *et al.* who suggested CDMO consisted of γ/β-MnO_2 and spinel [17, 18]. Based on this solid state reaction but with a different molar ratio of Li/Mn (3/8), Ohzuku *et al.* prepared an orthorhombic compound Li_xMnO_2 at 380 °C [19-21]. This oxide is also a 3 volt cathode material.

The formation of lithium manganese oxide spinel is, however, accessible via this route but requires an appropriate heating temperature [22, 23]. Using a moderate temperature, 450 °C, a spinel phase is obtained from the reaction of MnO_2 and Li_2CO_3 but with the presence of Mn_2O_3 as an impurity phase which only disappears at 800 °C [23]. Recently, Manev *et al.* [11, 24, 25] investigated intensively the conditions for this reaction with respect to the cathode performance for use in 4 V cells. They proposed that chemical MnO_2 and $LiNO_3$ are the optimum starting materials because chemical MnO_2 has a higher porosity and a greater mean pore radius than electrolytic MnO_2, and $LiNO_3$ melts at a significantly lower temperature (264 °C) than Li_2CO_3 (723 °C), and a reaction temperature in the range from 650 °C to 750 °C gives material with the best combination of capacity and cyclability. Similarly, Tarascon *et al.* [26] reported the effect of annealing temperature and cooling rate on the electrochemical performance. Their studies pointed out that a cubic spinel oxide is obtained from 800 °C annealing associated with slow cooling and the spinel produced performs well as a 4 volt cathode material. On other hand, preparing solid solution spinels $LiM_yMn_{2-y}O_4$ by replacement of some of manganese with another metal (e.g. Ti, Ni, Zn, Ge, Fe [27], Co [28], Mg [29], Cr [30, 31]) has also been done. The mixed metal spinels do give to some extent an improvement on cyclability but at the cost of capacity when cycling on the 4 V plateau [27, 30, 31]. Thackeray *et al.* [29, 32-34] discovered two new spinel related

phases $Li_2Mn_4O_9$ (a = 8.162 Å) and $Li_4Mn_5O_{12}$ (a = 8.137 Å) from solid-state reaction of $MnCO_3$ and Li_2CO_3 at 400 °C. However, these compounds belong to the class of 3 V cathode materials.

In summary of all the manganese oxides prepared by solid state reactions to date only the $LiMn_2O_4$ can be used as a 4 volt cathode in lithium batteries. It also of course can operate as a 3 V cathode. The preparation temperature of spinel phase $LiMn_2O_4$ material from solid state reaction may be lowered to 700 °C by using MnO_2 [11, 23-25] instead of Mn_2O_3 [2] as a starting material. Further reduction of the preparation temperature requires sol-gel techniques because such a synthesis encourages homogeneous mixing of the starting materials requiring less diffusion of ions at elevated temperature. Low temperature routes also have another advantage of reducing the particle size of the product. Based on a sol-gel route, Barboux *et al.* [35] synthesised $LiMn_2O_4$ at 300 °C using manganese acetate and LiOH as the starting compounds. This compound performed well as a 3 V cathode. A sol-gel route was also used to prepare a lameller manganese oxide [36], but this route is not very simple and the produced material only operates at 3 volt.

Compared with these literature methods, a new solution synthesis for preparing $LiMn_2O_4$ spinel is proposed. Depending on the conditions spinel optimised for 3 V or 4V performance may be prepared by this route. First the synthesis of 3 V material has the merits, (i) one can access a very low heating temperature, 200 °C, to prepare a single phase lithium manganese oxide with the spinel structure, (ii) the particle size of the products is small, (iii) the synthesis process is very simple and the aqueous solution reaction is able to be carried out in air compared with the sol-gel route in reference 35 in which an inert atmosphere is required, and (iv) as a result of (i) and (iii) the route is commercially attractive. This synthesis has been patented and published [37-39]. By raising the temperature to 600 °C after firing at 200 °C material optimised for 4 V operation can be prepared. We have found that the addition of carbon to the solution during preparation of 3 V and 4 V spinels has a significant beneficial effect on cycling at

3 V but no effect at 4 V. Similarly adding carbon to the sol-gel route of Barboux improves cyclability. We therefore report in this chapter synthesis with and without carbon showing how the resulting material compare in term of their structure and composition. The studies in this chapter also include chemical analysis, X-ray diffraction, and cyclic voltammetry etc. to characterise the solution based spinel products.

5-2 Spinel prepared by the sol-gel method

The following sol-gel method is based on that reported by Barboux *et al.* [35] but with the addition of carbon which enhances the capacity retention on cycling. The preparation procedure was as follows:

A small amount of carbon was first added to 100 ml of a solution of 0.8 M manganese acetate in water. This solution was stirred continuously while argon was bubbled through the solution. Sequentially, 40 ml of an aqueous solution which was 1 molar in LiOH and 3 molar in NH_4OH was added to the manganese acetate solution with vigorous stirring while maintaining an argon atmosphere. The use of ammonia was to supply more OH^- anions to ensure all manganese cations formed $Mn(OH)_2$. Because the oxidation of $Mn(OH)_2$ to Mn(III) takes place easily in air, the sol-gel reaction requires an inert atmosphere. A gelatinous precipitate was rapidly obtained once the two solutions were mixed. After stirring for about half a hour, the water was removed from the gelatinous slurry using a rotary evaporator at 85 ^oC, resulting in the formation of a xerogel. The xerogel was packed in a 25 ml alumina crucible and heated in air at 300 ^oC for 48 hour to obtain the final product. Another similar preparation but without the addition of carbon was also performed. The resulting powders were analysed by X-ray diffraction (Fig 5-2-1) and the powder patterns for materials with and without carbon were very similar, both were consistent with a spinel phase [2].

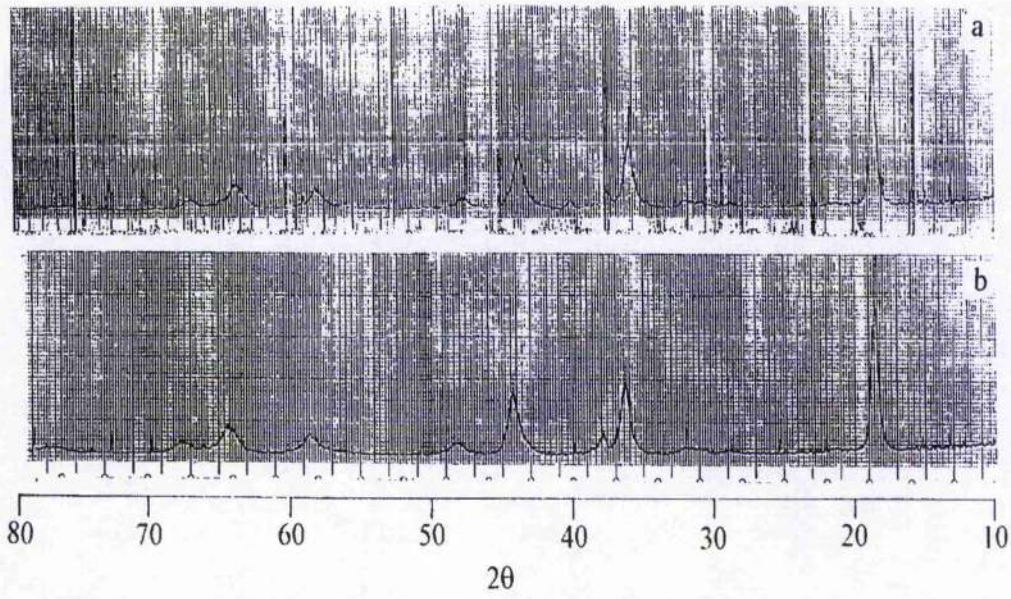

Fig 5-2-1 X-ray powder diffraction patterns for sol-gel products heated at 300 °C (a) without and (b) with carbon.

5-3 Spinel prepared by the solution method

5-3-1 Synthetic procedure

Starting materials were manganese acetate and lithium carbonate. They were mixed in distilled water with stirring. Sufficient manganese (II) acetate was used to yield a 2:1 mole ratio of manganese to lithium, for example, 8 g of $Mn(CH_3CO_2)_2{\cdot}4H_2O$ reacts with 0.603 g of Li_2CO_3 in 30-40 ml of water. A precipitate formed and was then separated from the remaining water by rotary vacuum evaporation at 85 °C. Finally, the solid obtained from the rotary evaporation was heated in air at 200 °C for 96 hours. In order to study the influence of carbon on the properties of the product, some solution reactions were carried out exactly as described above but with the addition of carbon, that is, a small amount of carbon (0.75 % by weight of $Mn(CH_3CO_2)_2{\cdot}4H_2O$) was introduced into the Mn (II) solution before being mixed with Li_2CO_3. Furthermore, various firing temperatures, specifically 300, 500, 600, 700, 850 °C were employed to prepare the spinel. In most cases, a two step heating procedure was applied, for

example, the solid product of rotary evaporation was first fired at 200 °C for a period and then fired at 600 °C. For convenience, sMn and scMn are used to denote the spinel prepared by the solution route without and with carbon, respectively. Firing temperatures are added to these symbols, e.g. a solution preparation with carbon and fired at 600 °C is denoted scMn600.

The resulting powders were analysed by X-ray diffraction. Fig 5-3-1 presents the XRD patterns for sMn200, scMn200, sMn600 as well as ssMn850 (the spinel which is prepared by conventional high temperature solid state reaction between Li_2CO_3 and Mn_2O_3 at 850 °C) for comparison. The powder patterns for materials fired at 200 °C with and without carbon are very similar. Both exhibit broader peaks than those in Fig 5-2-1. Despite the extremely low reaction temperature of 200 °C, there is no evidence of any additional peaks in the X-ray patterns arising from phases other than the spinel. The powder pattern of sMn600 is the same as those for sMn200 and scMn200 except that the peak widths are much reduced. The peaks are slightly broader in the case of sMn600 compared with the ssMn spinel indicative of a somewhat smaller average particle size. Samples fired at other temperatures, e.g. sMn500, sMn700 and sMn850, also show a single phase spinel.

In contrast to the sol-gel method [35] that involves the use of LiOH and NH_4OH, the solution reaction is able to operate in air due to the fact that $Mn(OH)_2$ is not produced in the solution that contains acetate and carbonate anions. Consequently, this solution route has an advantage over the sol-gel route because of its simplicity.

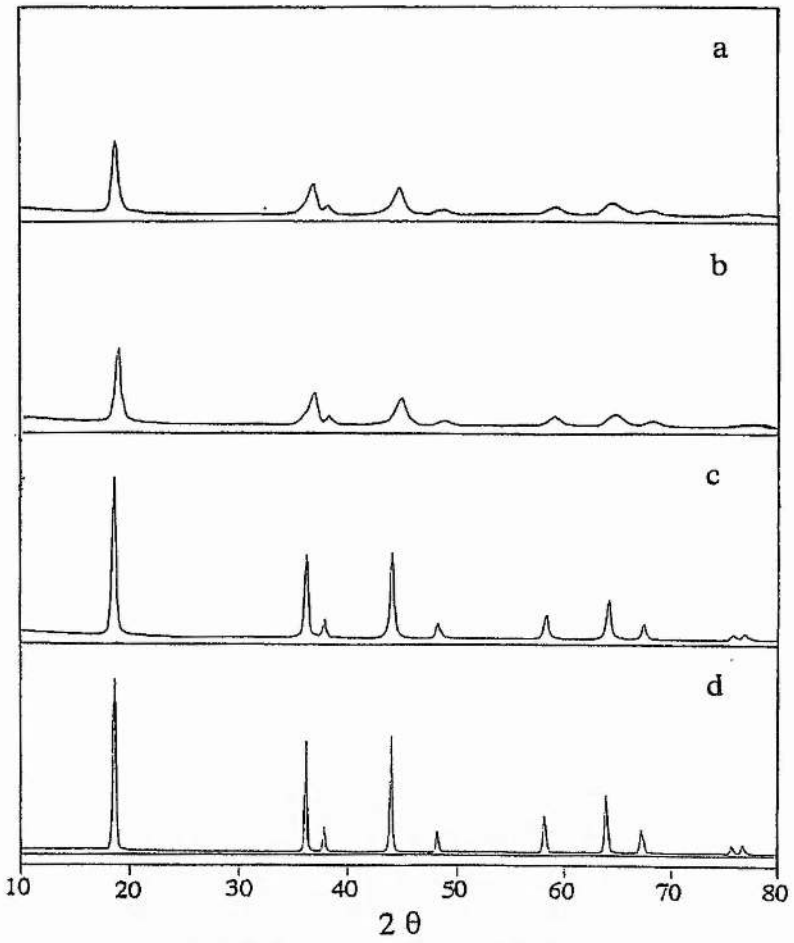

Fig 5-3-1 X-ray powder diffraction patterns for spinel lithium manganese oxides prepared from the solution synthesis, respectively, fired at 200 °C (a); 200 °C, but with carbon (b); 600 °C (c); and the spinel from conventional solid-state reaction, fired at 850 °C (d).

5-3-2 Mechanism of spinel formation

5-3-2-1 A study by X-ray diffraction

From X-ray diffraction patterns, the success of preparing the lithium manganese oxide spinel by the solution synthesis has been demonstrated. The following focuses on the changes which occur in the powder during formation of the spinel phase from this solution route as discovered by X-ray diffraction. Fig 5-3-2 carried out at different stages of the heating process. The pattern of the solid immediately after rotary

evaporation at 85 °C possesses a few broad peaks (Fig 5-3-2 (a)). Although the quality of the data is limited at this stage of heating, the peak at 10° in 2θ may be attributed to manganese acetate. The remaining two peaks at 24.6° and 31.4° correspond to the most intense peaks for $MnCO_3$ (seen Appendix I). After only a few hours heating at 200 °C, the XRD pattern changes significantly (Fig 5-3-2 (b)), for example, the peak at around 10° in 2θ present in Fig 5-3-2 (a) is now much sharper. The powder pattern is in fact similar to that obtained for manganese acetate alone after heating at 200 °C [40]. It is very interesting to observe an intermediate appearing during heating (Fig 5-3-2 (c)). For convenience, the peak positions in Fig 5-3-2 (c) are listed in Table 5-3-1 to compare with the XRD peaks of γ-Mn_2O_3 and $LiMn_2O_4$. As can be seen, the pattern of Fig 5-3-2 (c) is a result of overlap between the γ-Mn_2O_3 phase and that of spinel. Heating at 200 °C for 96 hours yields the final product i.e. a single phase spinel (Fig 5-3-2 (d)). Under the same heating conditions, a single phase spinel can not be formed from a mechanical mixture of solid manganese acetate and lithium carbonate, highlighting the key role of the solution step.

Table 5-3-1: XRD peak positions (in 2θ).

Fig 5-4-3c	18.3	29.2	31.1	32.7	36.3	38.5	44.6	51.3	54.3	56.2	58.8	60.5
γ-Mn_2O_3*	18.02 (70)	28.97 (90)	31.03 (20)	32.41 (90)	36.04 (100)	38.10 (30)	44.37 (60)	50.98 (30)	53.89 (20)	56.03 (10)	58.76 (30)	60.02 (80)
$LiMn_2O_4$**	18.65				36.15	37.85	44.00	48.12		58.10	63.88	67.13

* see Appendix I. Note that the values in bracket are relative intensities of diffraction peaks.

** based on the sample from solid-state reaction at 850 °C (see Fig 5-3-1d).

The effect of firing the solid obtained from rotary evaporation at 200 °C in argon has been investigated. No spinel phase was observed unless the atmosphere was switching to air. The product obtained in argon has a XRD pattern similar to Fig 5-3-2 (b) and this pattern remained unchanged within 96 h period of the experiment. From this, it may be concluded that in the early stage of heating at 200 °C, the solution based precursor (i.e.

the solid obtained from rotary evaporation) decomposes without oxidation, but subsequently the presence of oxygen is necessary to convert Mn^{2+} to higher average oxidation state of the spinel product. Therefore, we may propose a reaction mechanism for formation of spinel in air,

$$\text{solution based precursor} \xrightarrow{200^{o}C} \text{a decomposed product} + O_2$$

$$\xrightarrow{200^{o}C} \gamma\text{-}Mn_2O_3 \text{ phase} + O_2$$

$$\xrightarrow{200^{o}C} \text{spinel product.}$$

It has been reported that Mn_2O_3 reacts with lithium compounds to form $LiMn_2O_4$ spinel at a temperature higher than 700 °C [24]. It has been also pointed out that Mn_2O_3 exists as an impurity phase when MnO_2 reacts with Li_2CO_3 [23]. All these reports indicate that Mn_2O_3 only reacts at high temperature significantly above 200 °C. However, we note that the Mn_2O_3 material used as staring materials or formed as an impurity is the α-form, see Appendix I. In fact, it is known that γ-Mn_2O_3 is not stable and transfers spontaneously to α-Mn_2O_3 at room temperature [41]. Therefore, it is not inconsistent that lithium manganese oxide spinel forms at a low temperature by reaction with γ-Mn_2O_3.

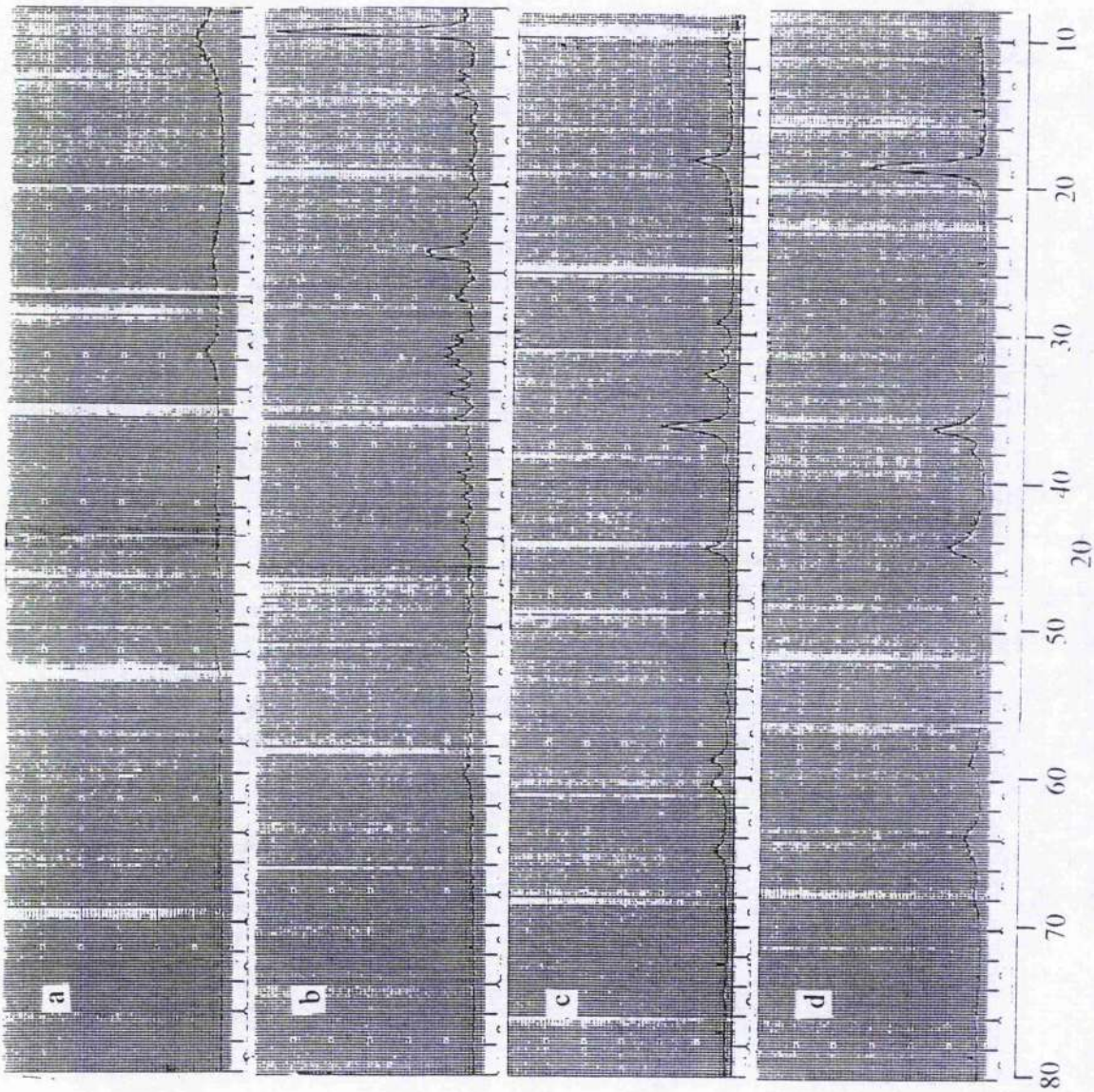

Fig 5-3-2 XRD patterns for the samples prepared by the solution synthesis and fired at air for (a) 0 hour, (b) 4 hours, (c) 48 hours, and (d) 96 hours.

5-3-2-2 A study by FTIR

Based on the stoichiometry of the reactants, 1 Li_2CO_3 to 4 $Mn(CH_3CO_2)_2$, it is clear that there is insufficient CO_3^{2-} to react with all the $Mn(CH_3CO_2)_2$. We may expect therefore that some $Mn(CH_3CO_2)_2$ remains along with $LiCH_3CO_2$. The XRD analysis revealed the presence of $MnCO_3$ and $Mn(CH_3CO_2)_2$ after rotary evaporation at 85 °C but no evidence for the other constituents presumably because of the weak scatting of lithium. Fourier Transfer Infrared spectroscopy (FTIR) was employed to investigate further the species present in the solid products of rotary evaporation. Fig 5-3-3 presents the FTIR spectra for the solid products from solution reaction with and without carbon. The FITR spectrum for the solid mixture of $Mn(CH_3CO_2)_2{\cdot}4H_2O$ and Li_2CO_3 is also included in Fig 5-3-3. As a result of the considerable similarity between the FTIR spectra for solid $LiOH{\cdot}H_2O$, $LiCH_3CO_2$, Li_2CO_3, $MnCO_3$ and $Mn(CH_3CO_2)_2{\cdot}4H_2O$ (see Appendix II), it is very difficult to identify the different chemical components of the solution-based precursor prior to firing at 200 °C. But, by comparing Fig 5-3-3 (a) with Fig 5-3-3 (c), the latter corresponding to the 4:1 mixture of $Mn(CH_3CO_2)_2$ and Li_2CO_3, it is possible to draw some conclusions. Fig 5-3-3 (c) exhibits two peaks arising from Li_2CO_3, marked with full circles, while these are absent in Fig 5-3-3 (a). The peak close at 720 cm^{-1} in Fig 5-3-3 (a), marked with full triangle, is not due to Li_2CO_3 but is associated with $MnCO_3$ (see Appendix II). Fig 5-3-3 (c) is similar to Li_2CO_3 in the range 500-400 cm^{-1}, whereas this is not the case for Fig 5-3-3 (a). Although no Li_2CO_3 remains after rotary evaporation it is not possible to unambiguously identify other lithium components from the IR results. Comparison of the IR spectra for materials prepared without and with carbon, i.e. Fig 5-3-3 (a) and Fig 5-3-3 (b) respectively, indicate that the addition of carbon does not change the chemical components in the product.

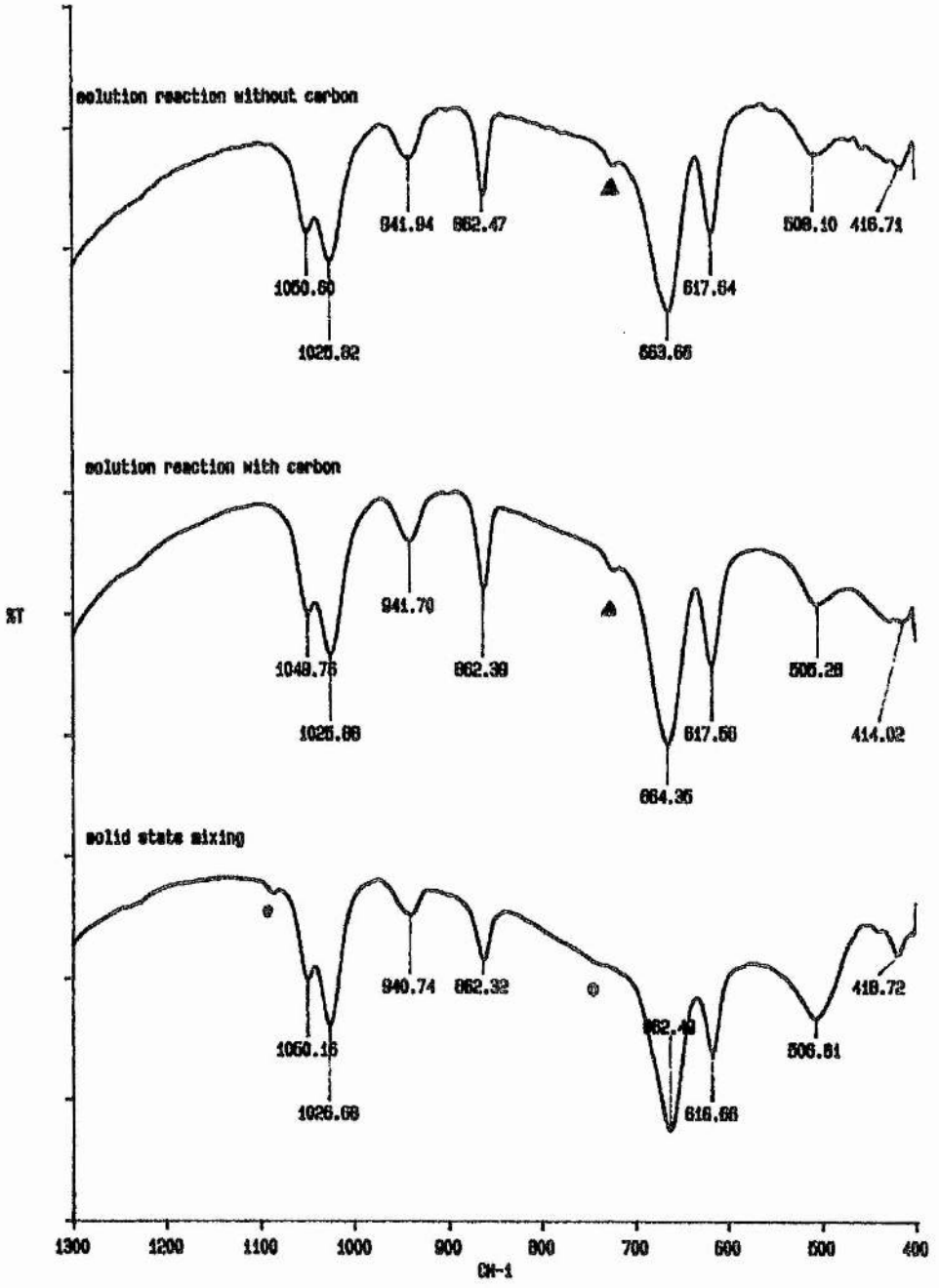

Fig 5-3-3 FTIR spectra for (a) the product of rotary evaporation from the solution reaction, (b) the product of rotary evaporation from the solution reaction but with carbon, (c) the mixture of manganese acetate and lithium carbonate. The filled circles correspond to peaks of Li_2CO_3 and the full triangle to $MnCO_3$.

5-4 Characterisation of the spinels prepared by the solution method

In order to characterise the physical and chemical properties of the solution based spinels, various experimental techniques including X-ray diffraction, potentiometric titration, transmission electron microscopy (TEM), and cyclic voltammetry have been used and described below.

5-4-1 Lattice parameter

In **5-3-1**, X-ray diffraction results have demonstrated that all oxide products from the solution route possess a spinel phase even at a heating temperature as low as 200 °C but the peaks broaden as the heating temperature decreases. Although broad peaks preclude an accurate determination of peak positions, lattice parameters for the solution based spinels prepared without or with carbon and fired at different temperatures are estimated by averaging the values obtained from the equation [43]

$$a = \frac{\lambda}{2 \times \sin(\theta)} \sqrt{h^2 + k^2 + l^2}\,.$$

Table 5-4-1 presents the values of the lattice parameters for the solution based spinels prepared at 200 °C, 300 °C, 600 °C and 850 °C without and with carbon, respectively denoted as sMn200, scMn200, sMn300, sMn600, and sMn850. The lattice parameter of the spinel prepared by solid-state reaction at 850 °C (ssMn850) is also calculated from the X-ray pattern. It is obvious that the lattice parameter of the cubic spinel decreases as the heating temperature is lowered, consistent with work in the literature [23, 26, 42]. However, because we have employed a lower firing temperature (200 °C) than has been reported previously then we observe the lowest ever lattice parameter for lithium manganese oxide spinel, 8.17 Å.

Table 5-4-1: The lattice parameters for various products from the solution synthesis (calculated on average from the (111), (311), (222), (400), (331) diffraction peaks).

samples	sMn200	scMn200	sMn300	sMn600	sMn850	ssMn850
a (Å)	8.17	8.17	8.17	8.21	8.23	8.24

5-4-2 Particle sizes

The particle size of battery electrode materials is an important parameter influencing performance. In order to investigate the particle sizes of our materials, transmission electron micrographs (TEM) was obtained. Fig 5-4-1 is the micrograph of the sample prepared by solution synthesis and fired at 200 °C (sMn200), it shows small particles 200-600 Å in size. It is interesting to find that the particle size of the sample fired at 600 °C is similar. This may be a result of the fact that this material was heated at 200 °C prior to final calcination at 600 °C, thus locking in a small particle size.

Fig 5-4-1 The micrograph of the spinel prepared from solution synthesis and fired at 200 °C by TEM.

5-4-3 Defect spinel

As shown in Fig 5-3-1, the low temperature spinels exhibit very broad X-ray diffraction peaks. In general, the width of a diffraction peak depends on the dimension of the regular crystalline array, so that the particle size of powder can be estimated from the widths of X-ray diffraction peaks according to the Scherrer formula [43]:

$$t = \frac{0.9 \times \lambda}{B \times \cos(\theta_B)}$$

where t is the thickness of the crystal (in angstroms), λ the x-ray wavelength (1.5405 Å) and θ_B the Bragg angle. The line broadening, B, is measured from the extra peak width at half the peak height compared with the peak width due to instrumental effects and is obtained from the Warren formula :

$$B^2 = B_m^2 - B_s^2$$

where B_m is the measured peak width in radians at half peak height and B_s is the corresponding width of a peak of a standard material, mixed with the sample, with a particle size sufficiently large to produce minimal peak broadening. The standard material should possess a particle size of greater than 2000 Å and its diffraction peaks must be close to the relevant peak of the sample under study.

It is important to remember that the particle size so determined is not necessarily the size of a grain. There may be many small added regions within one grain. Factors other than particle size may contribute to peaks broadening when the crystal is not perfect, such as strain in the lattice. In this situation, the Scherrer formula will not yield the correct result. To examine this, several spinel samples were mixed, respectively, with an appropriate amount of KCl powder and then X-rayed. Fig 5-4-2 shows an X-ray diffraction pattern for the sMn200 sample containing KCl; two peaks arise from the spinel at 36.45° and 37.90° in 2θ, respectively, with corresponding Miller indices of 311 and 222, and a narrow peak at 40.66° from KCl. Since the 222 peak is not well

defined in some samples, the 311 peak was chosen to calculate the particle size from the Scherrer formula. Similar measurements were performed for other spinels sample, see Table 5-4-2. Taking the case of sMn200 as an example, one can see that a particle size of less than 100 Å is estimated from the peak width, much smaller than the particle size estimated from TEM, Fig 5-4-1. By contrast, the result for sMn600 is similar to the values obtained from TEM. This suggests that the peaks broadening is not completely attributable to the small dimensions of coherent scattering blocks.

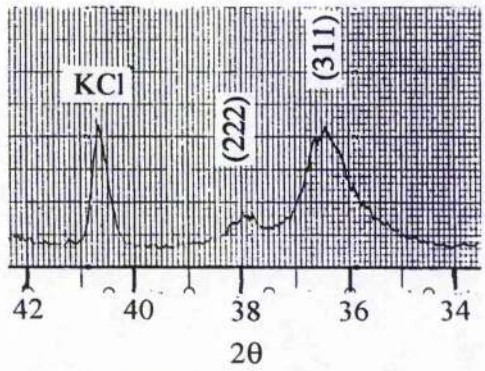

Fig 5-4-2 Powder X-ray diffraction for the mixture of the spinel prepared by solution synthesis and fired at 200 °C (sMn200) and KCl.

Table 5-4-2: Based on the 311 peak, the particle sizes for various spinel samples is calculated from Scherrer formula.

samples	sMn200	scMn200	sMn300	sMn600
t (Å)	93	91	128	283

It is noticeable that in the cases of the low-temperature samples the widths of the Bragg peaks increase significantly with increasing scattering angle. This suggests the presence of residual strain in the spinel [35, 44]. When peak broadening is influenced significantly by strain then a linear relationship between $B(2\theta)x\cos^2(\theta)$ and $\sin^2(\theta)$ for X-ray diffraction data should be observed, where $B(2\theta)$ is the width of the Bragg peak at half of its maximum intensity. In these circumstances the intercept with the origin

gives the structural coherence length (particle-size) and the slope provides the residual strain [35, 45]. Fig 5-4-3 presents the plots for several solution based spinels fired at different temperatures, sMn200, scMn200, sMn300, sMn500, sMn600 and sMn850, as well as ssMn850 prepared by solid state reaction at 850 °C.

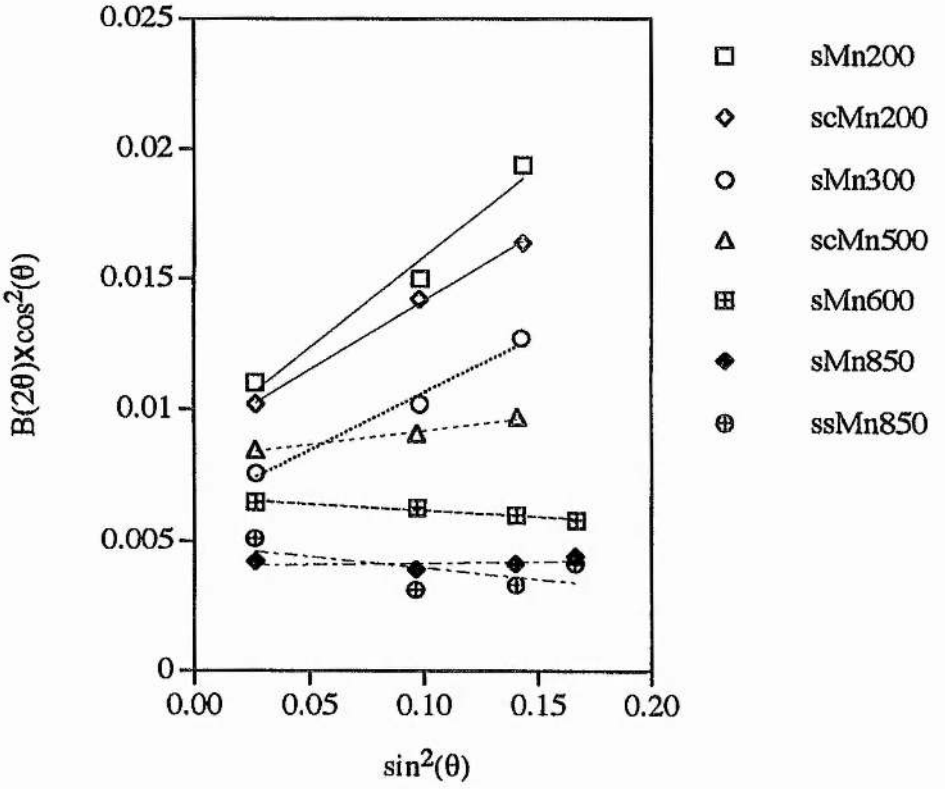

Fig 5-4-3 Plots of $B(2\theta)\cos^2(\theta)$ vs. $\sin^2(\theta)$ for the spinel oxides.

These plots are all linear, except for the case of ssMn850, but their slopes decrease with increasing firing temperature. The 200 °C and 300 °C samples produce the highest slope indicative of high residual strain, while the samples fired at or above 600 °C give a flat straight line, i.e. less residual strain. Although the intercept with the origin also depends on firing temperature, the significant change in slope indicates that XRD peak broadening, particularly in the low temperature spinels, is largely attributed to residual strain. The residual strain may arise from defects, e.g. cationic or anionic vacancies, or composition at inhomogeneities, or polymorphism [35, 44]. It is therefore reasonable

that the particle size calculated from the width of X-ray diffraction peaks is much smaller than that observed in the TEM result for sMn200.

5-4-4 Spinel composition

From the discussions in **5-4-2** and **5-4-3**, it is evident that the spinels obtained from the solution synthesis, particularly these fired at lower temperature (e.g. 200 °C), are imperfect. Chemical analysis in this section will indicate that these defect spinels deviate from the ideal $LiMn_2O_4$ composition.

The absence of any peak in the X-ray diffraction pattern other than these associated with the spinel coupled with the fact that the ratio of the Li to Mn in the starting materials was 1:2 and the firing temperature was not higher than 600 °C (i.e. there should be no significant loss of Li_2O) leads to the conclusion that the Li:Mn ratio in the product is also 1:2. This leaves the only undetermined aspect of the composition that of the oxygen content. Such a variation would of course imply a Mn oxidation state different from +3.5 valency. In order to determine the oxidation state of the lithium manganese oxide spinels, a chemical analysis based on a sequence of redox titrations involving the MnO_4^- / Mn^{2+} , Mn^{3+}/Mn^{2+}, and Fe^{3+} / Fe^{2+} couples [46] was used. This procedure is as follows:

(1) dissolution of lithium manganese oxide spinel in a solution of $FeSO_4$ in sulphate acid by reduction to Mn^{+2} ions:

$$LiMn_2O_{4+x} + (8+2x)H^+ + (3+2x)Fe^{2+} \longrightarrow$$

$$2Mn^{2+} + (3+2x)Fe^{3+} + (4+x)H_2O + Li^+ \qquad \{1\}$$

(2) potentiometric titration with a $KMnO_4$ solution to oxidise the excess Fe (II) ions which remains after the spinel dissolution:

$$MnO_4^- + 8H^+ + 5Fe^{2+} \longrightarrow Mn^{2+} + 5Fe^{3+} + 4H_2O \qquad \{2\}$$

(3) a second potentiometric titration with the same $KMnO_4$ solution but in the presence of an excess of $Na_4P_2O_7$ and at pH 6-7. Mn^{2+} ions generated in the first two steps react with the $KMnO_4$ and oxidise to Mn^{3+} in the presence of $H_2P_2O_7^{2-}$ and at pH 6-7:

$$4Mn^{2+} + MnO_4^- + 8H^+ + 15H_2P_2O_7^{2-} \xrightarrow{pH6-7} 5[Mn(H_2P_2O_7)_3]^{3-} + 4H_2O \qquad \{3\}$$

According to the three reactions, the x value in $LiMn_2O_{4+x}$ can be calculated from equation.{4} without the necessity to know the exact mass of solid oxide nor the exact molarity of the titrating $KMnO_4$ solution.

$$x = \frac{1}{2} \times [\frac{10 \times (V_o - V_1)}{4V_2 - V_1} - 3]. \qquad \{4\}$$

where V_0 is the volume of the $KMnO_4$ solution which is used to titrate the same volume of Fe(II) acidic solution as that used for dissolving the solid samples, i.e. a blank titration; V_1 and V_2 are the volumes of the $KMnO_4$ solutions consumed in the first and the second titration, respectively.

Thus, a series of titrations were carried out and then x values calculated from equation {4}. Table 5-4-3 presents the results for different spinels fired at different temperatures indicating that the products from the solution synthesis are a series of oxygen-rich spinels, and that the content of oxygen depends on the firing temperature. For example, a stoichiometry of $LiMn_2O_{4.1}$ is obtained by firing at 200 °C (sMn200), and $LiMn_2O_{4.02}$ by firing at 700 °C (sMn700). Stoichiometric $LiMn_2O_4$ can be obtained from the solution synthesis if the firing temperature is 850 °C. The result of the same chemical analysis for the spinel formed by solid state reaction at 850 °C (ssMn850) is also included in the table. The conventional solid state reaction yields a stoichiometric spinel. The slight difference in composition between the materials fired at 200 °C with and without carbon is probably within the relative errors of the analyses which are estimated to be ± 6 %. On dissolution of the sample with carbon, fine black particles of carbon were observed confirming that the carbon was still present after firing at 200 °C.

Table 5-4-3: Titration data and calculated x values for various spinels prepared by the solution synthesis but at different temperatures (* the spinel from solid-state reaction at 850 °C).

Samples	V_0(ml)	V_1(ml)	V_2(ml)	x	$\bar{x}$
sMn200	19.47 19.47 9.74	9.89 10.49 5.54	9.94 9.63 4.65	0.10 0.10 0.11	0.10
scMn200	14.60 14.60	9.60 6.80	6.35 7.83	0.08 0.09	0.09
sMn300	19.98 19.98 19.98	1.40 2.20 5.85	15.05 14.67 12.64	0.08 0.07 0.08	0.08
sMn700	19.98 9.99	13.12 6.25	8.91 4.64	0.02 0.02	0.02
sMn850	19.47 19.47	8.64 9.65	11.15 10.55	0.00 0.01	0.00
ssMn850*	15.00 15.00	6.75 7.68	8.60 8.04	-0.01 0.00	0.00

5-4-5 Electrochemical behaviour

The spinels from the solution synthesis have been characterised by powder X-ray diffraction and chemical analysis. As far as oxygen content is concerned, the 200 °C spinel ($LiMn_2O_{4.1}$) may be related to $Li_2Mn_4O_9$ ($LiMn_2O_{4.5}$) which also possesses a spinel structure but operates in 3 volts only [32-34]. Cyclic voltammetry is a simple and

fast method of characterising the electrochemical properties of materials. Thus the spinel sMn200, sMn600 and ssMn850 were subjected to cyclic voltammetry below. In addition, $Li_2Mn_4O_9$ was prepared based on the method of Thackeray *et al.* [32, 34] and then also subjected to the same study. All spinel materials studied were mixed with carbon black and PTFE to fabricate composite electrodes as working electrodes in a three electrode cell in which reference and counter electrodes are made from lithium metal (see CHAPTER THREE for further details). The electrolyte was 1 M $LiAsF_6$ in PC.

Fig 5-4-4 compares the cyclic voltammograms for $LiMn_2O_{4.1}$ (sMn200) and $Li_2Mn_4O_9$ in which the potential sweep was initially swept cathodically and then cycled between 1.8 and 4.4 V at 0.2 $mV \cdot s^{-1}$. $Li_2Mn_4O_9$ exhibits a pair of redox peaks between 2.0 V and 3.5 V, while relatively small redox currents appear at potentials higher than 3.5 V (Fig 5-4-4 (a)). This reflects that fact that this material is a 3 volts cathode. By contrast, $LiMn_2O_{4.1}$ produces a second pair of redox peaks at the higher potential range in addition to the redox peaks between 2.0 V and 3.5 V (Fig 5-4-4 (b)), as expected for a spinel based on stoichiometric $LiMn_2O_4$ [3].

Since ionic diffusion within an intercalation host is slow, slow sweep cyclic voltammetry is always favoured in order to resolve clearly intercalation / deintercalation processes in detail. Voltammetric experiments at a scan rate of 10 $\mu V \cdot s^{-1}$ were thus performed for the three spinels, sMn200, sMn600 and ssMn850. Potential was first scanned cathodically and then cycled between 3.5 V and 2 V two or three times followed by two scans between 4.3 V and 2.0 V. The cyclic voltammograms in Fig 5-4-5 indicate that the solution based spinels whether fired at low temperature (200 °C) or high temperature (600 °C) remain similar to the electrochemistry of $LiMn_2O_4$. The pair of symmetric redox peaks in the region from 2.0 V to 3.5 V correspond to reversible lithium insertion, whereas the redox peaks at the higher potential region from 3.5 V to 4.3 V is due to a reversible extraction of lithium from the spinel host. Because of the use of a slow scan rate, lithium ordering during intercalation / deintercalation in this high potential range can be observed as peak splitting when compared with the cyclic

voltammograms in Fig 5-4-4. Evidently, the solution based spinels can be used as 3 volt and 4 volt cathodes in lithium batteries. However, it is noticeable from Fig 5-4-5 (a) that the charge in the higher potential range is apparently smaller that in the lower potential range in contrast to the case of ssMn850 which shows almost equal charge for both ranges. This implies that the defect spinel has different capacities when used as 3 V or 4 V cathodes, as will be discussed further in CHAPTER SIX. The abnormal current on scan reversal after polarising to 4.3 V in the case of sMn600 (Fig 5-4-6 (b)) is merely due to electrolyte oxidation on the stainless steel substrate (see CHAPTER FOUR).

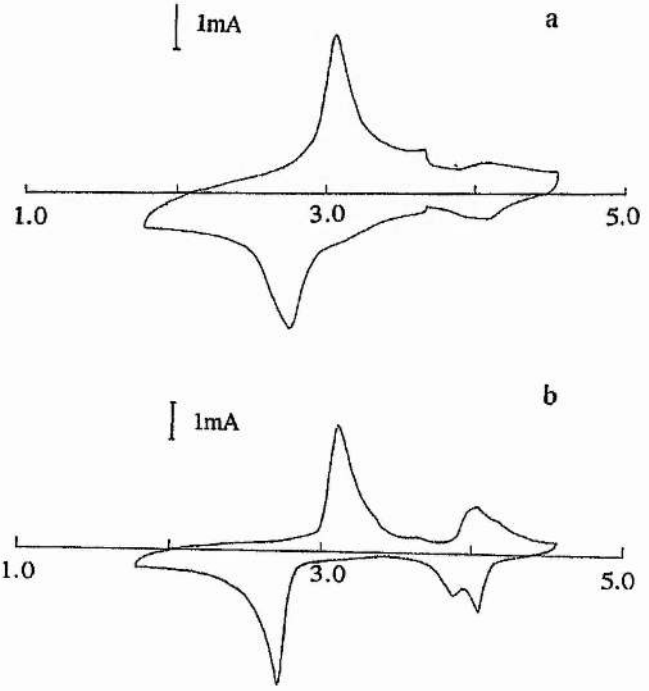

Fig 5-4-4 Cyclic voltammograms for $Li_2Mn_4O_9$ (a) and $LiMn_2O_{4.1}$ (b) (0.2 $mV \cdot s^{-1}$).

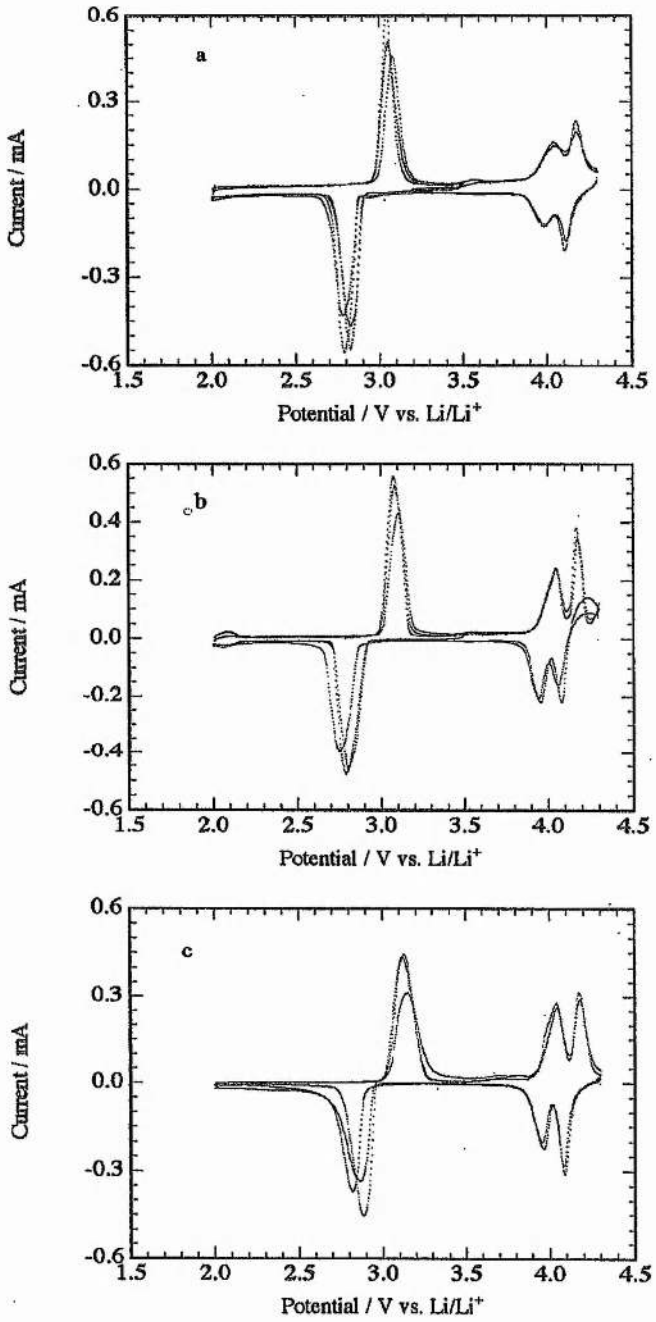

Fig 5-4-5 Cyclic voltammograms for the lithium manganese oxides spinels prepared from the solution synthesis fired at 200 °C (a), 600 °C (b), and from the solid-state reaction fired at 850 °C (c).

5-5 Conclusions

Lithium manganese oxide spinels are obtainable from a new solution synthesis. Based on this method, spinel products fired at 200 to 600 °C possesses very small particle size, around several hundred angstroms compared with the micrometer magnitude in literature work [11]. The solution based spinels possess a variable oxygen content depending on the firing temperature. A single spinel phase may be obtained at temperature as low as 200 °C and with a formula of $LiMn_2O_{4.1}$. Firing at 700 °C yields a material with composition $LiMn_2O_{4.02}$. At 850 °C, a composition very close to $LiMn_2O_4$ is obtained. Electrochemically, all these solution products retain the characteristic feature of $LiMn_2O_4$ and so can be used as 3 V or 4 V cathodes in lithium batteries.

X-ray diffraction studies suggests that spinel formation occurs via an intermediate with the γ-Mn_2O_3 structure. Reaction steps during synthesis may consist of:

$$\text{solution based precursors} \xrightarrow{200^oC} \text{a decomposed product} + O_2$$

$$\xrightarrow{200^oC} \gamma\text{-}Mn_2O_3 \text{ phase} + O_2$$

$$\xrightarrow{200^oC} LiMn_2O_{4+x},$$

$$\xrightarrow{>700^oC} LiMn_2O_4.$$

References

[1] D.G.Wickham, and W.J.Croft, J. Phys. Chem. Solids, **7** 351 (1958).

[2] J.C.Hunter, J. Solid State Chem., **39** 142 (1981).

[3] J.C.Hunter, and F.B.Tudron, Proc. Electrochem. Soc., **P1-3** 444 (1991).

[4] A.Mosbah, A.Verbaere, and M.Tournoux, Mat. Res. Bull., **18** 1375 (1983).

[5] M.M.Thackeray, W.I.F.David, P.G.Bruce, and J.B.Goodenough, Mater. Res. Bull., **18** 461 (1983).

[6] J.B.Goodenough, M.M.Thackeray, W.I.F.David, and P.G.Bruce, Revue de Chimie Minerale, **21** 435 (1984).

[7] M.M.Thackeray, P.J.Johnson, L.A.de Picciotto, W.I.F.David, P.G.Bruce, and J.Goodenough, Mat. Res. Bull, **19** 179 (1984).

[8] J.B.Goodenough, Proc.-Electrochem. Soc., **85-4** 77 (1985).

[9] T.Ohzuku, H.Fukuda, and T.Hirai, Chemistry Express, **2** 543 (1987).

[10] T.Ohzuku, M.Kitagawa, and T.Hirai, J. Electrochem. Soc., **137** 769 (1990).

[11] V.Manev, A.Momchilov, A.Nassalevska, and A.Kozawa, J. Power Sources, **43-44** 551 (1993).

[12] T.Nohma, Y.Yamamoto, I.Nakane, and N.Furukawa, J. Power Sources, **39** 51 (1992).

[13] T.Nohma, and N.Furukawa, Proc-Electrochem. Soc., **91-3** 311 (1990).

[14] T.Nohma, Y.Yamamoto, K.Nishio, I.Nakane, and N.Furukawa, J. Power Source, **32** 373 (1990).

[15] T.Nohma, T.Saito, N.Furukawa, and H.Ikeda, J. Power Source, **26** 389 (1989).

[16] N.Furukawa, T.Nohma, K.Teraji, I.Nakane, Y.Yamamoto, and T.Saito, DENKI KAGAKU, **57** 533 (1989).

[17] M.M.Thackeray, M.H.Rossouw, A de Kock, A.P.de la Harpe, R.J.Gummouw, K.Pearce, and D.C.Liles, J. Power Sources, **43-44** 289 (1993).

[18] M.H.Rossouw, A.de Kock, L.A.de Piciotto, M.Thackeray, W.I.F.David, and R.M.Ibberson, Mat. Res. Bull., **25** 173 (1990).

[19] T.Ohzuku, K.Sawai, and T.Hirai, Proc-Electrochem. Soc., **P1-3** 318 (1991).

5-2 Experimental.

[20] T.Ohzuku, K.Sawai, T.Hirai, Chemistry Express, **4** 777 (1989).

[21] T.Ohzuku, K.Sawai, T.Hirai, Chemistry Express, **4** 773 (1989).

[22] T.Nagaura, M.Yokoawa, and T.Hashimoto, Br. Patent No. 2 196 785 (1988).

[23] W.J.Macklin, R.J.Neat, and R.J.Powell, J. Power sources, **34** 39 (1991).

[24] A.Momchilov, V.Manev, A.Nassalevska, and A.Kozawa, J. Power Sources, **41** 305 (1993).

[25] V.Manev, A.Momchilov, A.Nassalevska, and A.Sato, J. Power Sources, **54** 323 (1995).

[26] J.M.Tarascon, W.R.McKinnon, F.Coowar, T.N.Bowmer, G.Amatucci, and D.Guyomard, J. Electrochem. Soc., **141** 1421 (1994).

[27] J.M.Tarascon, E.Wang, F.K.Shokoohi, W.R.McKinnon, and S.Colson, J. Electrochem. Soc., **138** 2859 (1991).

[28] R.Bittihn, R.Herr, and D.Hoge, J. Power Sources, **43-44** 223 (1993).

[29] R.J.Gummouw, A de Kock, and M.M.Thackeray, Solid State Ionics, **69** 59 (1994).

[30] G.Pistoia, G.Wang, and C.Wang, Solid State Ionics, **58** 285 (1992).

[31] Wang Baochen, Xia Yongyao, Li Feng, and Zhao Dongjiang, J. Power Sources, **43-44** 539 (1993).

[32] M.M.Thackeray, A.de Kock, M.H.Rossouw, D.Liles, R.Bittihn, and D.Hoge, J. Electrochem. Soc., **139** 363 (1992).

[33] M.M.Thackeray, A.de Kock, M.H.Rossouw, D.Liles, R.Bittihn, and D.Hoge, Proc-Electrochem. Soc., **P1-3** 326 (1991).

[34] A.de Kock, M.H.Rossouw, L A de Picciotto, M.M.Thackeray, W I F David, and R.M.Ibberson, Mat. Res.Bull., **25** 657 (1990).

[35] P.Barboux, J.M.Tarascon, and F.K.Shokoohi, J. Solid state Chem., 94 185 (1991).

[36] S.Bach, J.P.Pereir-Ramos, N.Baffier, and R.Messina, Electrochimica Acta, **36** 1595 (1991).

[37] (a) U.K. Pat. application 9305440.1 (filed 1993): (b) U.K. Pat. application 9305457.5 (filed 1993).

[38] H.Huang, and P.G.Bruce, J. Electrochem. Soc., **141** L76 (1994).

[39] H.Huang, and P.G.Bruce, J. Electrochem. Soc., **141** L106 (1994).

[40] Joerg Kaspar, Report for Senior Honours Research Project, University of St. Andrews, 1994.

[41] Comprehensive Inorganic Chemistry, edited by J.C.Bailar Jr. *et al.*, Pergamon Press, Volume 3, 801 (1973).

[42] G.Pistoia, and G.Wang, Solid State Ionics, **66** 135 (1993).

[43] Anthony R.West, Solid State Chemistry and its Applications, 1984, John Wiley & Sons Ltd.

[44] B.B.Bokhonov, I.G.Konstanchuk, V.V.Boldyrev, Mat. Res. Bull., **30** 1277 (1995).

[45] H.P.Klug and L.E.Alexander, "X-ray diffraction procedures for polycrystalline and amorphous materials", wiley, New York (1954).

[46] K.J.Vetter, N.Jeager, Electrochemica Acta, **11** 401 (1966).

CHAPTER SIX

Electrochemical Studies of Spinel Lithium Manganese Oxides for 4 V Lithium Batteries

6-1 Introduction

Only three intercalation compounds, $LiMn_2O_4$, $LiCoO_2$ and $LiNiO_2$, are known to possess oxidising potentials as high as 4 V vs Li/Li^+. The success of a commercial lithium ion battery system based on the $LiCoO_2$ cathode, launched onto the market by the Sony Corporation [1] in the early 1990s, has generated a great deal of interest in such highly oxidising cathode materials. The fact that manganese compounds are cheaper and less toxic than the equivalent Co and Ni materials means that the next generation of commercial lithium ion batteries is likely to be manganese oxides.

Lithium manganese oxide spinel $LiMn_2O_4$ is a unique intercalation electrode in that it can exhibit intercalation/deintercalation at both 3 V and 4 V vs Li/Li^+ [2-5], i.e.

$$LiMn_2O_4 + Li^+ + e^- \leftrightarrow Li_2Mn_2O_4 \qquad \text{(3 V plateau)},$$

$$LiMn_2O_4 - Li^+ - e^- \leftrightarrow 2\lambda - MnO_2 \qquad \text{(4 V plateau)};$$

the manganese spinel $LiMn_2O_4$ is the only cathode material, known to date, from which both 3 V and 4 V rechargeable lithium cells may be fabricated in contrast to other manganese oxides such as $Li_2Mn_4O_9$ and CDMO, from which only 3 V lithium cells can be constructed. $LiMn_2O_4$ spinel was originally recognised as an intercalation cathode by Bruce, David, Thackeray and Goodenough in the 1980s [2-4]. Since the 1990s, this compound has been under intensive investigation as a 4 V electrode for rechargeable lithium batteries [6-23]. Early studies indicated that the compound could not yield high practical capacity, lower than 80 $mAhg^{-1}$ even at a relatively low rate

of C/10 [23]. Only recently, has progress in this aspect been made. For example, Manev *et al.* claimed a synthesis of material that exhibited an initial capacity of 134 $mAhg^{-1}$ at a discharge rate of C/3 [21], and Tarascon *et al.* reported an initial capacity of 125 $mAhg^{-1}$ at the same discharge rate [8]. In their studies, however, lithium manganese oxide spinels were still synthesised by solid-state reaction, using MnO_2 along with either Li_2CO_3 or $LiNO_3$ as the starting materials and at temperature of 800 °C [8] or 700 °C [21, 22].

We have discussed a new solution route to the synthesis of lithium manganese oxide spinel, as described in CHAPTER FIVE. In this chapter the solution based spinels are investigated as 4 volts cathodes in rechargeable lithium batteries. In order to match practical criteria, these cathodes were subjected to cycling tests under relatively rigorous conditions, e.g. a discharge rate of C/2, and the cells were charged and discharged for 300 cycles. As a result of these studies, the spinel prepared from the solution synthesis but fired at 600 °C shows very promising performance for battery applications [24]. The cycling tests were carried out in two liquid electrolytes: 1 M $LiClO_4$ in propylene carbonate (PC) and 1 M $LiPF_6$ in a mixture of ethylene carbonate (EC) and dimethyl carbonate (DMC) (1:1 by volume). The cycling performance of the spinel based cathodes was shown to be influenced by the electrolytes, thus this chapter also attempts to understand the factors related to capacity retention.

6-2 Spinels for use as 4 volts cathode materials

As indicated in CHAPTER FIVE, lithium manganese oxide spinel can be prepared at 200 °C with an oxygen-rich composition, but the composition of the spinel product will approach to that of the stoichiometry material $LiMn_2O_4$ as the firing temperature is increased. In this section we investigate the 4 volt performance of these solution based spinel products fired at different temperatures.

6-2-1 Spinel compositions and theoretical capacities

Lithium manganese oxide spinel with the stoichiometric composition $LiMn_2O_4$ possesses a theoretical capacity of 148 $mAhg^{-1}$ associated with each of its discharge plateaux. The stoichiometry of the spinels prepared from solution synthesis depends however on the temperature used to fire the materials. Lower temperatures result in more oxidised spinels with the composition $LiMn_2O_{4+x}$. Table 6-2-1 summaries the influence of heating temperature on stoichiometry and as a consequence the theoretical capacity (based on the average Mn oxidation state) for the extraction (4 V) and insertion (3 V) of lithium. This indicates that the capacity of the 4 V electrode increases with higher stoichiometry as the composition approaches $LiMn_2O_4$, while that of 3 V electrode decreases. Therefore, a high temperature spinel should be chosen as the 4 V cathode material.

Table 6-2-1 The nominal capacities calculated from spinel stoichiometric compositions

	heating temperature (°C)	spinel composition $LiMn_2O_{4+x}$		
		x*	Q_{3V}** ($mAhg^{-1}$)	Q_{4V}** ($mAhg^{-1}$)
solid state reaction	850	0.00	148	148
solution synthesis	850	0.00	148	148
	700	0.02	156	140
	300	0.08	170	124
	200	0.10	176	118

* see Table 5-4-3 in CHAPTER FIVE.

** theoretical specific capacities for a 3V and 4V cell, respectively.

6-2-2 Practical capacities of spinels

Several spinel oxides prepared by the solution synthesis but fired at different temperatures such as 200, 500, 600, 700 and 850 °C (denoted as sMn200, sMn500, sMn700 and sMn850, respectively) were used to fabricate composite cathodes and then three electrode cells (see Fig 3-4-1) were constructed to determine their practical capacities. The cathodes were cycled between 4.4 V and 3.3 V cut-offs at discharge and charging current densities of 1 and 0.5 $mA \cdot c\,m^{-2}$, the discharge current corresponded to a rate of C/2. The electrolyte used was 1 M $LiClO_4$ in PC. The practical capacities for these spinel oxides are obtained by averaging over the first four cycles. These values are plotted against heating temperature in Fig 6-2-1, from which it can be seen that the practical capacity of the spinels increases with increasing temperature until 600 °C at which a maximum capacity is reached, consistent with the predication based on theoretical capacities in Table 6-2-1. Beyond 600 °C, the practical capacities of the spinels decrease with rising temperature.

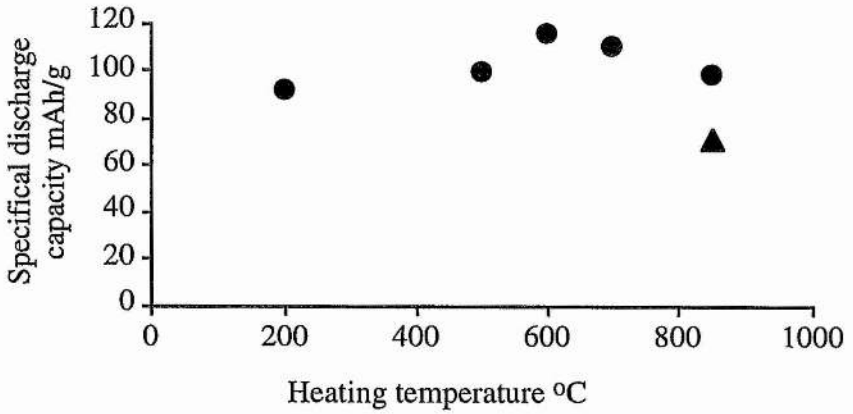

Fig 6-2-1 Initial discharge capacities for lithium manganese oxides prepared from the solution synthesis but fired at different temperature (●), or from the solid-state reaction at 850 °C (▲).

It is well known that particle size and crystallinity generally increase with increasing temperature of firing. Both these factors also play an important role along with stoichiometry in determining the performance of intercalation electrodes. For example, the smaller the particle size the lower is the true current density for a given

effective current. This reduces the polarisation arising from the lithium concentration gradient within the intercalation host. In CHAPTER FIVE, the TEM experiment showed that the particle size of spinels did not change very much from 200 °C to 600 °C. This is because the solution synthesis makes it possible to form the spinel phase at 200 °C, lower than any other synthesis, and the composition of the spinel can then be modified by further heating at a higher temperature but without significant increase in particle size [22]. As indicated by the chemical analysis in CHAPTER FIVE, the defect spinel formed at 200 °C is oxygen rich, but the stoichiometric composition of high temperature spinel (e.g. 700 °C) will be much close to $LiMn_2O_4$. Of course, the crystallinity of spinel significantly increases with increasing temperature as is evident from X-ray diffraction. Thus, there undoubtedly exists an optimal temperature for preparing 4 volt spinel cathode material with a high performance. The spinel fired at 600 °C should possess a composition similar to that of the 700 °C spinel. This spinel therefore possesses a high theoretical capacity, while its particle size remains small. As a result, the 600 °C spinel exhibits the best performance in term of practical capacity.

A critical criterion for a cathode material suitable for rechargeable cells is its cycle life (cyclability). Thus, the composite cathodes based on sMn200, sMn600 and sMn850 spinels were further cycled many times under the same conditions as those in Fig 6-2-1. Their capacities are plotted against cycle number in Fig 6-2-2, showing that the cathode material prepared at 600 °C not only possesses the highest capacity but in addition exhibits the best capacity retention. It is interesting to note that the sMn200 cathode has a high capacity retention in the first twenty cycles, but thereafter decays more rapidly. By considering the experimental results of the anodic oxidation of $LiClO_4$/PC on the surface of manganese spinels in Fig 4-4-2 which shows a much higher current at a given potential with sMn200 than sMn600, the declining capacity of the sMn200 cathode may involve the electrolyte oxidation which occurs at a higher rate on the surface of this oxide. The situation for the sMn850 cathode is different. Its capacity deterioration may be related to the adverse action of high crystallinity, like

the spinel prepared by solid state reaction at high temperature. Once again, the particle size and crystallinity of the material show their effects on material performance so that the preparation temperature is always a critical factor to be considered.

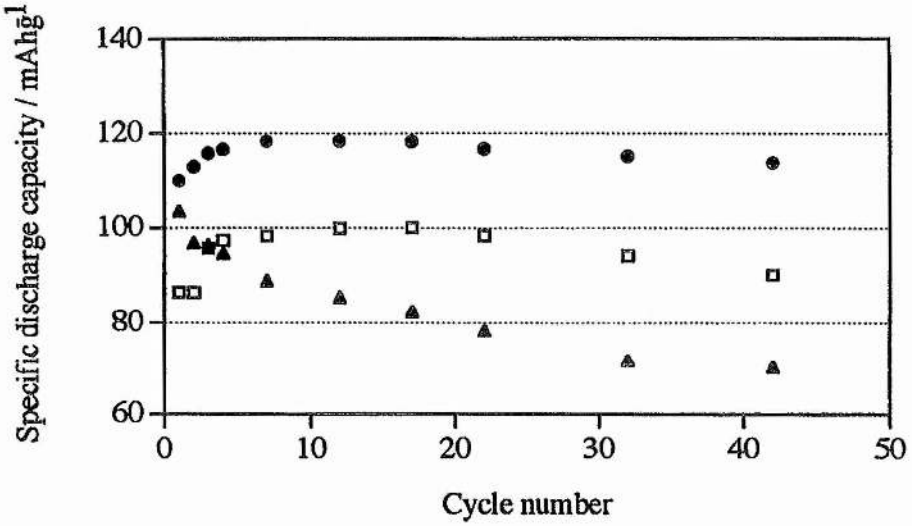

Fig 6-2-2 Capacity retentions for composite cathodes as a function of cycle number: (a) ● sMn600, (b) □ sMn200 and (c) ▲ sMn850 oxide materials. The cut-off limits were 4.4 V and 3.3 V and the discharge and charging current densities were 1 and 0.5 $mA \cdot cm^{-2}$, respectively.

As a comparison, the practical capacity of the spinel prepared from the conventional solid state reaction at 850 °C (denoted as ssMn850) was also included in Fig 6-2-1 showing that it has the worse practical capacity compared with all products from the solution synthesis. Interestingly, when prepared at 850 °C, the solution based spinel (sMn850) is better than the ssMn850 spinel in capacity. This is likely to be related to particle size. The particle size of ssMn850 has yet to be determined, but from the work of others using the same solid state procedure we may assume a value of 0.1 $m^2 \cdot g^{-1}$ for the specific surface area [23]. This value is equivalent to a particle size (diameter) of 10 μm by assuming the particles as spheres, and contrasts with the particle size of around 40 nm for the solution based spinel product as measured by TEM (see CHAPTER FIVE). In a conclusion, the solution synthesis is able to produce

spinel materials with small particles. The spinel fired at 600 °C has better performance in terms of practical capacity and capacity retention than spinels fired at other temperatures. Compared with literature methods, it is clear that the solution synthesis is a promising low temperature route to prepare 4 volts spinel cathode materials.

6-3 Electrochemical characterisation and cathode performance

In the following, we focus mainly on studies of the spinel prepared by solution synthesis fired at 600 °C. The cathodes based on this material were subjected to long term cycling under a high discharge rate typically C/2. The electrolytes used were $LiClO_4$/PC and $LiPF_6$/EC+DMC. The latter electrolyte system has been suggested as the best candidate for practical use [19]. In addition, other electrochemical studies such as cyclic voltammetry were also carried out to more fully characterise the spinel.

6-3-1 Charge and discharge curves

The sMn600 spinel was subjected to galvanostatic charging to 4.4 V and then discharging to 3.3 V at a current of 1.5 $mA \cdot g^{-1}$. There was a period of 12-15 hours where the cell stood on open-circuit between the charging and discharging processes. Fig 6-3-1 presents the variations of the potentials of the spinel electrode on charge and discharge as a function of the electrode capacity. For comparison results on sMn200 and the material prepared by solid state reaction and fired at 850 °C (ssMn850) are also included. The sMn600 spinel has the smallest gap between the discharge and charge curves, reflecting a relatively low polarisation, as expected for a high performance material. The solution material fired at 600 °C and the solid state material at 850 °C both show a step in the charge and discharge curves separating two voltage plateaux. This has been ascribed to lithium ordering.

Table 6-3-1 The charged capacities measured from the curves in Fig 6-3-1.

sMn200	sMn600	ssMn850
118.9 ($mAh \cdot g^{-1}$)	138.0 ($mAh \cdot g^{-1}$)	138.2 ($mAh \cdot g^{-1}$)

From these charging curves, the amounts of lithium extracted from the three spinels were determined, see Table 6-3-1. The measured capacities for sMn200 and ssMn850 are very similar to the calculated values reported in Table 6-2-1 supporting the stoichiometries determination by potentiometric titration (CHAPTER FIVE). Therefore, one may assume that the composition of sMn600 is similar to that of sMn700, i.e. $LiMn_2O_{4.02}$.

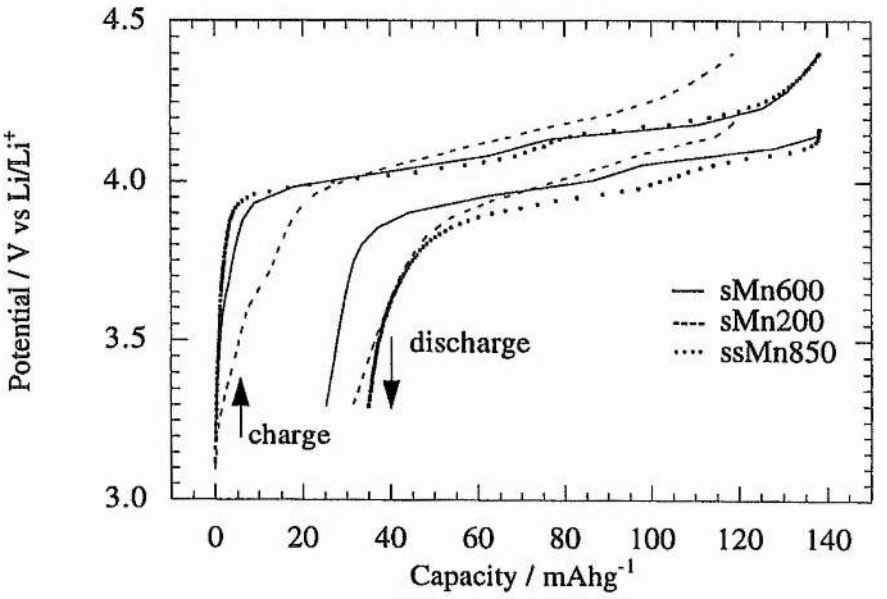

Fig 6-3-1 Charge and discharge curves of lithium manganese oxide spinels (in 1 M $LiClO_4$/PC electrolyte and at 0.2 $mA \cdot cm^{-2}$ of current).

The shape of charging and discharging curves of sMn200 is somewhat special: sloped and with higher potential on charge. This is probably not due to concentration polarisation within particles. Instead it may arise from local structure disorder or the fact that for a given lithium content (capacity) the average Mn oxidation state is

higher in $LiMn_2O_{4.1}$ than sMn600 or ssMn850. As the voltage increase with increasing oxidation state in all cases, it may be that the higher oxidation state for the same amount of lithium extracted is, at least in part, responsible for the higher voltage.

6-3-2 Cyclic voltammograms

The sMn600 spinel was further characterised by cyclic voltammetry and compared with the ssMn850 spinel, see Fig 6-3-2. An interesting point is that the sMn600 spinel has no redox peaks at 4.5 V, whereas the ssMn850 spinel does. According to the values in Table 6-3-1, only 93 % of lithium was extracted from the ssMn850 spinel up to a cut-off of 4.4 V while the sMn600 spinel delivers almost all its lithium (99 %) during charging based on the $LiMn_2O_{4.02}$ stoichiometry, so that the extra peak at 4.5 V should correspond to the remainder of lithium in ssMn850 which needs higher energy to be extracted.

Tarascon *et al.* [7-9] also observed this redox process at +4.5 V in the cyclic voltammogram of the spinel prepared from solid-state reaction. The existence and magnitude of the 4.5 V peaks were strongly dependent on preparation conditions such as annealing temperatures and cooling rates [8], and a high performance spinel was characterised by the absence of the +4.5 V peaks [9]. They ascribed the production of the peaks to a small proportion of Mn ions present in tetrahedral sites of the spinel which oxidise less readily compared with Mn ions in octahedral sites [8]. However, recently Dahn has shown that the 4.5 V Peak does not correlate to Mn in the tetragonal site [25]. Hence the precise origin of the peak is not clear. Tarascon *et al.* also reported there were other small redox peaks occurring at around 4.9 V, ascribed either to the oxidation of Mn^{4+} to Mn^{5+} or to the removal of Li from a 16d site [8]. As shown in Fig 6-4-2, there is no evidence of a 4.9 V peak in either sMn600 and or ssMn850. More detailed studies of the Li/Mn distribution in the spinel will be

necessary to see if the separate redox peaks at 4.5 V is related to the site occupied by Li.

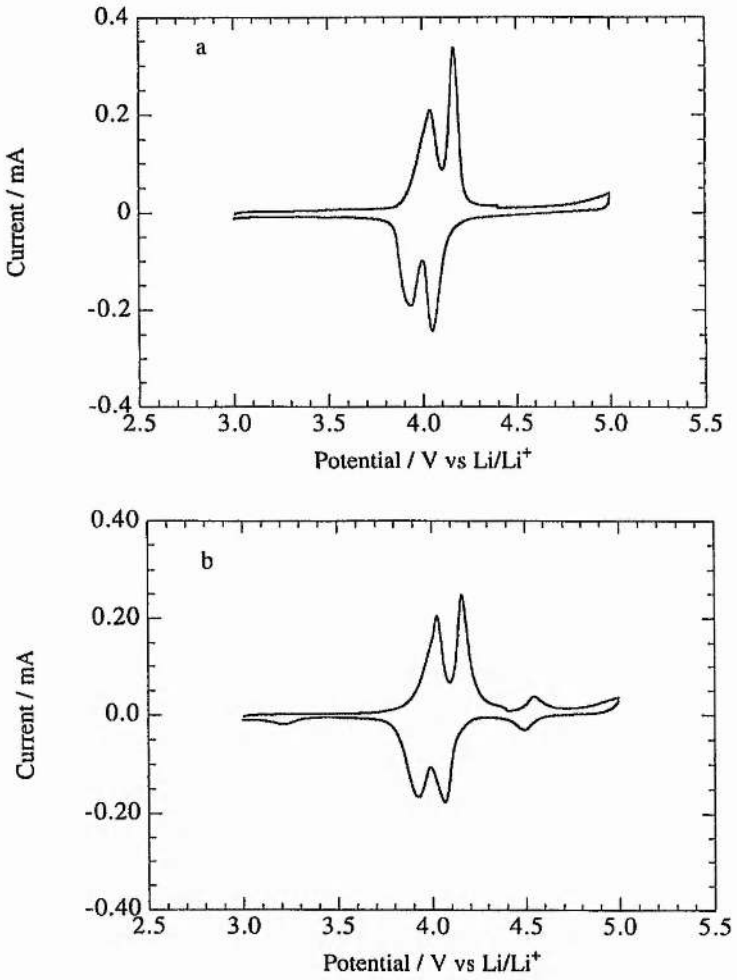

Fig 6-3-2 Cyclic voltammograms for composite electrodes of (a) the spinel from solution synthesis fired at 600 °C (sMn600) and (b) the spinel prepared by solid state reaction at 850 °C (ssMn850), at a scan rate of 10 $\mu V \cdot s^{-1}$ and in the electrolyte of 1M $LiPF_6$/EC+DMC.

6-3-3 Cycling performance in $LiClO_4$/PC

The cycling performance of the solution based material was first tested in the electrolyte of $LiClO_4$/PC. A three electrode cell with a sMn600 cathode was cycled between 4.4 V and 3.3 V and at discharge and charging current densities of 1 and 0.5 $mA \cdot cm^{-2}$. The discharge rate was C/2. The variation of capacity of the sMn600

cathode on cycling the cell is presented in Fig 6-3-3, where the result from a ssMn cathode is included for comparison. As can be seen, the cathode material prepared by our new solution route offers very substantial improvement in performance. The initial discharge capacity is over 115 $mAhg^{-1}$, rising slightly on the following few cycles, then declining by only 10 $mAhg^{-1}$ to 105 $mAhg^{-1}$ at 100 cycles, 90 $mAhg^{-1}$ at 200 cycles and 85 $mAhg^{-1}$ at 300 cycles. This represents very good capacity retention particularly in view of the relatively high discharge rate (C/2) and depth-of-discharge.

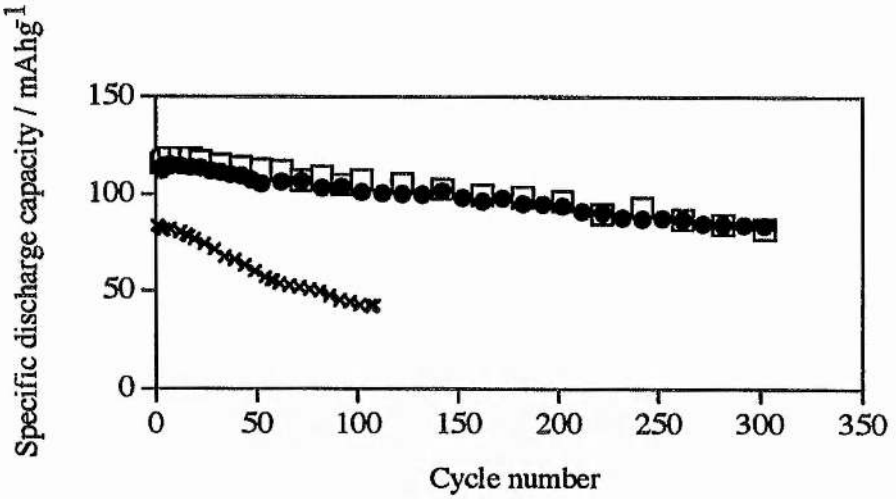

Fig 6-3-3 Variation of specific discharge capacity with the number of cycles for 4 V composite cathodes containing, lithium manganese oxide spinels synthesised from the solution route at 600 °C (□) without carbon, sMn600, and (●) with carbon, scMn600; or (x) prepared from the solid state reaction at 850 °C, ssMn.

Another cell was also assembled and tested under the same conditions but using the cathode material scMn600, i.e. the spinel prepared with carbon (see CHAPTER FIVE). The result is also presented in Fig 6-3-3 (filled circles). It is evident that the use of carbon in the synthesis has no apparent effect on the performance of the 4 volt material in complete contrast to the case of 3 V cycling, as will be described in CHAPTER SEVEN.

The effect of varying the discharge and charging currents on the specific discharge capacity is presented in Fig 6-3-4. Three different discharge and charging currents 0.5, 1 and 1.8 $mA{\cdot}cm^{-2}$ were considered. The specific discharge capacities represent the average obtained from the first four cycles. The overall trend is towards a lower discharge capacity at high charge or discharge currents although, when cycling at lower current densities, the influence of varying the magnitude of the current density on the discharge capacity is less significant than at high current.

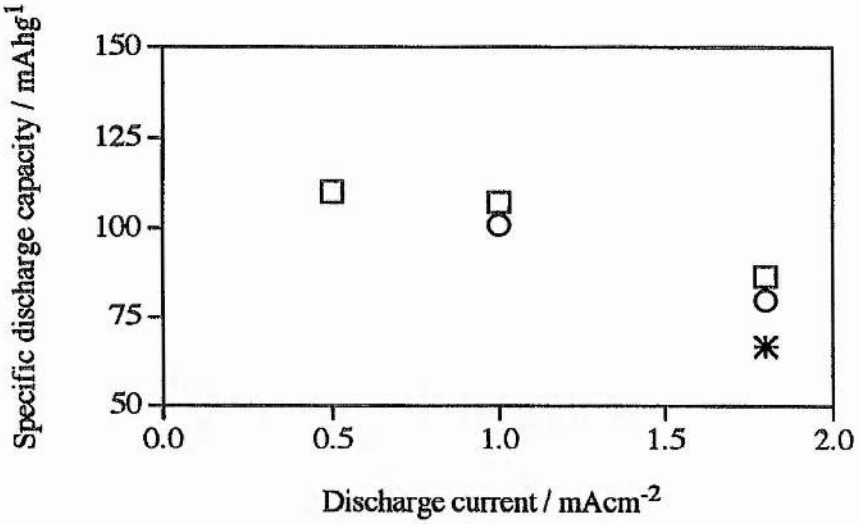

Fig 6-3-4 Influence of the current density on the specific capacity of the 4 V composite cathode. Cut-off potentials are those used in Fig 6-4-2 and the capacities are averaged over the first four cycles. Charging currents (□) 0.5 $mA{\cdot}cm^{-2}$; (○) 1 $mA{\cdot}cm^{-2}$, and (✳) 1.8 $mA{\cdot}cm^{-2}$.

6-3-4 Cycling performance in $LiPF_6$/EC+DMC

As discussed in CHAPTER FOUR, electrolytes consisting of a 1 M solution of $LiPF_6$ in a 1:1 ratio of EC and DMC are stable up to an oxidation potential of 5 V provided the working electrode substrate is aluminium. This is significantly more stable than 1 M $LiClO_4$ in PC (see **4-3** in CHAPTER FOUR). The wider anodic window of the $LiPF_6$ electrolyte permits the use of a higher charge cut-off. Thus, the sMn600 cathode material was tested in the $LiPF_6$/EC+DMC electrolyte under the same cycling

conditions as above but with higher cut-off potentials. As shown in Fig 6-3-5, there is no apparent difference in the shape of charging and discharging curves between the two electrolytes.

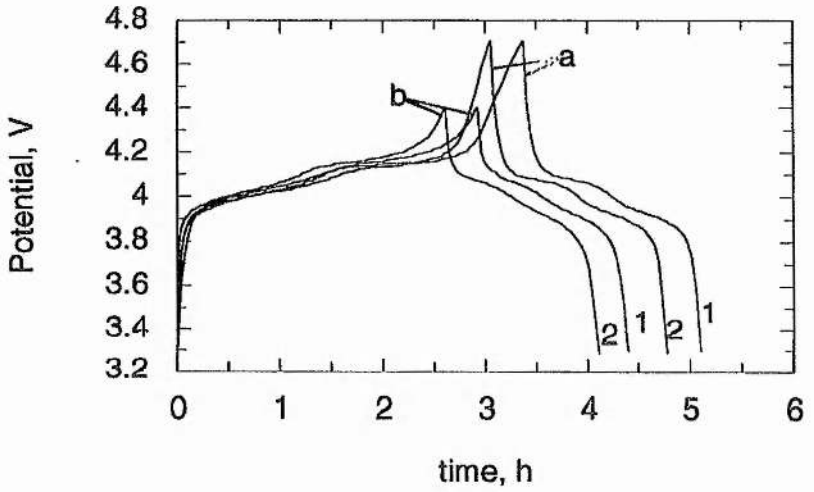

Fig 6-3-5 Charge and discharge curves for sMn600 based composite cathodes at I= 1 $mA{\cdot}cm^{-2}$, I_c = 0.5 $mA{\cdot}cm^{-2}$ in (a) $LiPF_6$/EC+DMC and (b) in $LiClO_4$/PC. The digits in the figure represent the cycle number.

Fig 6-3-6 presents the average discharge capacities over the first four cycles for different cut-off potentials. It is encouraging to note the initial capacity greater than 130 $mAhg^{-1}$ when used with a higher charge voltage. However, Fig 6-3-7 demonstrates the adverse effect of using a higher charge voltage on capacity retention. It is evident by comparing Fig 6-3-6 and Fig 6-3-7 that although a higher capacity is accessible by using a higher charge cut-off potential, such as 4.7 V, the retention of capacity becomes significantly worse. It can be seen from Fig 6-3-7 that cut-off potentials of 4.3 V and 3.1 V provide the optimum capacity retention (see the line marked with full triangles), comparable to the result with $LiClO_4$/PC. The variation of specific discharge capacity with cycle number for a sMn600 based cathode cycled in a 1 M solution of $LiPF_6$ in EC and DMC mixture (1:1) between the voltage limits of 4.3 V and 3.1 V and at a discharge current density of 1 $mA{\cdot}cm^{-2}$ (C/2) and charge current density of 0.5 $mA{\cdot}cm^{-2}$ is shown in Fig 6-3-8. The initial capacity was over 122 $mAhg^{-1}$, and a capacity of 110 $mAhg^{-1}$ remained after 100

cycles. Thus, an enhancement in capacity of 5 % after 100 cycles is obtained for the replacement of $LiClO_4$/PC by $LiPF_6$/EC+DMC.

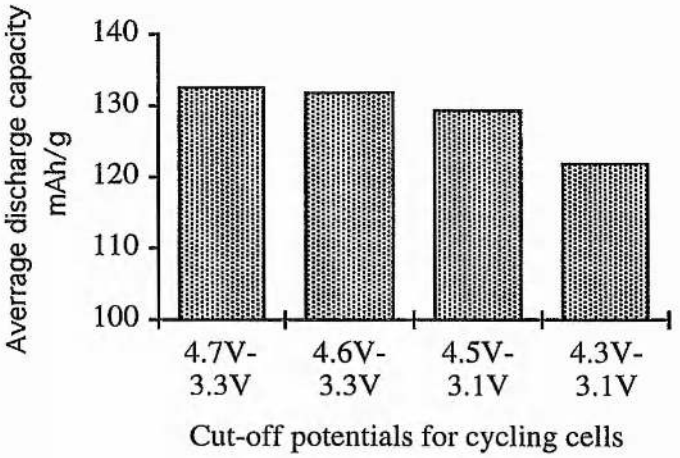

Fig 6-3-6 Initial capacities for the 600 °C spinel oxide, averaged over the first four cycles, in $LiPF_6$/EC+DMC with different cut-off potentials at 1 $mA \cdot cm^{-2}$ for discharging (C/2) and 0.5 $mA \cdot cm^{-2}$ for charging.

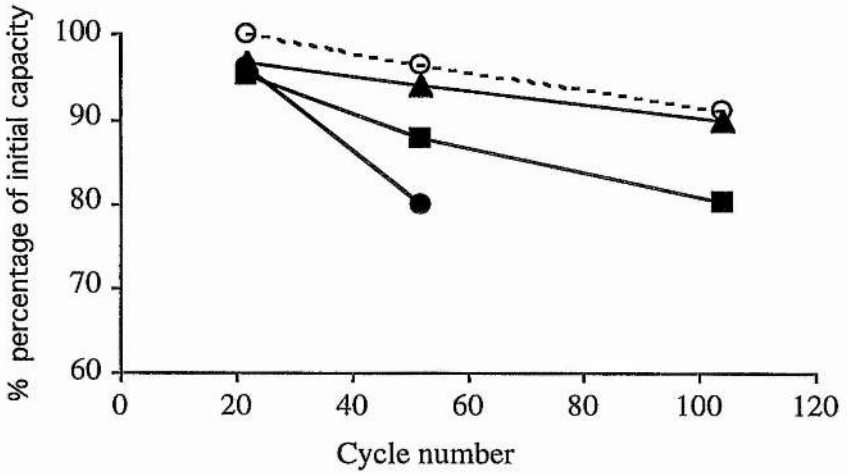

Fig 6-3-7 Decline of discharge capacity with cycle number in $LiPF_6$/EC+DMC with different cut-off potentials: (●) 4.7 V - 3.3 V, (■) 4.5 V -3.1 V, (▲) 4.3 V - 3.1 V; and (○) in $LiClO_4$/PC with 4.4 V -3.3 V.

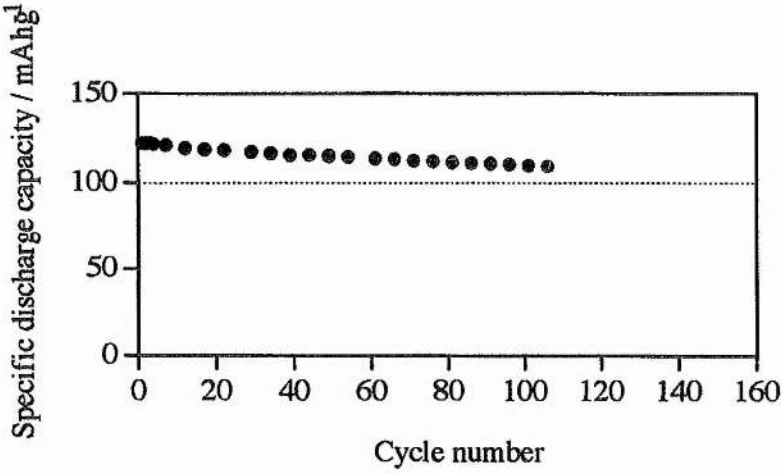

Fig 6-3-8 The retention of capacity of sMn600 cathode material cycled in $LiPF_6$/EC+DMC electrolyte and with 4.3 V - 3.1 V at a C/2 discharge rate.

6-4 Capacity fade and electrolytes

It is evident from the above that the chemical nature of electrolytes has a critical effect on the cathode capacity and cyclability. In order to gain further insight into the factors which may control such performance, the following experiments were carried out, which included the use of ac impedance technique.

6-4-1 Cell postmortems

After subjecting a cell to at least 100 charge/discharge cycles, cell postmortems revealed that the Whatman GF/F filter pads, containing the electrolyte (see Fig 3-4-1), showed no evidence of discolouration when the electrolyte was $LiPF_6$/EC+DMC, while a red-brown colour was apparent in cells containing $LiClO_4$ in PC. The colouration is probably an indication that some dissolution of manganese oxide in the electrolyte had occurred.

Electrolyte loss is more serious in the case of $LiPF_6$/EC+DMC than in $LiClO_4$/PC, for the pads were much dried when the former electrolyte was used. Whether the

electrolyte evaporates or is drawn into the porous cathode is not known. Two layers formed on the cathode, a thick white layer on the composite material and a grey layer on the Al substrate. This implied that some precipitation, passivation or/and evaporation processes is taking place in $LiPF_6$/EC+DMC environment.

6-4-2 Open-circuit potential of cathodes

On assembling a cell with a sMn600 cathode the open circuit potential was usually 3.3 ± 0.05 V in $LiClO_4$/PC and 3.45 ± 0.05 V in $LiPF_6$/EC+DMC. After cycling, the open-circuit potential was observed to change. The variation of open-circuit potential with cycling is shown in Fig 6-4-1, in each case the cell was cycled for two, twenty, fifty and one hundred times and after each of these sets of cycles the cell was left on open circuit for 18 hours in the discharged state before the potential was recorded. For the $LiPF_6$/EC+DMC electrolyte, the cathode potentials under open circuit conditions were related to the cut-off potentials applied during cycling. If the voltage limits are modest, e.g. 4.3 V-3.1 V, the open circuit potential varies only slightly over 100 cycles, but for more extreme cut-off voltages, the open circuit potentials gradually increase with cycle number, particularly in the case of 4.7 V-3.3 V cut-offs. By contrast, in the case of the $LiClO_4$/PC electrolyte, the cathode potential immediately increased in the first two cycles and then changed little during successive cycles.

Comparing Fig 6-4-1 with Fig 6-3-7, this potential increase with cycling is associated with the cathode capacity decline. There are two possibilities which may explain the increase of open circuit potential on cycling: first, after discharge the lithium content in spinel is less than in the original $LiMn_2O_4$ and this reduction of lithium content increases on cycling so that the open circuit potential of the cathode increases. A second possibility is the electrode surface is modified on cycling. However, the capacity retention for the cells studied above was similar in the first few cycles, while the potential increase depended on the electrolyte and the cut-off voltages, so that a change of the surface is likely to be the main reason for the increase in open-circuit

potential. We indeed observed the existence of a layer on the cathode as mentioned above. If this is so then the surface continues to change in the case of $LiPF_6$ based electrolytes but rapidly stabilises when $LiClO_4$ /PC is used.

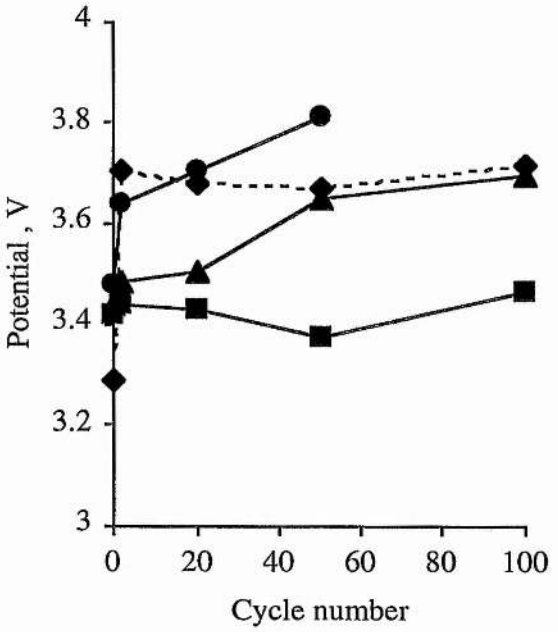

Fig 6-4-1 Open-circuit potentials for sMn600 composite cathodes before and after cycling in the $LiPF_6$/EC+DMC electrolyte: voltage limits were : (○) 4.7 V-3.3 V, (Δ) 4.5 V - 3.1 V, (□) 4.3 V - 3.1 V. Results for $LiClO_4$/PC electrolyte with 4.4 V - 3.3 V are also given (◆).

6-4-3 Ac impedance studies

In order to understand the role of electrolytes on cycle life of the cathode, sMn600 cathodes were further investigated by ac impedance, which is a technique sensitive to process in both the bulk and surface of the electrode, before and after long term cycling. The cells which underwent at least 100 cycles were reassembled by renewing the electrolyte and lithium counter electrode to reduce any possible influence from bulk electrolyte degradation or lithium dendrites on the ac impedance results. This may of course influence any interfacial change. However if a robust surface layer

forms as reported on $LiCoO_2$ [26], then its presence will still be observed in the refreshed cells. The cells were then cycled twice before ac impedance measurements were performed.

6-4-3-1 Ac impedance spectra before and after cycling

In the electrolyte $LiClO_4$/PC, the ac impedance spectra of the sMn600 cathode exhibits a number of changes after 300 cycles (Fig 6-4-2): the high frequency intercept on Z' axis has shifted from 20 to 45 Ω and the arc has increased in diameter from 35 to 60 Ω. Similarly, the sMn600 cathode also exhibits an increase in the high frequency intercept after cycling 100 times in the $LiPF_6$/PC+DMC electrolyte (Fig 6-4-3). However, the expansion of the arc in LiPF6/EC+DMC is much more significant, nearly three times higher than that in $LiClO_4$/PC, although the sizes of the arcs are very similar in both electrolytes before cycling.

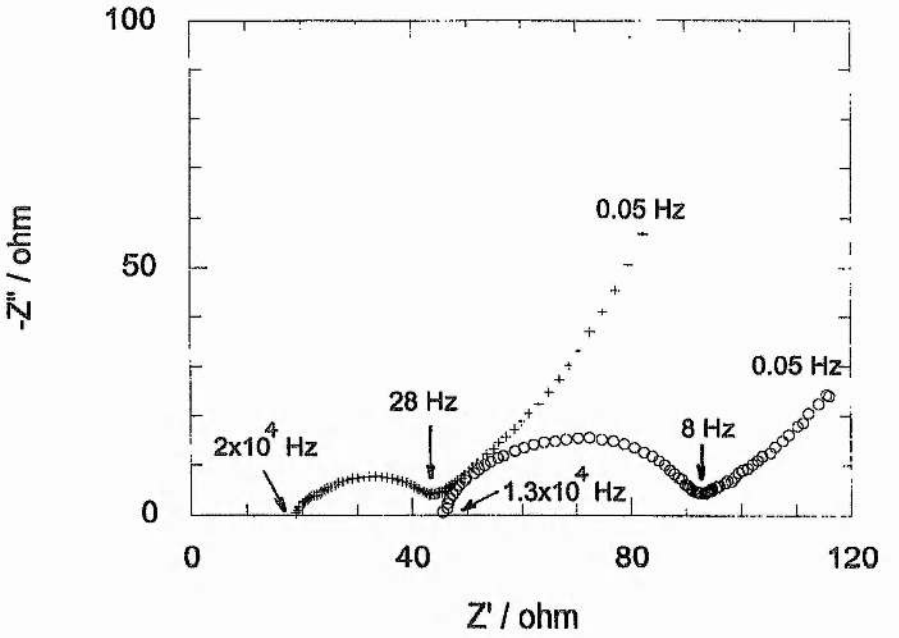

Fig 6-4-2 Ac impedance spectra for a sMn600 composite cathode measured initially (+) and after 300 cycles (○) in $LiClO_4$/PC with voltage limits of 4.4 V and 3.3 V and at a current density of 1 $mA \cdot cm^{-2}$ for discharging and 0.5 $mA \cdot cm^{-2}$ for charging.

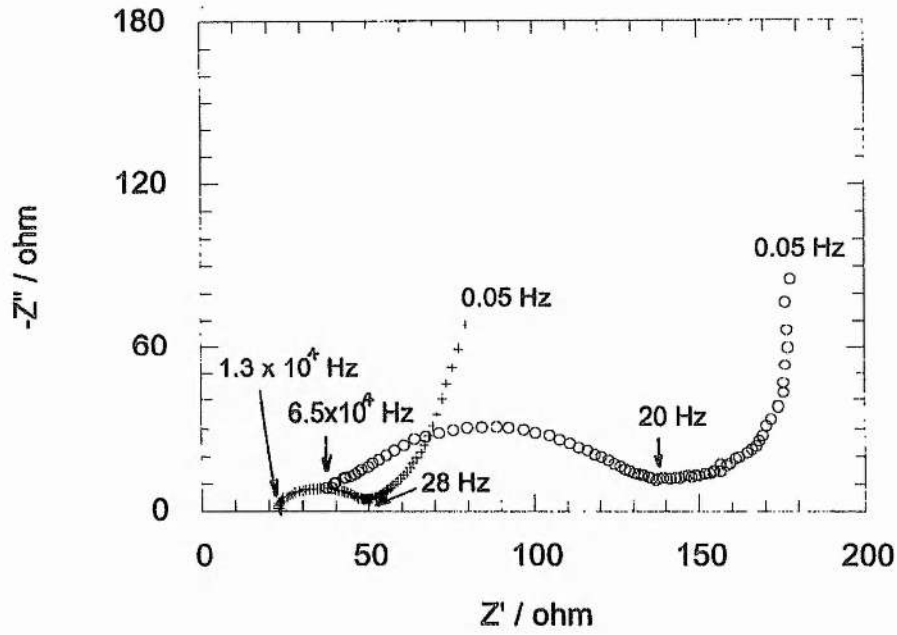

Fig 6-4-3 Ac impedance spectra for a sMn600 composite cathodes measured initially (+) and after 100 cycles (○) in $LiPF_6$/EC+DMC with voltage limits of 4.3 V and 3.1 V and at a current density of 1 $mA \cdot cm^{-2}$ for discharging and a current density of 0.5 $mA \cdot cm^{-2}$ for charging.

The high frequency intercept usually represents the electrolyte resistance (R_l), but possibly including the bulk resistance of electrode and the contact resistance between the electrode material and the metal substrate when these factors are not negligible. Since the electrolyte is renewed before measuring, this increase ought to relate to a change in the electrode/substrate contact and/or the electrode resistance. R_l increases relatively little in the case of the $LiPF_6$ electrolyte, however this may correlate with the fact that only 100 cycles were carried out in this electrolytes in contrast to 300 cycles in the $LiClO_4$ electrolyte.

Arcs in ac impedance are often called "semicircles", although they are frequently distorted or more semicircles may be observed depending on the electrode reaction mechanism [27, 28]. When a single semicircle is observed, it is often attributed to the intercalation process (R_f) and the electrode capacitance (C_{dl}) arising from a double layer on the electrode/electrolyte interface (see **2-4-3** in CHAPTER TWO). When there

is a surface layer on the electrode, another semicircle appears and is characterised using R_s and C_s parameters [26]. The thicker the surface layer, the larger the size of the semicircle (i.e. a big value of the R_s and a small value of the C_s [26]). Often these two semicircles overlap and even appear to be a broad and depressed semicircle if the time constants, R_fC_{dl} and R_sC_s are not significantly different. Since the cathodes were fabricated from identical materials but cycled in different electrolytes, the increase in the arcs after cycling in these two electrolytes should relate to the formation of a surface layer which much relies on the electrolyte used. Compared with cycling in $LiClO_4$/PC, the sMn600 electrodes have a much larger increase in ac impedance when cycled in $LiPF_6$/EC+DMC, so that we may conclude that a thicker surface layer formed in this medium.

Taking the observations in **6-4-1** and **6-4-2** into account, it is suggested that some dissolution of manganese oxide may occur resulting in the capacity fade in the $LiClO_4$/PC electrolyte observed in Fig 6-3-3 (marked with □) while the formation and growth of a surface layer in the electrolyte of $LiPF_6$/EC+DMC may be critical to capacity retention on cycling (see Fig 6-3-7).

6-4-3-2 Other factors relative to the use of $LiPF_6$ based electrolytes

Since the electrolyte of $LiPF_6$ in EC and DMC is recognised as the best candidate for use in practical lithium ion batteries, it is important to investigate this electrolyte solution in detail to understand the factors responsible for promoting the formation and growth of the surface layer. It has been discussed in **6-3-4** that when sMn600 cathode is cycled in this electrolyte, the cyclability of cathode depends on the end of charge voltage. From ac impedance measurements, it is found that the increase in the impedance is also dependant on the cut-off voltage, the higher the charge voltage, the bigger the expansion. Fig 6-4-5, in which the cell was cycled between 4.7 V and 3.3 V for 50 cycles and then subjected to ac impedance measurement, makes the point clear. The impedance after 50 cycles is similar to the value after 100 cycles at the

lower cut-off voltage. The correlation between arc size and charge voltage implies that the formation of surface film involves some by-product during charge.

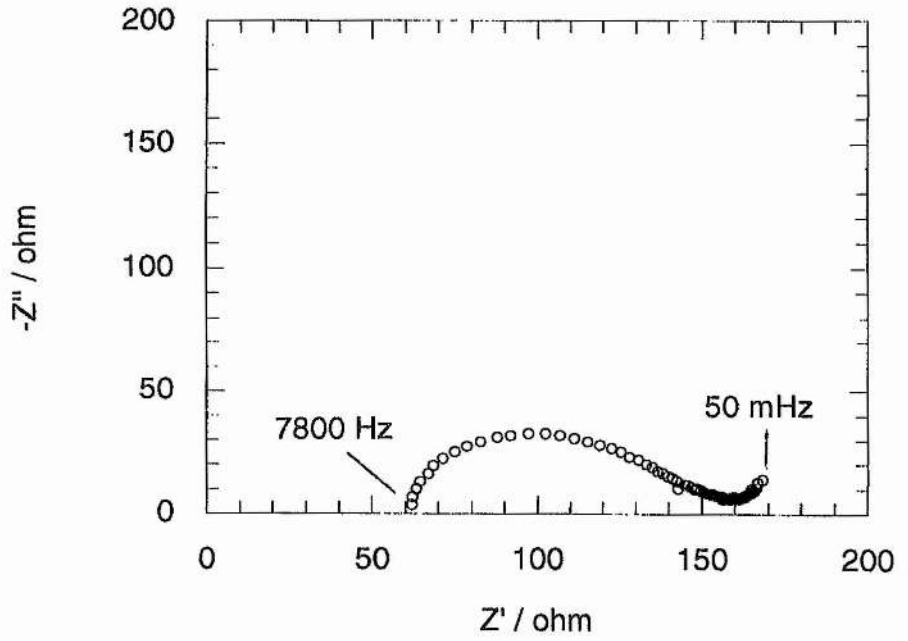

Fig 6-4-5 Ac impedance spectrum for a sMn600 cathode after 50 cycles in $LiPF_6$/EC+DMC electrolyte and with voltage limits of 4.7 V and 3.3 V and at a current density of 1 $mA \cdot cm^{-2}$ for discharging and a current density of 0.5 $mA \cdot cm^{-2}$ for charging.

Since layers appearing on electrodes should exhibit a time dependant impedance. A cell which had undergone 100 cycles was subjected to ac impedance measurements at different intervals of time on open circuit. The results are presented in Fig 6-4-6. The semicircle changed little on standing at open circuit from 12 hours to 7 days , but after this period the semicircle increased in size up to 25 days. This may indicate that the formation and growth of a surface layer also arise from other processes which develop slowly. At present, the nature of the chemical reaction between electrolyte and the cathode is unknown. One possibility is that the evaporation of electrolytes may occur. This is more likely in EC+DMC than in PC considering the volatility of DMC (boiling point: 90 ^{o}C).

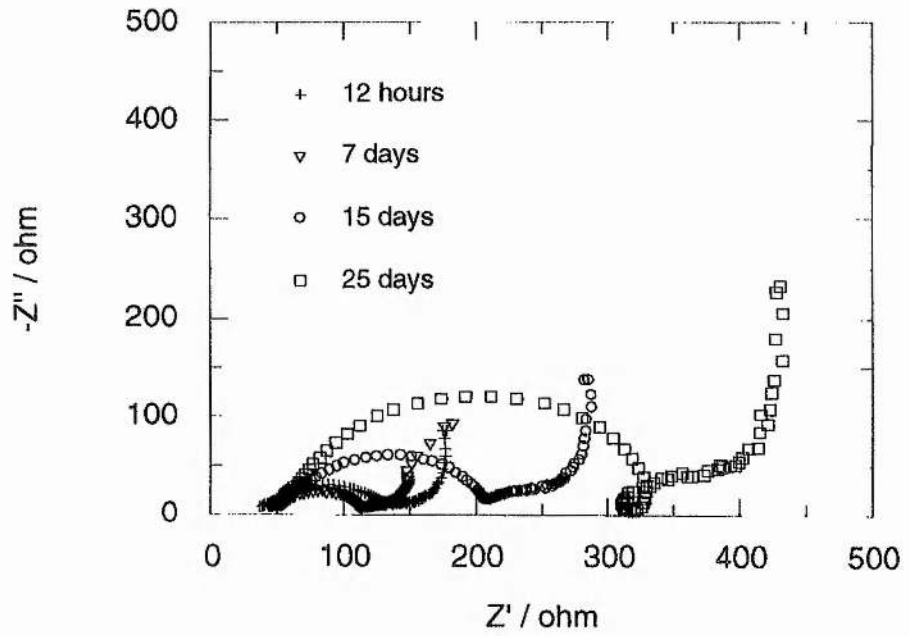

Fig 6-4-6 Ac impedance spectra for the sMn600 cathode in Fig 6-4-3 (100 cycles with 4.3 V - 3.1 V cutoffs) after standing on open circuit for 12 hours (+), 7 days (x), 15 days (○) and 25 days (□). (Frequency range: $6.5x10^3$-0.05 Hz).

A further interesting feature of the EC+DMC system is that the impedance exhibits blocking behaviour at lower frequency (see Fig 6-4-6). This is consistant with a surface layer that is not just an ionically conducting material but is also an intercalation compound. The model would have to involve a 2 layers structure, the outer being an electrolyte and the inner a modified form of the parent material. Finite length diffusion in a thin intercalation electrode layer is known to give vertical impedance spikes [29]. A different interpretation is also possible. There is evidence for the formation of a film on the surface of the Al substrate which may be in part responsible for the stabillity of the $LiPF_6$ in EC/DMC electrolytes at high voltage [30]. The appearance of the vertical line may arise from the passivation of this Al surface. The passivating film may be detrimental to electron flow between the external circuit and the composite electrode. The composition of the $LiPF_6$ based electrolyte including the EC to DMC ratio as well as the purity of $LiPF_6$ salt should be considered to order to improve the surface properties of the Al substrate.

From the above discussions, the possible mechanics for the layer formation in the $LiPF_6$/EC+DMC electrolyte may involve some by-product of cycling, chemical reaction between the electrolyte and electrode materials and the evaporation of liquid electrolyte as well. However, it has yet to be determine which of them is dominant. In particular possible chemical reaction between electrolyte and cathode material is unaware, and it is also necessary to know if the passivating layer on the surface of aluminium plays a role to cause cathode performance declining.

6-5 Conclusions

The lithium manganese oxide spinel prepared by solution synthesis and fired at 600 ^oC is a promising cathode material for use in 4 V rechargeable lithium batteries. In 1 M $LiClO_4$ in PC, the composite cathode based on this 600 ^oC spinel possesses 115 $mAhg^{-1}$ of capacity and retains 75 % of capacity after 300 cycles at a high discharge rate of C/2. In 1 M $LiPF_6$/EC and DMC (1:1 by volume), an initial capacity of 130 $mAhg^{-1}$ is obtainable from the spinel base cathode under similar cycling conditions, but the cut-off potentials are critical to cathode cyclability. Once replacing $LiClO_4$/PC electrolyte with the $LiPF_6$ based electrolyte, at least 5 % enhancement in capacity is achieved over the first 100 cycles under a charge cut-off voltage of 4.3 V. The main reasons for the capacity fade of this spinel cathode differ in the two electrolytes. For the $LiClO_4$/PC electrolyte, manganese oxide dissolution may be a critical factor; for the $LiPF_6$/EC+DMC electrolyte, surface-layer formation and growth with cycling may result in capacity fade. Therefore, it may be concluded that a high cycle life of cathode relies on the electrolyte composition and the quality of $LiPF_6$, particularly in water content. Obviously, future work should seek an optimised electrolyte composition and further investigate with these new electrolyte compositions and highly pure electrolyte solutions the best choice of the charging cut-off potential to maximise the performance of the solution based spinel material. We have also seen the possible deleterious effect of surface layer formation on the Al substrate.

References

[1] T.Nagaura, 4th International Rechargeable Lithium Battery Seminar, Deerfield Beach, FL, USA (1990).

[2] M.M.Thackeray, W.I.F.David, P.G.Bruce, and J.B.Goodenough, Mater. Res. Bull., **18** 461 (1983).

[3] J.B.Goodenough, M.M.Thackeray, W.I.F.David, and P.G.Bruce, Revue de chimie Minérale, 21 435 (1984).

[4] M.M.Thackeray, P.J.Johnson, L.A. de Picciotto, W.I.F.David, P.G.Bruce, and J.B.Goodenough, Mater. Res. Bull., **19** 179 (1984).

[5] J.C.Hunter, and F.B.Tudron, Proc. Electrochem. Soc., **P1-3** 444 (1991).

[6] K.Brandt, Solid State Ionics, **69** 173 (1994).

[7] D. Guyomard, and J.M.Tarascon, Solid State Ionics, **69** 222 (1994)

[8] J.M.Tarascon, W.R.McKinnon, F.Coowar, T.N.Bowmer, G.Amatucci, and D.Guyomard, J. Electrochem. Soc., **141** 1421 (1994).

[9] J.M.Tarascon, W.R.McKinnon, F.Coowar, G.Amatucci, F.K.Shokoohi, and D.Guyomard, Extended Abstracts, 7th International Meeting on Lithium Batteries, 113, (1994).

[10] J.M.Tarascon, D.Gyomard, and G.L.Baker, J. Power Sources, **43** 689 (1993).

[11] J.M.Tarascon, and D.Guyomard, Electrochimica Acta, **38** 1221(1993).

[12] D.Guyomard, and J.M.Tarascon, J. Electrochem. Soc., **139** 937 (1992).

[13] D.Guyomard, and J.M.Tarascon, Proc. Electrochem. Soc., **P2-15** 113 (1992).

[14] J.M.Tarascon, E.Wang, F.K.Shokoohi, W.R.McKinnon, and S.Colson, J. Electrochem. Sco., **138** 2859 (1991).

[15] J.M.Tarascon, and D.Guyomard, J. Electrochem. Soc., **138** 2864 (1991).

[16] F.K.Shokoohi, J.M.Tarascon, B.J.Wilkens, D.Guyomard, and C.C.Chang, J. Electrochem. Soc., **139** 1845 (1992).

[17] F.K.Shokoohi, J.M.Tarascon, B.J.Wilkens, Appl. Phys. Lett., **59** 1260 (1991).

[18] P.Barboux, J.M.Tarascon, and F.K.Shokoohi, J. Solid state Chem., **94** 185 (1991).

[19] J.M.Tarascon, and D.Guyomard, Solid State Ionics, **69** 293 (1994).

[20] D.Guyomard, and J.M.Tarascon, J. Electrochem. Soc., **140** 3071 (1993).

[21] V.Manev, A.Momchilov, A.Nassalevska, and Atsushi Sato, J. Power Sources, **54** 323 (1995).

[22] A.Momchilov, V.Manev, A.Nassalevska, and A.Kozawa, J. Power Sources, **41** 305 (1993).

[23] V.Manev, A.Momchilov, A.Nassalevska, and A.Kozawa, J. Power Sources, **43-44** 551 (1993).

[24] Haitao Huang, and Peter G.Bruce, J. Power sources, **54** 52 (1995).

[25] Y.Gao and J.R.Dahn, J. Electrochem. Soc., **143** 100 (1996).

[26] M.G.S.R.Thomas, P.G.Bruce, and J.B.Goodenough, J. Electrochem. Soc., **132** 1521 (1985).

[27] A.J.Bard, and L.R.Faulkner, Electrochemical Methods Principles and Experimental, John Wiley & Sons, (1980).

[28] Southampton Electrochemistry Group, Instrumental Methode in Electrochemistry, Ellis Horwood, (1990).

[29] C.Ho, I.D.Raistrick, and R.A.Huggins, J. Electrochem. Soc., **127** 343 (1980).

[30] K.Kanamura, T.Okagawa, Zen-ichiro Takehara, J. Power Sources, **57** 119 (1995).

CHAPTER SEVEN

Electrochemical Studies of the Lithium Manganese Oxide Spinel $LiMn_2O_{4.1}$ for 3 V Lithium Batteries

7-1 Introduction

The abundance of 3 volt cathode materials is much greater than 4 volt materials. The former have the advantage of placing less stringent requirement on the stability of organic electrolytes to oxidation. The 3 volt cathode is able to utilise in full the present battery and electrolyte technologies that have been developed over many years. Therefore, this battery system still attracts considerable interest.

Most of the 3 volt materials of interest are based on manganese or vanadium oxides [1-4]. However, those based on manganese oxides have an advantage over the vanadium oxides, due to their lower toxicity. Lithium manganese oxides which have already been investigated as 3 volt cathodes include the spinel $LiMn_2O_4$ [5-9] and other spinel-related materials, e.g. $Li_2Mn_4O_9$ [10-15] and $Li_4Mn_5O_{12}$ [11-15], as well as CDMO which consists of a mixture of $\gamma/\beta MnO_2$ and lithiated spinel [14, 16-18].

It is useful to summarise briefly the performance of the various 3 volt manganese oxides before discussing the performance of our new spinel material. CDMO is prepared by reacting manganese dioxide (MnO_2) with either LiOH, Li_2CO_3 or $LiNO_3$ at a temperature lower than 400 °C [16, 17]. The manganese valence in CDMO is more than +3.8 [17], and as a result its theoretical specific capacity is able to reach 300 $mAhg^{-1}$. Over 200 $mAhg^{-1}$ of practical capacity was reported by Norhma *et al.* [16]. With regard to cycling life, CDMO was reported to be superior to $LiMn_2O_4$ spinel at a discharge depth of 0.26 e/Mn [18]. This is believed to arise from the fact

that the intercalation process is associated with a one-phase reaction in CDMO while a two-phase reaction takes place in the spinel [18]. However, the discharge depth of 0.26 e/Mn represents only a small fraction of the capacity utilised in a practical rechargeable battery

The spinel-related materials, $Li_2Mn_4O_9$ and $Li_4Mn_5O_{12}$, are prepared by solid state reaction between $MnCO_3$ and Li_2CO_3 at 400 °C [10, 13]. Table 7-1-1 compares the theoretical capacities of various spinel and spinel related manganese oxides. Although λ-MnO_2 has the highest capacity (308 $mAhg^{-1}$), the practical use of this oxide as a cathode material has to be limited to 148 $mAhg^{-1}$ because of the two well separated potential plateaux at 3V and 4V in the course of discharging to $Li_2Mn_2O_4$ and so a practical cell has to be confined to either of them. This is not the case for $Li_2Mn_4O_9$ which delivers its capacity at 3 V and is therefore the best manganese oxide in term of theoretical capacity. Thackeray *et al.* reported that the practical capacity of $Li_2Mn_4O_9$ is 165 $mAhg^{-1}$ and that of $Li_4Mn_5O_{12}$ is 150 $mAhg^{-1}$ [14]. Regarding cyclability, a test with 20 cycles showed that improved capacity retention was obtained from the two spinel-related materials in comparison to $LiMn_2O_4$ prepared by high temperature solid state reaction, arising from the fact that on lithium intercalation into $Li_2Mn_4O_9$ and $Li_4Mn_5O_{12}$ the Jahn-Teller distortion only occurs at relatively high lithium ion content compared with the specific $LiMn_2O_4$ spinel [13]. However, no long-term cycling of the two materials has been reported to date. From a very recent paper [20] on $Li_4Mn_5O_{12}$, one can see that it is hard to prepare high purity $Li_2Mn_4O_9$ and $Li_4Mn_5O_{12}$ materials. In practice impure materials can not retain high performance over long term cycling.

It is important to point out that the $LiMn_2O_4$ phase mentioned above was prepared by conventional high temperature solid-state reaction and is thus highly stoichiometric. It has already been recognised that highly crystalline and stoichiometric spinel does not yield good cycling performance in either 4 V or 3V lithium batteries [19, 8]. To obtain a high capacity at 3 volt it is important to prepare a spinel with as high a

concentration of Mn^{4+} as possible. $Li_2Mn_4O_9$ and $Li_4Mn_5O_{12}$ both contain only Mn^{4+}, also they are defect spinels, the former having the ion / vacancies distribution $(Li_{0.89}\square_{0.11})_{8a}[Mn_{1.78}\square_{0.22}]_{16d}O_4$, and the latter $(Li)_{8a}[Mn_{1.66}Li_{0.33}]_{16d}O_4$ [15]. In searching for other 3 volt spinel similar characteristics may be sought.

Table 7-1-1: Mn valency and electrode capacities of spinel-related oxides.

Composition of spinel phase	Average Mn valency	Theoretical capacity ($mAhg^{-1}$)
λ-MnO_2	4.00	308
$Li_2Mn_4O_9$	4.00	213
$Li_4Mn_5O_{12}$	4.00	163
$LiMn_2O_4$	3.50	148
Mn_3O_4	2.67	117

CHAPTER FIVE described the synthesis of a new lithium manganese oxide spinel, $LiMn_2O_{4.1}$, which has a higher proportion of Mn^{4+} to Mn^{3+} compared with the stoichiometric spinel and may have a defect structure as $(Li_{0.98}\square_{0.02})_{8a}[Mn_{1.95}\square_{0.05}]_{16d}O_4$. The compound was obtained by heating at 200 °C. Although it does not perform well in 4 volts cells due in part to the lower theoretical capacity at this potential as discussed in CHAPTER SIX, this chapter will discuss the excellent performance of this oxygen-rich spinel ($LiMn_2O_{4.1}$.) as a 3 volts cathode, particularly a remarkable enhancement of cyclability by the addition of carbon during synthesis. Cells based on this spinel cathode were cycled at a relatively high discharge rate C/2 for 300 cycles and show high practical capacity and cyclability compared with spinels prepared by other methods such as conventional high temperature solid state reaction and sol-gel [21, 22]. When the $LiMn_2O_{4.1}$ spinel is cycled in the 3 V region and compared with cycling of the other solution based spinel in the 4 V region (for discussion of this other spinel see CHAPTER SIX), the

former is found to exhibit a much greater capacity fade. This has been attributed to the existence of the cubic to tetragonal phase transition on cycling at 3 volts. An important aspect of this chapter concerns X-ray studies made on the 3 V spinel cathodes ($LiMn_2O_{4.1}$) during cycling to ascertain the origin of the greater capacity fade.

7-2 Performance of $LiMn_2O_{4.1}$ spinels

The following describes the investigation of the cycling performance of $LiMn_2O_{4.1}$ for use in 3 volt lithium cells and further improvement of performance by adding carbon during synthesis of this material. In all cases a three electrode cell was used and both counter and reference electrodes were made from lithium metal. The spinel materials were mixed with carbon black and PTFE powder in ratios as 80:13:7 to fabricate a composite electrode as working electrode. The electrolyte was 1 M $LiAsF_6$ in PC. (The details of the structure of three electrode cell and the fabrication of composite cathodes refer to CHARTER THREE.)

7-2-1 Practical capacity and charge-discharge behaviour

The lithium manganese oxide spinel prepared by solution synthesis but without carbon and fired at 200 °C (denoted as sMn200) was fabricated into a composite electrode and then discharged, in a three electrode cell, intermittently to 2.0 V at 0.2 $mA \cdot cm^{-2}$. The discharge process involved 8 hours on load and 12 hours on open circuit. A discharge capacity of 178 $mAhg^{-1}$ was obtained. As a comparison, a similar test was performed but using the spinel formed by solid state reaction at 850 °C (denoted as ssMn850), in this case a capacity of only 142 $mAhg^{-1}$ was obtained. The value of 178 $mAhg^{-1}$ is much higher than the theoretical specific capacity of 148 $mAhg^{-1}$ expected for the stoichiometric spinel $LiMn_2O_4$ (see Table 6-2-1), but very close to the value of 176 $mAhg^{-1}$ which is expected for $LiMn_2O_{4.1}$ based on its

valency i.e. +3.6. If the capacity limit was determined by the amount of lithium required to fully occupy the octahedral 16c sites then a specific capacity of 150 $mAhg^{-1}$ would be expected. Instead the limit is completed reduction of all Mn^{4+} to Mn^{3+}. This corresponds to more lithium than would be accommodated in the rock salt structure (i.e. all lithium ions are in 16c sites). Lithium ions must occupy simultaneously 8a site and face sharing 16c sites.

Besides the increase in capacity, the solution based spinel exhibits some change in its charge and discharge curves. A composite electrode based on the spinel prepared by solution synthesis was subjected to cycling in a three electrode cell at a current density of 0.25 $mA \cdot cm^{-2}$ between 3.7 V and 2.0 V. Fig 7-2-1 (a) shows that discharge and charge behaviour is identical between the first and subsequent cycles. However, a different situation was observed in the case of the composite electrode containing ssMn850 spinel (Fig 7-2-1 (b)). The ssMn850 electrode exhibits two discharge plateaux but only during the first discharge and the potential of the discharge plateau increases after the first cycle. The cyclic voltammogram at a scan rate of 0.2 $mV \cdot s^{-1}$ for the ssMn850 spinel shows two broad and short peaks appearing in the first cathodic sweep (Fig 7-2-2). This appears to correspond with the two plateaux observed in the first galvaniostatic discharge. However, there are no double peaks in the first cathodic reduction when a slow scan rate, e.g. 10 $\mu V \cdot s^{-1}$, is applied. Instead the reduction peak is much broader during the first cycle than in subsequent cycles. The fact that more peaks are evident on the fast sweep indicates that this is not due to the kinetics of the intercalation process, instead some irreversible change must occur on the first cycle at high rate of intercalation. This may be due to displacement of Li^+ from tetrahedral to octahedral sites during the this cycle. This kind of discharge behaviour, i.e. differing in the first cycle, has already been reported for other intercalation materials and attributed to some structure rearrangement [23]. In contrast to the ssMn850 spinel, the sMn200 spinel always exhibits a single reduction peak in its cyclic voltammograms for the first and following cycles whether the scan rate is fast or slow. It has been suggested that a difference in crystallinity may influence the

electrochemical behaviour of intercalation hosts and the comparison between amorphous and crystalline LiV_3O_8 was used as an example [24]. The oxygen-rich spinel may exhibit less of a change between the first and subsequent cycles because the particles are already small and are not subjected to strain and particle break up to the some extent as the high temperature material. Finally, it is interesting to note that the charge and discharge potentials of the solution based spinel are somewhat lower than those of the spinel prepared by solid state reaction. This may be consistent with the suggestion above that there are lithium ions in 8a and face sharing 16c sites leading to stronger Li^+-Li^+ repulsion than would be the case for Li^+ ions in 16c site only.

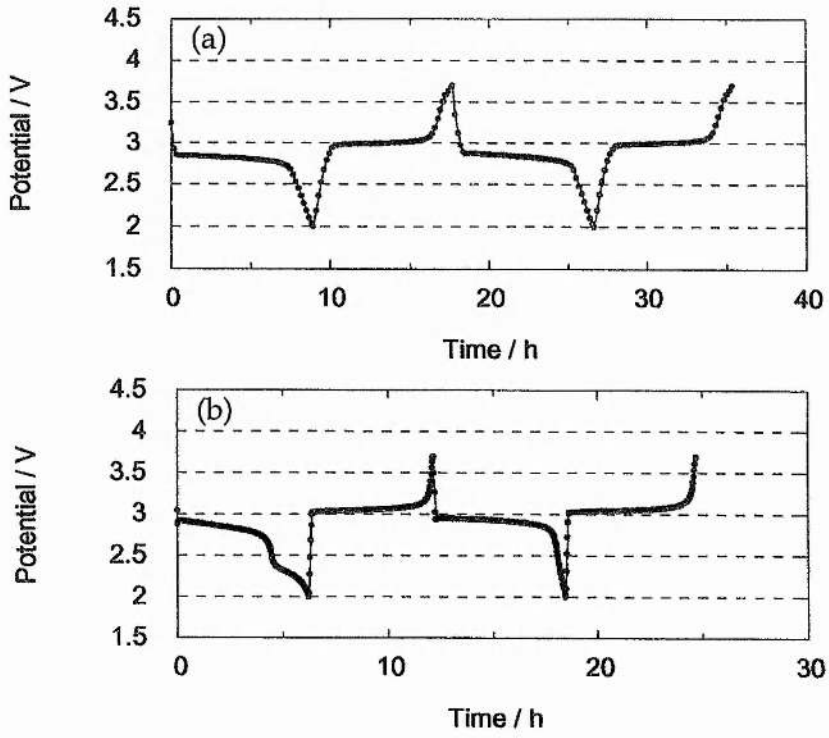

Fig 7-2-1 The first and second charge-discharge curves: (a) sMn200 and (b) ssMn850 composite cathodes; in 1 M $LiAsF_6$/PC and at 0.25 $mA \cdot cm^{-2}$.

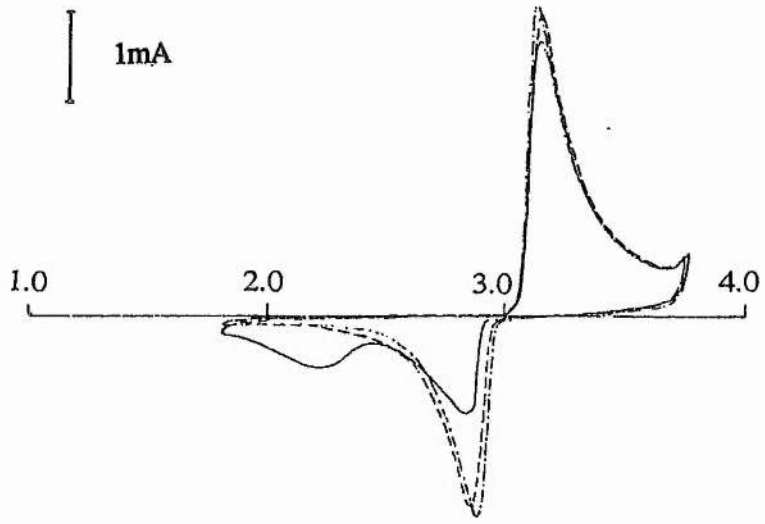

Fig 7-2-2 The cyclic voltammogram for a ssMn850 electrode in 1 M $LiAsF_6$/PC at a scan rate of 0.2 $mV \cdot sec^{-1}$.

7-2-2 Improvements by the addition of carbon during synthesis

As far as the author is aware, no work has been reported on the improvement of performance when carbon is added during the synthesis of an intercalation compounds. Based originally on the belief that carbon dispersed during solution synthesis would improve electronic contact between the particles, the preparation of $LiMn_2O_{4.1}$ in the presence of carbon was proposed. In the following sections the performance of $LiMn_2O_{4.1}$ spinel prepared with and without carbon is compared. Results for $LiMn_2O_4$ prepared by conventional solid state synthesis are also included.

7-2-2-1 Amount of carbon used during synthesis

Three spinel powders, containing respectively 1.3, 4.0 and 7.8 wt % of carbon, were prepared by the sol-gel synthesis described in **5-2** and then fabricated into composite cathodes. These electrodes were then subjected to three electrode cycling at a current of 0.49 $mA \cdot cm^{-2}$ between 2.0 V and 3.7 V in 1 M $LiAsF_6$/PC solution for more than

100 cycles. The curves in Fig 7-2-3 present the variation of discharge capacities on the 1st, 32nd, 52nd and 104th cycles with the amount of carbon in each spinel. The carbon content is expressed as a percentage of the total weight of spinel. Also, the cycling results under the same conditions from a sol-gel spinel prepared without carbon are included in the figure for comparison. The specific discharge capacities were based on the weight of the spinel only, i.e., corrected for the weight of the other components of the composite cathodes. Three points are worth noting: (1) the addition of carbon during preparation increases the discharge capacity of the cathode, (2) the optimum amount of carbon is between 1 and 3 wt % of the active material and (3) the broad maximum moves from 1 to 3 % with increasing cycle number.

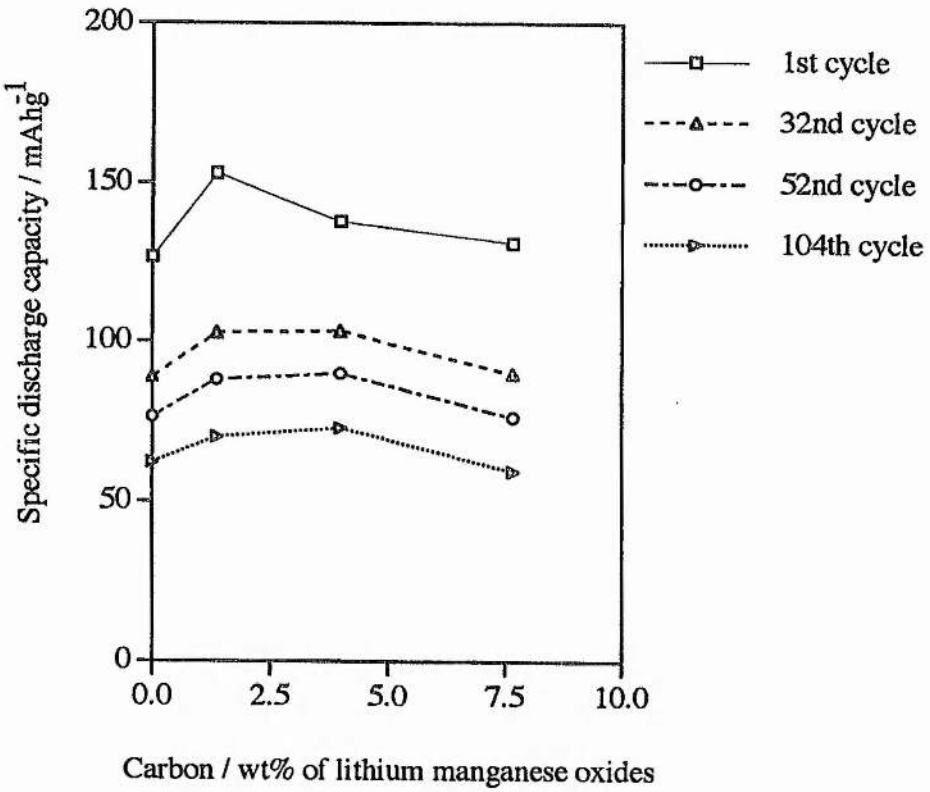

Fig 7-2-3 Influence of the quantity of carbon added during the sol-gel preparation of 3 V lithium manganese oxide on the specific capacity.

The value of 2 % expressed as a percentage of the active material is equivalent to a value of < 1 % expressed in term of the starting materials used to prepare the spinel.

That is < 1 % addition of carbon during the synthesis enhances the capacity of the spinel. The following presents the performance results on the spinels with and without carbon but now prepared by the solution synthesis.

7-2-2-2 Rate capability

In order to evaluate the rate capability of the spinels, a series of three electrode cycling tests at various currents were carried out using the composite cathodes containing the spinels prepared from solution synthesis with and without carbon (i.e. scMn200 and sMn200 respectively) as well as from solid state reaction at 850 °C (ssMn850). Cut-off voltage limits for cycling cells were between 3.7 V and 2.0 V. For discharge current densities of 0.2, 0.25 and 0.5 $mA \cdot cm^{-2}$, the charging currents employed were equal to the discharge currents. However, for cells discharged at 1 $mA \cdot cm^{-2}$, a charging current density of 0.5 $mA \cdot cm^{-2}$ was used. The specific discharge capacities presented in Fig 7-2-4 are an average of the first four cycles in each case. Under this charge and discharge regime an overall trend of linearly declining capacity with increasing discharge current density is clearly seen for all cathode materials. At the high current density of 1 $mA \cdot cm^{-2}$, scMn200 and sMn200 cathodes still deliver high capacities of 148 and 143 $mAhg^{-1}$, respectively, compared with only 81 $mAhg^{-1}$ obtained for the ssMn850 electrode.

7-2-2-3 Cycling life

The retention of capacity of materials prepared at 200 °C with and without carbon was examined. Composite cathodes based on sMn200 and scMn200 were cycled between 3.7 V and 2.0 V, and at relatively high current densities of I_d = 1 $mA \cdot cm^{-2}$ (C/2) and I_c = 0.5 $mA \cdot cm^{-2}$. The specific discharge capacities for each cycle are presented in Fig 7-2-5. In the case of the lithium manganese oxide prepared with carbon (less than 1 wt % of the reagents used in the synthesis), the initial capacity was

in excess of 140 $mAhg^{-1}$ and rises slightly within the first few cycles before falling to 125 $mAhg^{-1}$ at 100 cycles, 100 $mAhg^{-1}$ at 200 cycles, and 90 $mAhg^{-1}$ at 300 cycles. Although the initial cycling behaviour for the material prepared without carbon is very similar to that with carbon, the capacity fade is significantly greater in the absence of carbon. The material prepared with carbon possesses a capacity some 30 $mAhg^{-1}$ greater than the material without carbon at 300 cycles. This corresponds to an enhancement of 50 % indicating the very significant improvement in cycling performance that can be obtained if less than 1 wt. % of carbon is added to the solution during synthesis of the lithium manganese oxide spinel. As a comparison, the inferior cycling result from the material prepared by high temperature solid-state reaction (ssMn850) is also showed in Fig 7-2-5.

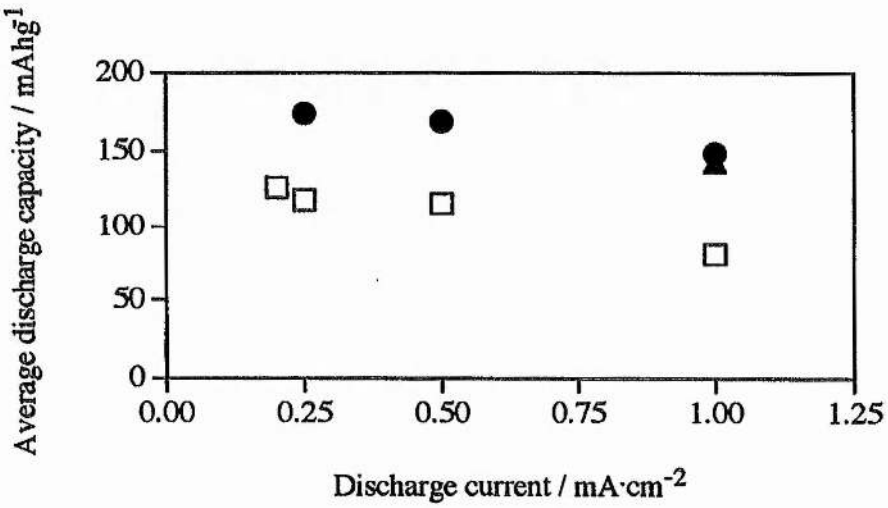

Fig 7-2-4 The variation of initial discharge capacities (averaged over the first four cycles) as a function of discharge current density. The lithium manganese oxide spinels were prepared by a solution route at 200 °C with carbon (●) and without carbon (▲), or prepared by solid state reaction and fired at 850 °C (❑). Cut-off voltage limits were 3.7 V and 2.0 V.

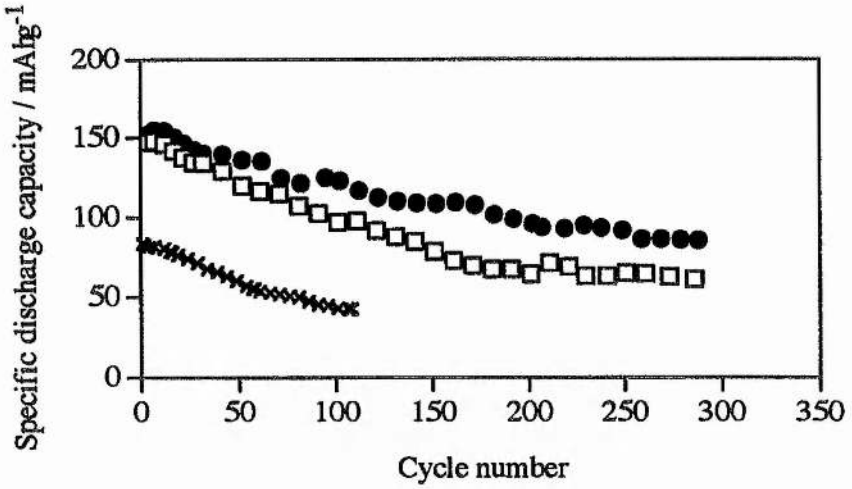

Fig 7-2-5 Evolution of the retention of discharge capacity for scMn200 (●), sMn200 (❑) and ssMn850 (x) electrodes in 1 M $LiAsF_6$/PC with 3.7 V and 2.0 V cutoffs at a discharge current density of 1 $mA \cdot cm^{-2}$ (C/2), and a charging current density of 0.5 $mA \cdot cm^{-2}$.

7-2-3 Comparison of performance with spinels prepared by other syntheses

It is interesting to review the progress that has been made in improving the cycling performance of lithium manganese oxide spinels over recent years. This is summarised in the histogram plot, Fig 7-2-6. This is not exhaustive in that the results from every variant of the synthetic methods have not been included. However it does give an impression of the improvements in performance that have been achieved in moving from high temperature solid-state synthesis to a sol-gel method with and without carbon (sol-gel + C and sol-gel, respectively, in Fig 7-2-6) and then to a solution-based preparation with and without carbon at 300 and 200 °C. The specific discharge capacities presented in this figure are again averaged over the first four cycles although they also reflect the trends at higher cycle number. It is evident from the figure that very substantial improvements in cycling performance have been achieved. At the higher discharge rate of C/2 the capacity has been doubled in changing from the high temperature solid-state synthesis to the solution method at

200 °C with and without carbon. Increasing the discharge rate from C/4 to C/2 severely diminishes the capacity of the solid-state material whereas the material prepared from solution with carbon at 200 °C possesses a capacity which is much less sensitive to discharge rate. The improvement in performance obtained by reducing the firing temperature from 300 °C to 200 °C for the material prepared by the solution route is evident. This is mainly due to the increase in oxidation state upon firing at a lower temperature.

As is evident from the above results, the lithium manganese oxide spinel $LiMn_2O_{4.1}$, prepared by the low-temperature (200 °C) solution synthesis with carbon, exhibits the best performance obtained so far for a 3 volt lithium manganese oxide spinel.

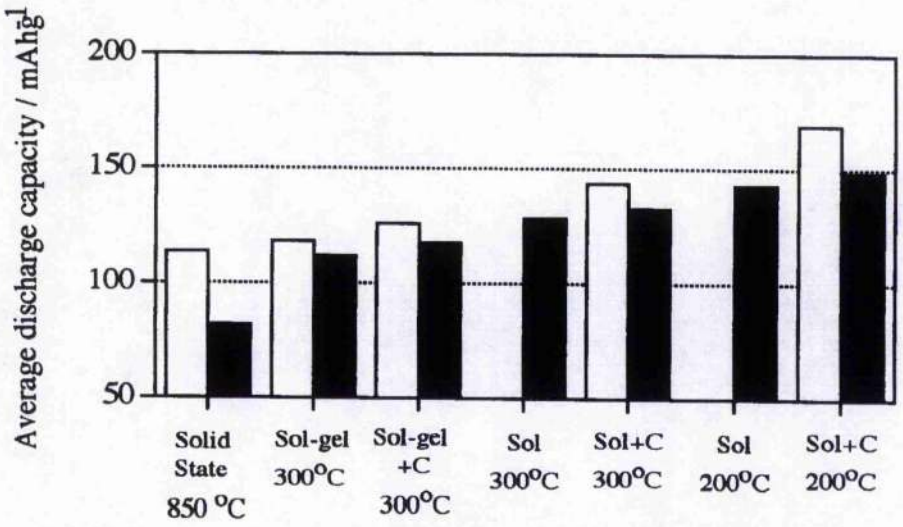

Fig 7-2-6 Histogram plot comparing the cycling performance of several 3 V composite cathodes containing lithium manganese oxide spinels prepared under different conditions. The composite cathodes and cycling conditions were identical in all cases, the only difference being the active material. The specific discharge capacities are an average taken over the first four cycles. The charge rate is C/4 and the discharge rate are (❑) C/4 and (■) C/2.

7-3 A study of cathode cycle life by X-ray diffraction

Despite the fact that our 3 volt material with carbon offers a substantial improvement in performance compared with some other synthetic routes, the capacity fade apparent in 3 V cells (Fig 7-2-4) is still worse than that of 4 V cells (Fig 6-3-3). It is known that lithium intercalation into $LiMn_2O_4$ involves a two phase reaction due to the cooperative Jahn-Taller effect [5-7]. As lithium is inserted, the tetragonal phase grows at the expense of the cubic phase. X-ray diffraction is capable of following this change and this technique was therefore used to investigate the influence of the cubic-tetragonal phases transition on the cyclability of the 3 volt material. The X-ray diffraction study also attempts to understand the effect of the carbon added during the synthesis on cycle performance.

7-3-1 Ex situ measurements

To date the combined use of X-ray diffraction and electrochemical studies on intercalation compounds has been restricted to the determination of structural changes accompanying intercalation/deintercalation [25-30]. Two approaches are possible, either *in situ* or *ex situ*.. There are, of course, advantages in using the *in situ* technique, in particular structural changes can be continuously monitored and there is no possibility of the electrode being disturbed (for example, loss of power) on transferring into or out of the diffractometer. Furthermore, the *in situ* technique will detect phases which may not be stable on removal of the electrode from the electrochemical environment [31]. *In situ* X-ray studies of intercalation electrode cells have been carried out in both reflection and transmission mode. The latter in particular has been extensively used in recent years by the group in Sweden for the study of cathodes based on V_6O_{13} [29]. One particular problem with this technique is the relatively high background encountered due to the current collector on the anode

and, to a lesser extent, the electrolyte, both of which are also in the X-ray beam. Manganese fluoresces significantly with copper radiation and our in-house Stoe Transmission Diffractometer is only equipped with a position sensitive detector and therefore no means of removing the fluorescence by monochromation as is commonly carried out with scintillation detectors. We were therefore restricted to use of a reflection geometry instrument used *ex situ*.

A composite electrode without an Al gauze substrate was used for the *ex situ* X-ray diffraction experiments. The weight ratios in the composite electrode were manganese spinel (80 %):carbon black (13 %):PTFE (7 %). The presence of the PTFE resulted in the formation of a film simply by grinding the mixture in an agate mortar and pestle. Each composite film weighed 53 mg in total and contained an area of approximately 2 cm^2. The composite film was subjected to X-ray diffraction measurements using a Philips diffractometer operating with CuK_α radiation both before and after galvanostatically cycling in a two electrode cell (Fig 3-4-2). In order to prevent any possible reaction of discharged spinel with air and moisture, the composite film was sandwiched between two Mylar X-ray transparent films and sealed with tape, the assembly is shown schematically in Fig 7-3-1. The absence of aluminium gauze avoided additional XRD peaks in the pattern.

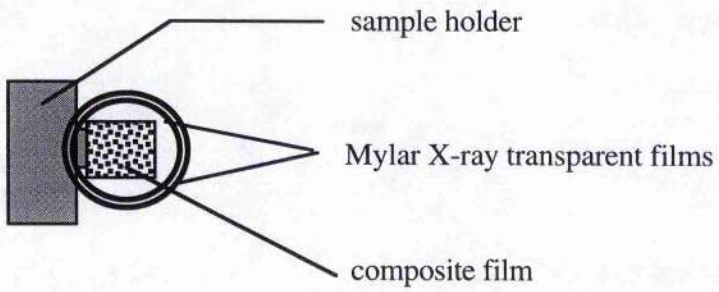

Fig 7-3-1 A diagram showing the sample mounting for an ex-situ X-ray diffraction experiment.

7-3-2. XRD patterns with discharge depth

A two electrode cell, containing the composite electrode and an electrolyte composed of 1 M $LiAsF_6$ in PC, was intermittently discharging at 75 $\mu A \cdot cm^{-2}$ (C/41). The spinel used in the composite electrode was prepared by solid state reaction at 850 °C (ssMn850) and X-ray diffraction patterns were taken at various stages of intercalation i.e. depth of discharge and the electrode then returned to the cell. Fig 7-3-2 clearly shows the cubic to tetragonal phase change on discharge. The patterns in Fig 7-3-2 (a) and (d) are representative of two extreme cases: a cubic phase and an almost pure tetragonal phase [32], corresponding to the undischarged spinel (x = 0) and the almost fully discharged spinel (x = 0.94), respectively. The different patterns in Fig 7-3-2 (b) and (c) are a mixture of cubic and tetragonal phases, corresponding to partial discharging (x = 0.1 and 0.6). For convenience, the main diffraction peaks for the cubic phase (Fig 7-3-2 (a)) and the tetragonal phase (Fig 7-3-2(d)) are listed in Table 7-3-1.

Table 7-3-1 Main diffraction peaks for cubic and tetragonal spinel obtained from Fig 7-3-2 (a) and (d).

cubic phase	2θ	18.6°		36.2°			44.0 °
	hkl	111		311			400
tetragonal phase	2θ	18.2°	33.0°	36.8°	37.2°	38.8°	45.2°
	hkl	101	103	211	202	004	220

7-3-3 Structure change on cycling

A composite cathode containing the spinel prepared by solid state reaction at 850 °C (i.e. ssMn850) was discharged and charged galvanostatically and then subjected to *ex situ* X-ray diffraction. An initial discharge to 2.0 V at a current of 0.25 $mA \cdot cm^{-2}$ (C/12) yielded a capacity of only 96 $mAhg^{-1}$, much lower than the theoretical value of 148 $mAhg^{-1}$. Corresponding to this, the diffraction pattern at the end of the discharge exhibited two phases, cubic and tetragonal (Fig 7-3-3 (a)). On charging the

electrode to 3.7 V at the same current, the tetragonal phase disappeared completely leaving only the cubic spinel (Fig 7-3-3 (b)). The electrode was then subjected to 50 cycles at a higher current of 0.75 $mA \cdot cm^{-2}$ (C/4) between 3.7 V and 2.0 V, this was followed by one cycle at the same low current of 0.25 $mA \cdot cm^{-2}$ (C/12) as before. *Ex situ* X-ray diffraction was carried out on this electrode at the end of discharge again and indicated the co-existence of the tetragonal and cubic phases (Fig 7-3-3 (c)). However, the proportion of the cubic phase remaining at the end of discharge after 50 cycles (Fig 7-3-3 (c)) is much greater than before cycling (Fig 7-3-3 (a)). On recharging after 50 cycles it is evident of a very small amount of residual tetragonal phase (Fig 7-3-3 (d).

Composite electrodes containing the spinels prepared by solution synthesis at 200 ^{o}C with carbon (scMn200) and without carbon (sMn200) were tested under the same experiment conditions as the ssMn850 electrode above. After the first discharge at the lower current, both electrodes exhibited a single phase product (Fig 7-3-4 (a) and Fig 7-3-5 (a)), the powder patterns being identical to the tetragonal pattern in Fig 7-3-2 (d) although the peaks are broad and the 211 and 202 reflections overlap each other. The discharge capacities of the scMn200 and sMn200 electrodes were respectively 173 and 155 $mAhg^{-1}$, which are close to their theoretical value of 176 $mAhg^{-1}$. Again in contrast to the ssMn850 electrode (Fig 7-3-3 (c)), the scMn200 and sMn200 electrodes yielded a single tetragonal phase on discharging after 50 cycles (Fig 7-3-4 (c), Fig 7-3-5 (c)).

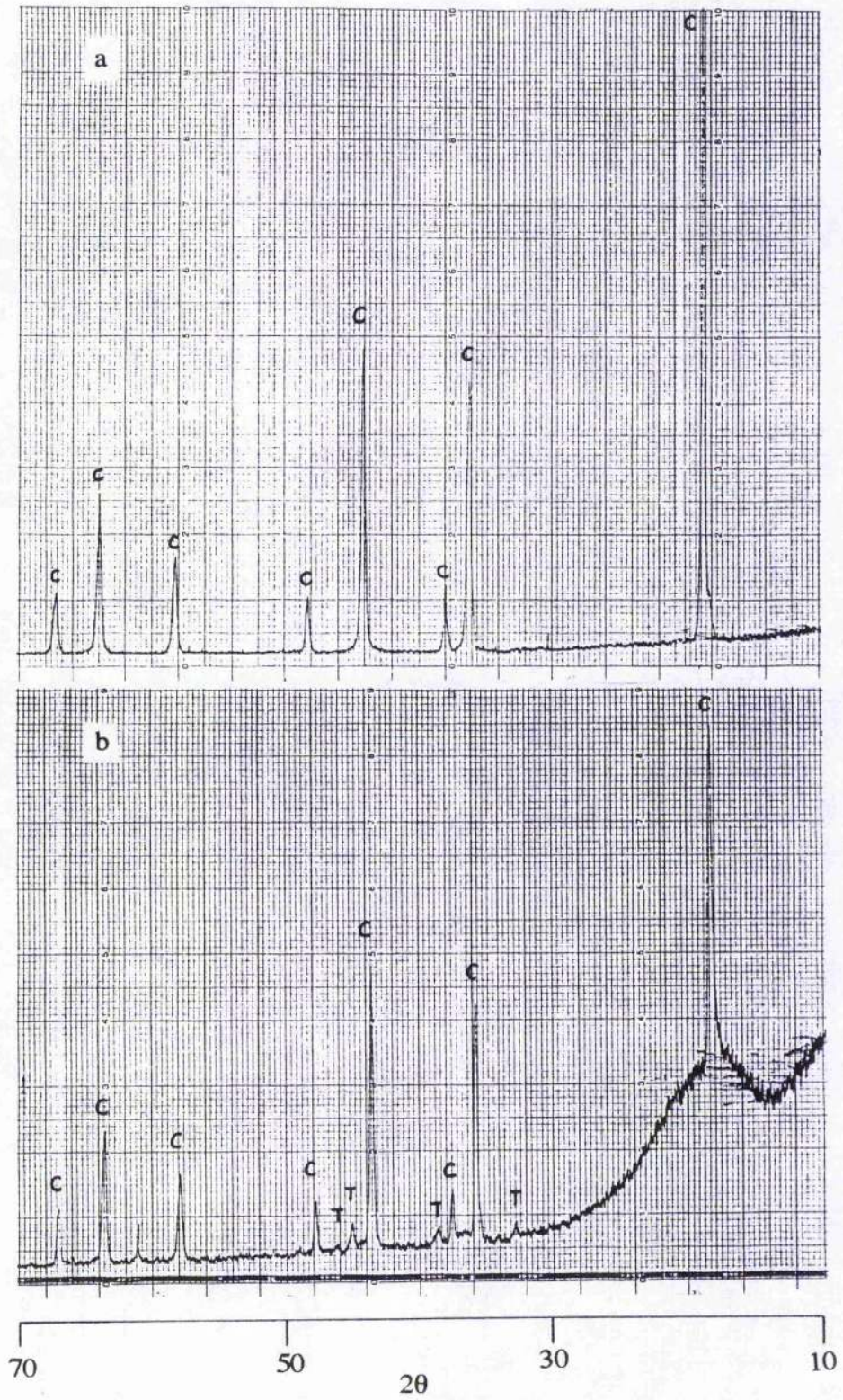

Fig 7-3-2 XRD patterns for $Li_{1+x}Mn_2O_4$ at different composites: (a) x = 0, (b) x = 0.1. The peaks denoted by C are attributed to the cubic phase, and the peaks denoted by T are attributed to the tetragonal phase. The very broad background peak at low angles (< 30° in 2θ) arises from the tape used to seal the sample from the atmosphere.

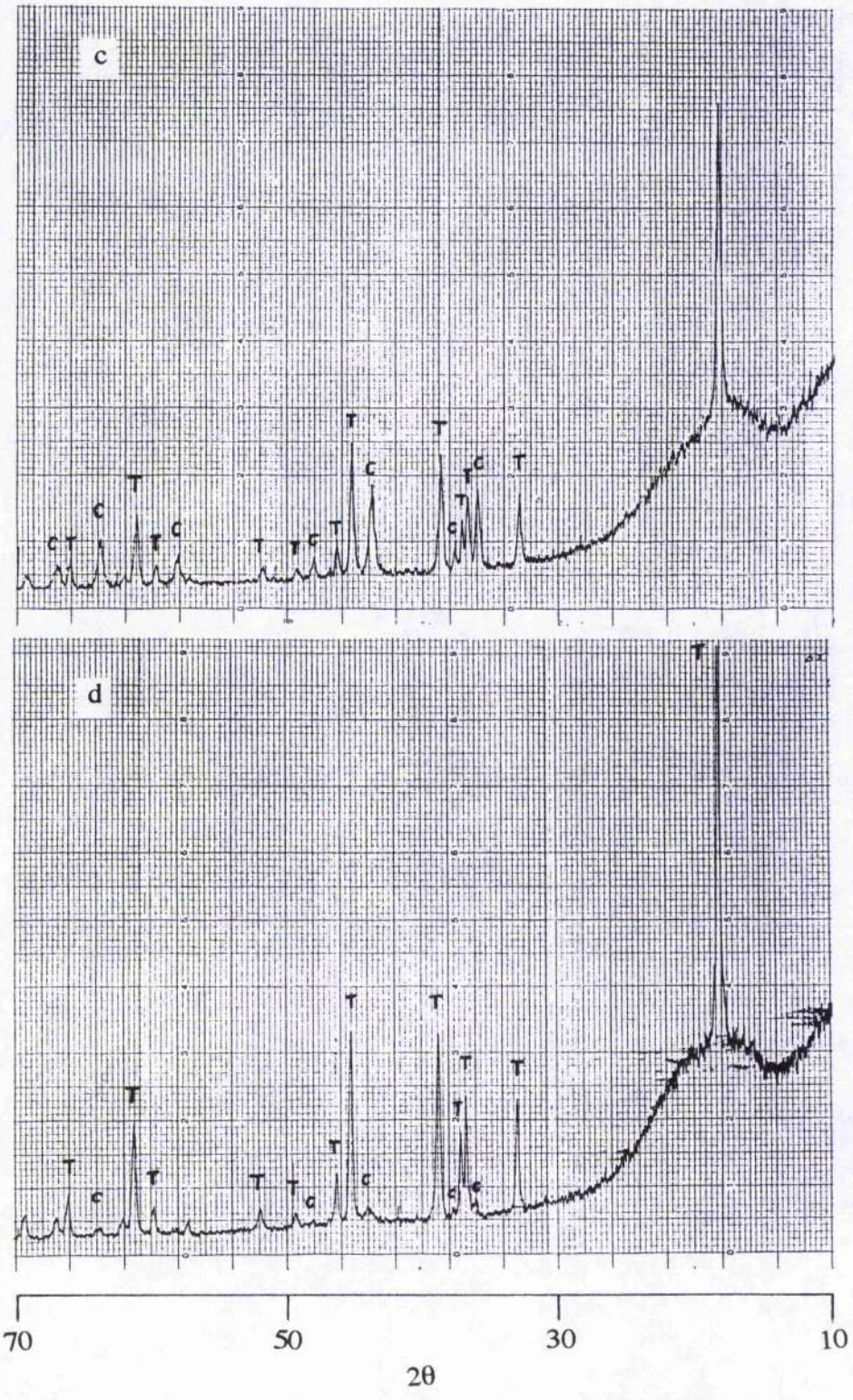

Fig 7-3-2 XRD patterns for $Li_{1+x}Mn_2O_4$ at different composites: (c) x = 0.6, (d) x = 0.94. The peaks denoted by C are attributed to the cubic phase, and the peaks denoted by T are attributed to the tetragonal phase. The very broad background peak at low angles (< 30° in 2θ) arises from the tape used to seal the sample from the atmosphere.

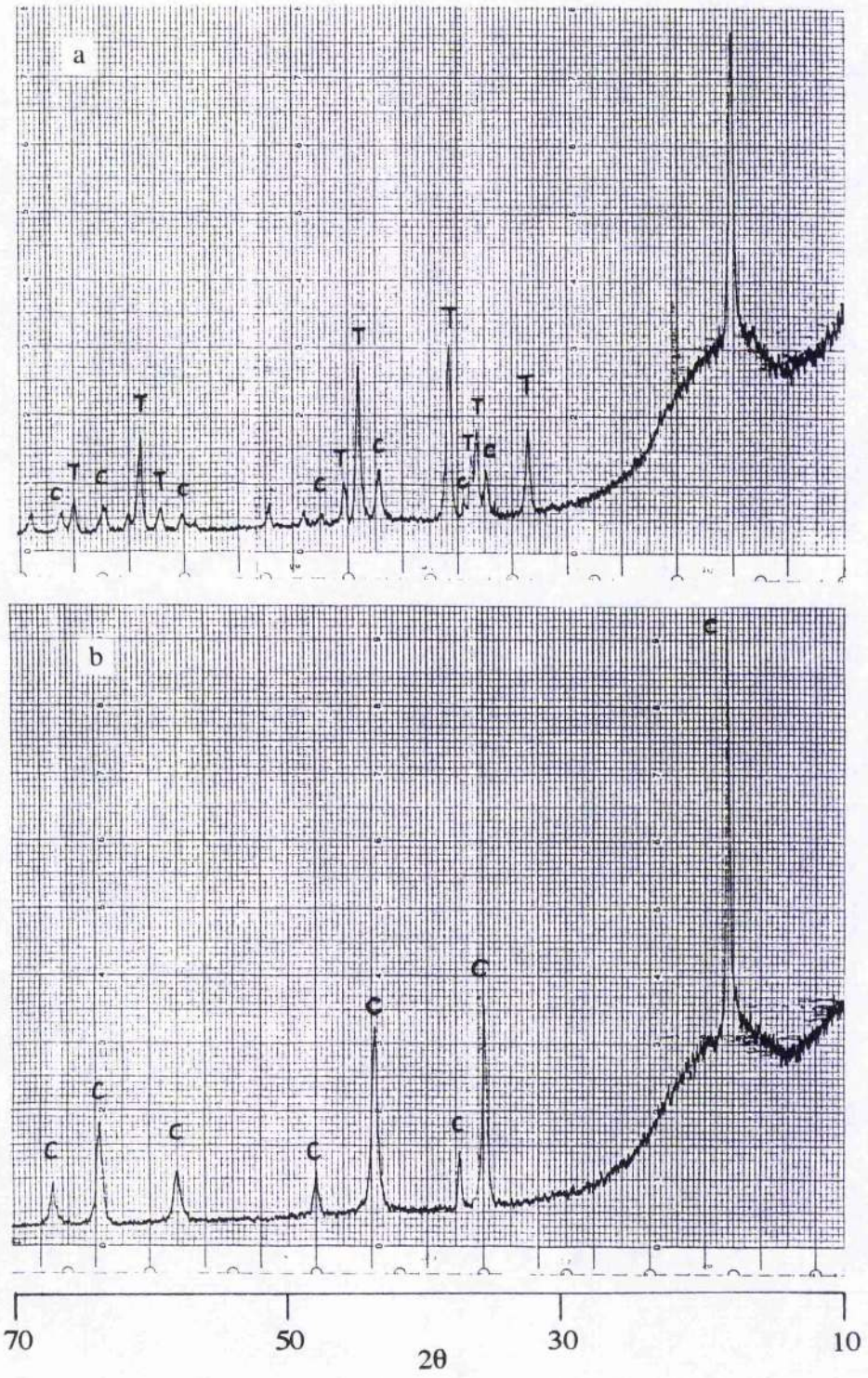

Fig 7-3-3 XRD patterns for a composite electrode based on ssMn850: (a) first discharge to 2.0 V at a current of 0.25 $mA \cdot cm^{-2}$, (b) first charge to 3.7 V at a current of 0.25 $mA \cdot cm^{-2}$. The very broad background peak at low angles (< 30° in 2θ) arises from the tape used to seal the sample from the atmosphere.

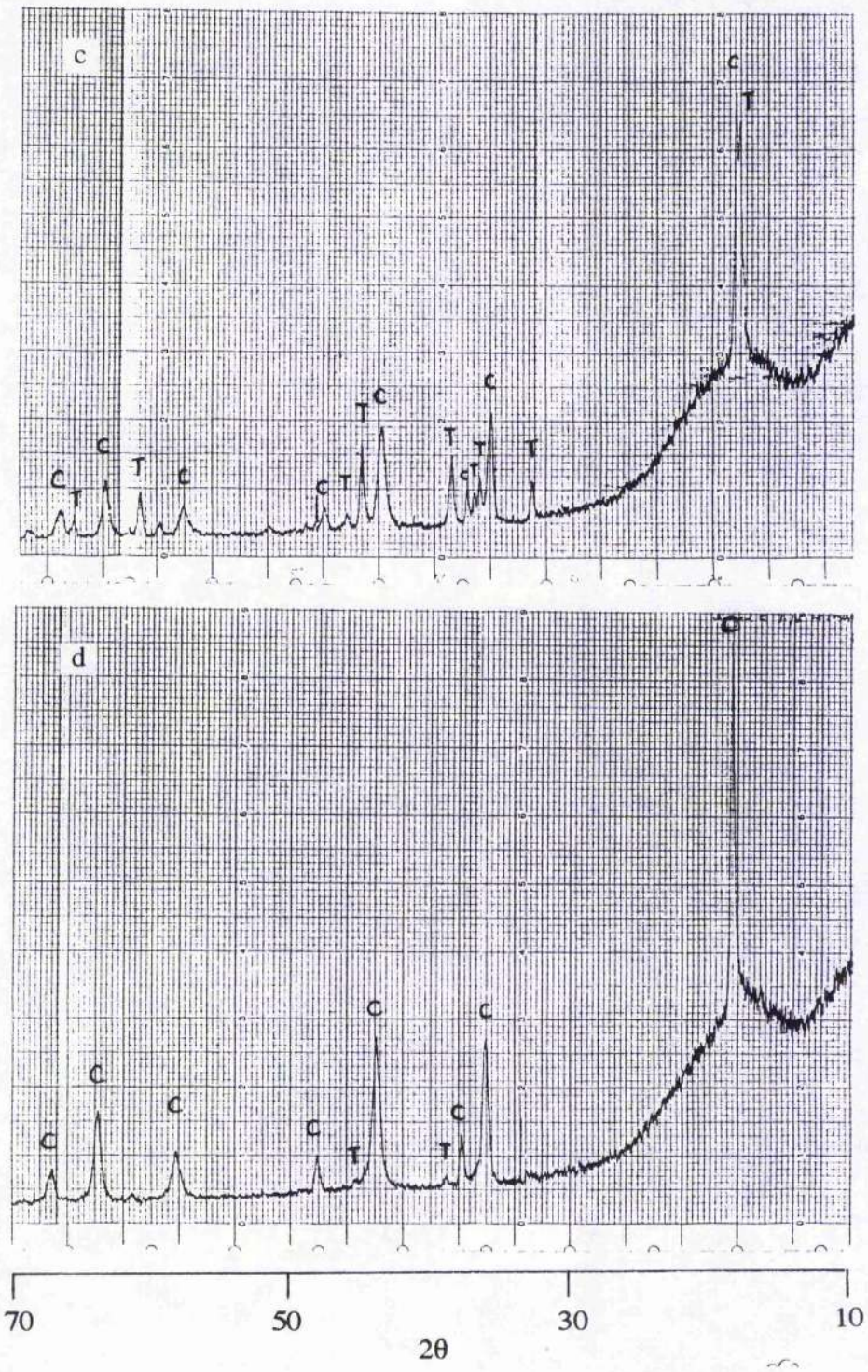

Fig 7-3-3 XRD patterns for a composite electrode based on ssMn850: (c) discharge to 2.0 V at a current of 0.25 $mA \cdot cm^{-2}$ after 50 cycles at a current of 0.75 $mA \cdot cm^{-2}$, (d) charge to 3.7 V at a current of 0.25 $mA \cdot cm^{-2}$ after 50 cycles at a current of 0.75 $mA \cdot cm^{-2}$. The very broad background peak at low angles (< 30° in 2θ) arises from the tape used to seal the sample from the atmosphere.

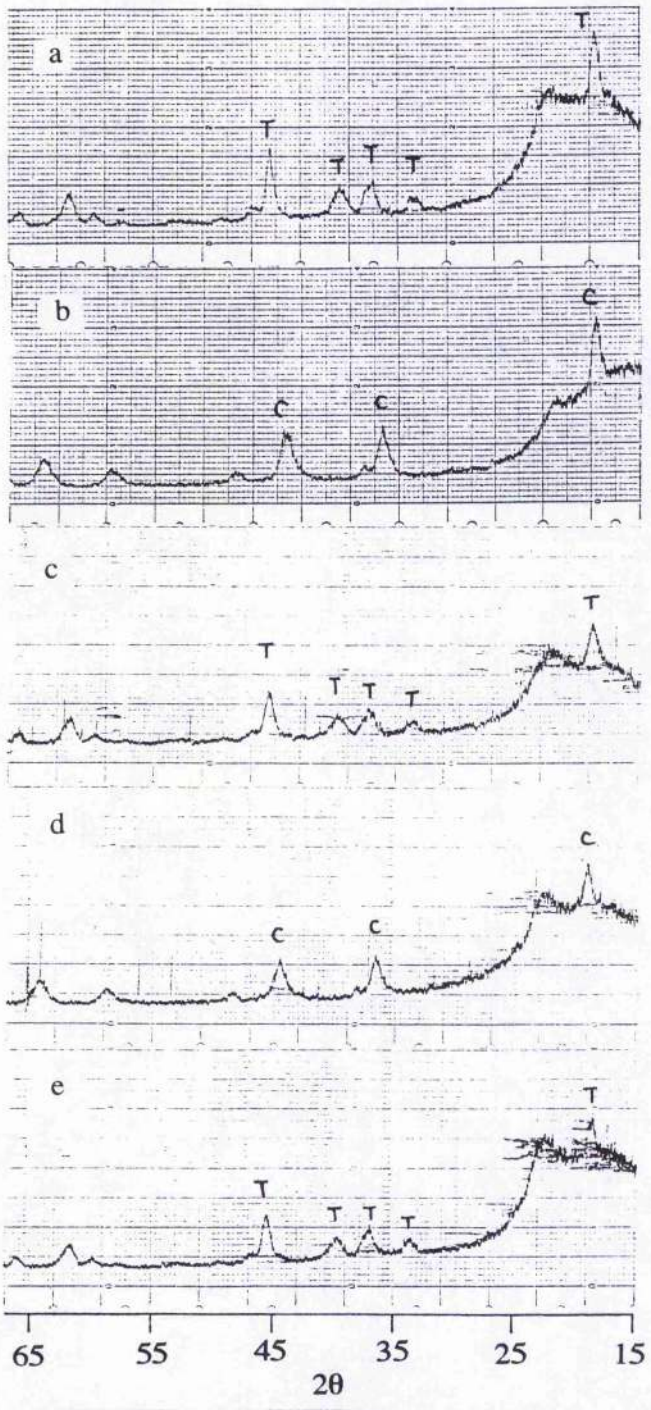

Fig 7-3-4 XRD patterns for a composite electrode based on scMn200: (a) first discharge to 2.0 V at a current of 0.25 $mA \cdot cm^{-2}$, (b) first charge to 3.7 V at a current of 0.25 $mA \cdot cm^{-2}$, (c) discharge to 2.0 V at a current of 0.25 $mA \cdot cm^{-2}$ after 50 cycles at a current of 0.75 $mA \cdot cm^{-2}$, (d) charge to 3.7 V at a current of 0.25 $mA \cdot cm^{-2}$ after 50 cycles at a current of 0.75 $mA \cdot cm^{-2}$, (e) discharge to 2.0 V at a current of 0.75 $mA \cdot cm^{-2}$ after 100 cycles at a current of 0.75 $mA \cdot cm^{-2}$. The very broad background peak at low angles ($< 30^{o}$ in 2θ) arises from the tape used to seal the sample from the atmosphere.

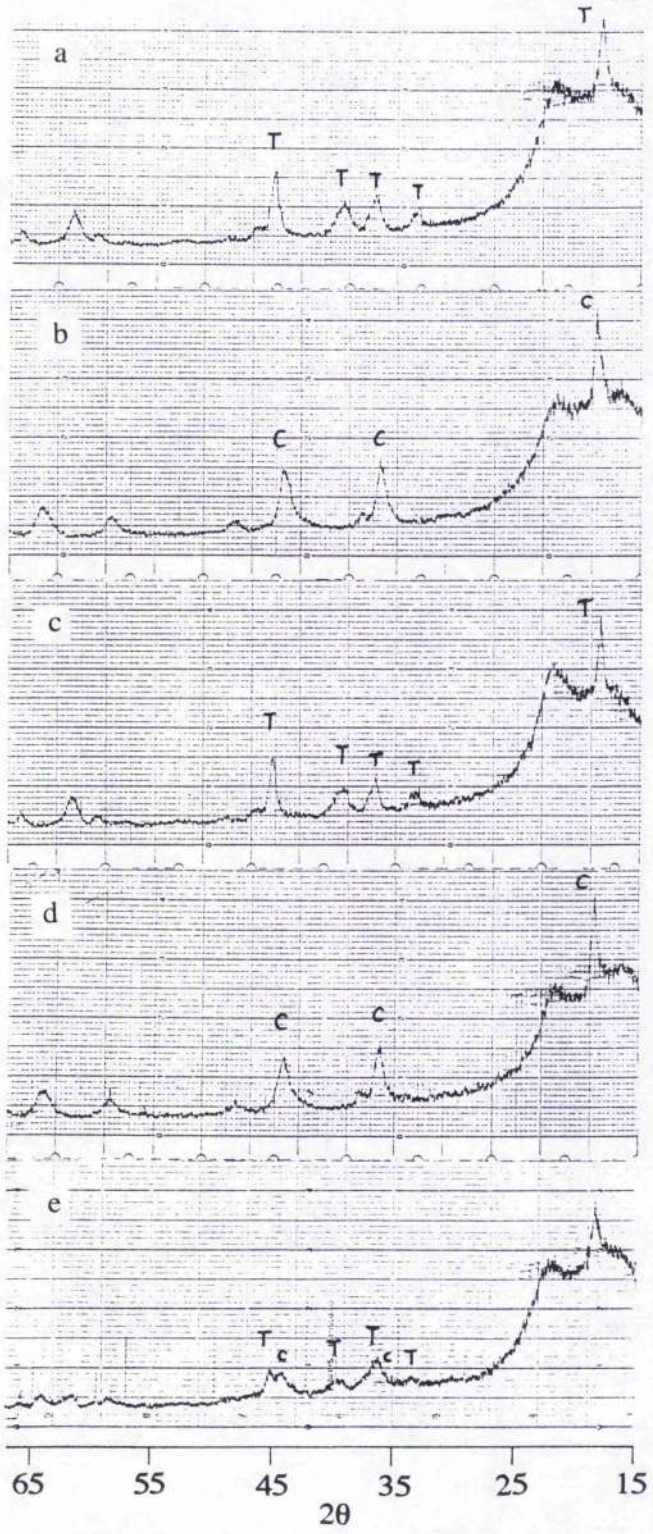

Fig 7-3-5 XRD patterns for a composite electrode based on sMn200: (a) first discharge to 2.0 V at a current of 0.25 $mA \cdot cm^{-2}$, (b) first charge to 3.7 V at a current of 0.25 $mA \cdot cm^{-2}$, (c) discharge to 2.0 V at a current of 0.25 $mA \cdot cm^{-2}$ after 50 cycles at a current of 0.75 $mA \cdot cm^{-2}$, (d) charge to 3.7 V at a current of 0.25 $mA \cdot cm^{-2}$ after 50 cycles at a current of 0.75 $mA \cdot cm^{-2}$, (e) discharge to 2.0 V at a current of 0.75 $mA \cdot cm^{-2}$ after 100 cycles at a current of 0.75 $mA \cdot cm^{-2}$. The very broad background peak at low angles ($< 30^{o}$ in 2θ) arises from the tape used to seal the sample from the atmosphere.

The specific discharge capacities of the three electrodes, ssMn850, scMn200 and sMn200, on the 50 cycles are presented Fig 7-3-6. By comparing the X-ray results with the loss of capacity on cycling, it appears that such capacity loss correlates with an inability to completely transform the cubic to tetragonal phase throughout the entire electrode structure. This is most clearly seen in the case of the solid state material, ssMn850, where we can see there is a significant proportion of cubic phase left after discharging on the fiftieth cycle. Since the tetragonal unit cell is larger than the cubic unit cell, the spinel will expand and contract as a result of the phase transition during cycling. It is known that this volume change is 6.5 % [13]. Contraction is more likely to lead to a loss of contact between particles if the electrode is not sufficiently flexible to accommodate the change. In the extreme case the formation of isolated islands will occur which can no longer participate in the subsequent intercalation reaction, hence some unreacted cubic phase is left after discharge. Fig 7-3-7 illustrates this schematically. It is not unusual in battery studies to find that active materials become less compact due to liquid electrolyte penetration; the phase transformation undoubtedly increases this adverse process.

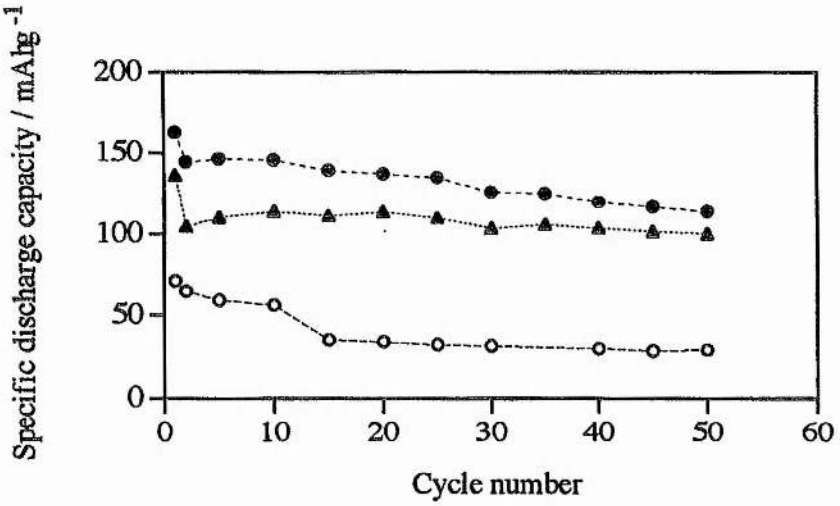

Fig 7-3-6 Retention of capacities for electrodes cycled at a current of 0.75 $mA \cdot cm^{-2}$ (C/4) and with 3.7 V and 2.0 V cutoffs. (●)scMn200, (▲)sMn200, (○) ssMn850.

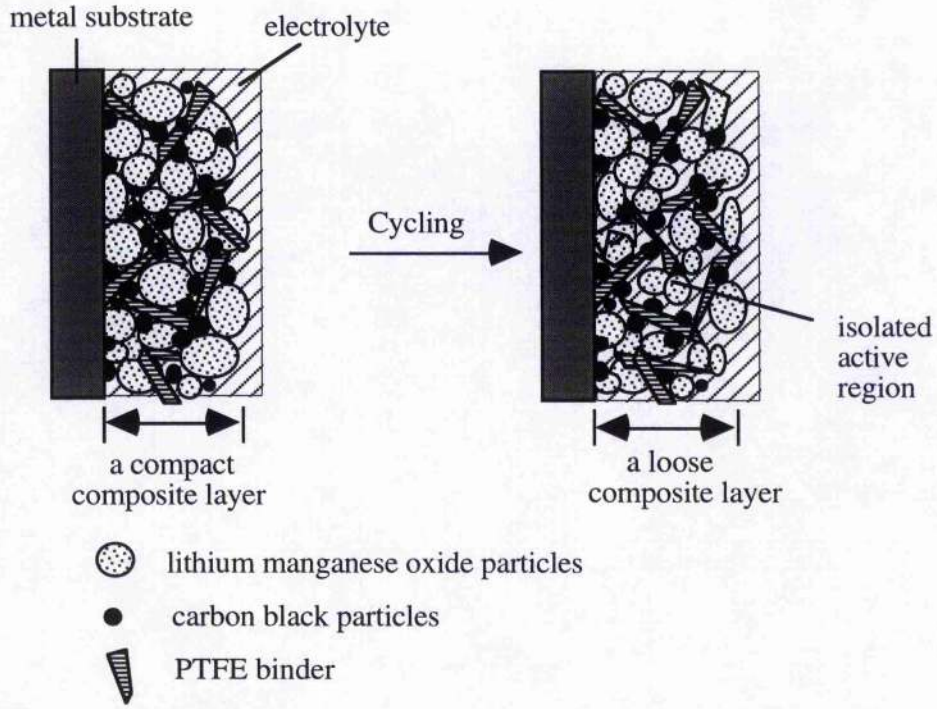

Fig 7-3-7 Schematic explanation of a change of compaction of a composite electrode.

Nohma et al. also carried out X-ray diffraction studies after cycling composite cathodes based on $LiMn_2O_4$ for 400 cycles [18], but X-ray diffraction patterns only collected after charging. In accord with our results above, they found no significant change in the XRD pattern after cycling. As can be seen here, it is impossible to explain the capacity fade of spinel electrodes without considering the structure change occurring at the end of discharge after cycling.

7-3-4 Phase transition within $LiMn_2O_{4.1}$ with and without carbon

From the X-ray results presented so far it would appear that no cubic phase is present at the end of discharge after 50 cycles for the scMn200 and sMn200 electrodes (Fig 7-3-4 (c), and Fig 7-3-5 (c)). However, Fig 7-3-6 indicates that capacity does indeed decrease for these two electrodes although it is much less significant than the

ssMn850 electrode. The better capacity retention for scM200 and sMn200 would suggest that less cubic material should exist after 50 cycles. Given the very broad X-ray peaks for these electrodes, it is possible that some small proportion of cubic phase is present but not observed in the powder patterns. A second possibility is that by carrying out one low current cycle immediately prior to the X-ray measurements some recovery in cyclability and hence reversibility of structural transformation had occurred. As indicated in Fig 7-2-5, the enhancement of cyclability due to the addition of carbon during the synthesis takes effect after the first 50 cycles. In other words, we would not expect to see a significant difference in the reversibility of the cubic/tetragonal transition for the solution based spinel with and without carbon until longer term cycling. In order to explore the origin of capacity fade in these two electrodes and understand the very significant difference of capacity retention between these two electrodes, the scMn200 and sMn200 electrodes were therefore subjected to a further 50 cycles at a higher current of 0.75 $mA \cdot cm^{-2}$ (C/4). Capacities for these electrodes could no longer be calculated because the act of transferring the electrodes between the cycling cells and the diffraction sample holder inevitably resulted in loss of material. After 100 cycles, the electrodes were discharged to 2.0 V at the same high current (0.75 $mA \cdot cm^{-2}$), and then ex-situ X-ray diffraction patterns were taken. The sMn200 electrode exhibited evidence of both tetragonal and cubic phases (Fig 7-3-5 (e)). This suggests that the loss of contact mechanism used to explain capacity fade for the ssMn850 material also operates in the case of the sMn200 electrode. However, it is less significant in the latter case indicating that the smaller particle size may yield a more flexible electrode.

The scMn200 electrode showed no evidence of two phases at the end of discharge ever after 100 cycles (Fig 7-3-5 (e)). One possible explanation is that the additional carbon ensures better electronic contact between particles. To examine this, the two spinel powders were pressed into pellets and sandwiched between two stainless steel electrodes and their conductivities measured using the ac impedance technique. The experimental results showed that both have a conductivity value around the same

order of magnitude i.e. 10^{-6} Scm^{-1} at room temperature. This result implies that the carbon particles which are added during synthesis do not enhance the electronic contact. The presence of fine carbon between the spinel particles may however improves flexibility.

7-4 Electrochemical characterisation after cycling

The relationship between capacity fade and the structural phase transition between cubic and tetragonal spinel has been clearly demonstrated above. The precise role of carbon although speculated upon cannot be regarded as understood in detail. The following electrochemical experiments attempt to further study the solution based spinels with and without carbon in order to understand better the role of carbon and find out if there are other factors which relate to a deterioration in performance .

7-4-1 Ac impedance

There are two questions of interest: is the electrode process the same for spinels with and without carbon and does it change after cycling? The ac impedance technique is a useful one to study the mechanism of electrode reactions. The sMn200 and scMn200 based cathodes used in Fig 7-2-5 were therefore examined by ac impedance before and after being subjected to 300 cycles. Note that after cycling these electrodes were reassembled with fresh lithium electrodes and electrolyte to avoid possible interference from lithium dendrites, which result in a "short circuit" between the counter and reference electrodes.

Fig 7-4-1 presents ac impedance spectra for a fresh sMn200 electrode measured at the ends of charge and discharge, respectively. The same ac impedance experiments were also carried out for a fresh scMn200 electrode but no significant difference was observed, indicating that the presence of carbon does not vary the mechanism of

electrochemical intercalation within spinel. It is interesting to note that the semicircle of the ac impedance spectra enlarges on discharge by comparing Fig 7-4-1 (a) and (b). This may imply a lower rate of electron transfer process within the tetragonal spinel host.

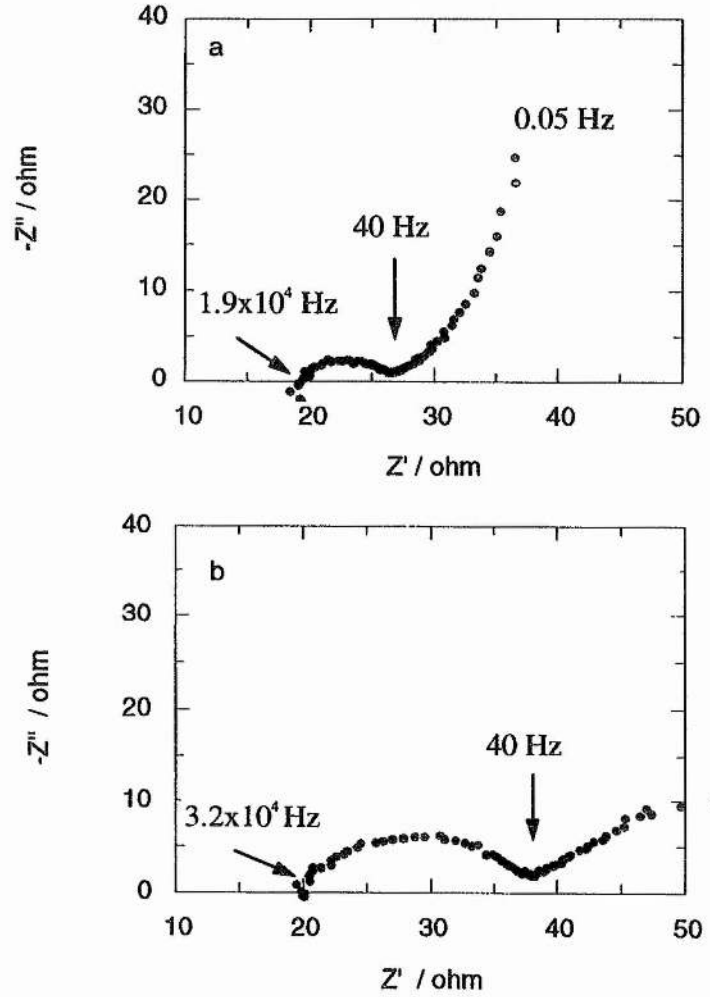

Fig 7-4-1 Ac impedance spectra of a fresh sMn200 electrode measured: (a) at the end of charge and (b) at the end of discharge. Cycling conditions were the same as those in Fig 7-2-5.

After 300 cycles, the ac impedance spectra at the end of charge for both electrodes do not appear to have changed in shape (Fig 7-4-2 (a) and Fig 7-4-3 (a)). This suggests no significant change in electrode reaction mechanism. However, the semicircles sizes increase, around two times. This increase may relate to the loss of contact

between particles as a result of the cubic/tetragonal transformation, and hence reduces the apparent rate of electron transfer in electrodes. The ac impedance spectra at the end of discharge after 300 cycles are somewhat complicated. The semicircle sizes for both cycled electrodes, see Fig 7-4-2 (b) and Fig 7-4-3 (b), do not enlarge very much on discharge in contrast to the situation observed for a fresh electrode (Fig 7-4-1). Further making a comparison between the fresh electrode and the cycled electrodes, it is evident that the semicircle size in the discharged state decreases after 300 cycles. This result may reflect the presence of less tetragonal material at the end of discharge after 300 cycles than is the case after 1 cycle as found by X-ray diffraction studies in **7-3-3**. The shape of the spectra at the end of discharge shows some difference between the sMn200 and scMn200 electrodes after 300 cycles. In the case of the scMn200 electrode (Fig 7-4-3 (b)), a linear segment is observed at high frequencies end. The origin of this is not understood at present.

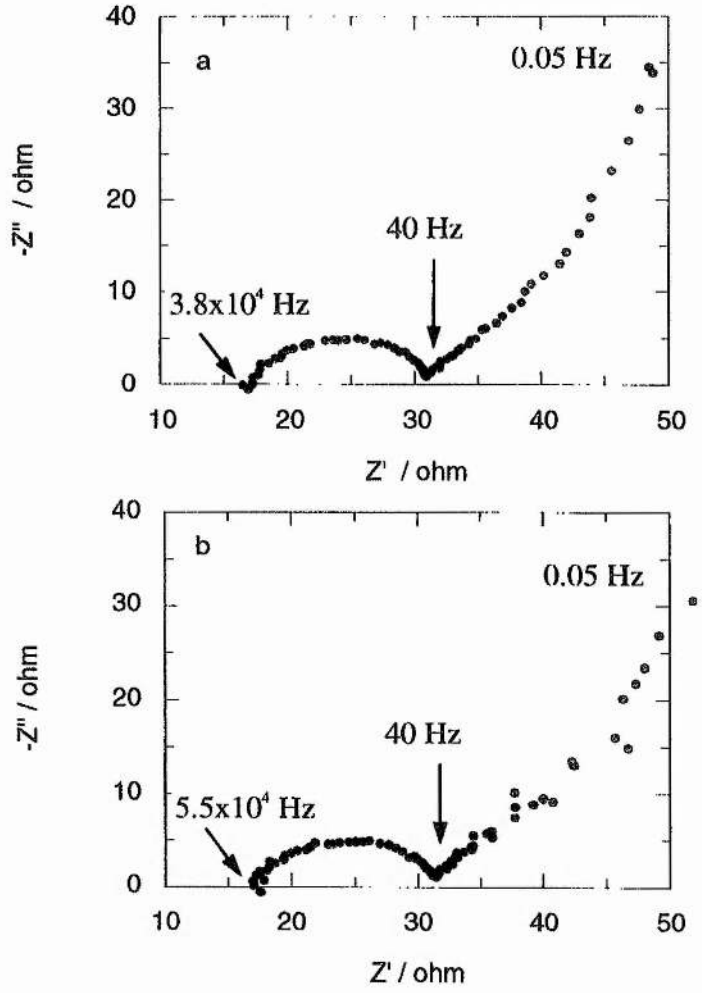

Fig 7-4-2 Ac impedance spectra of sMn200 electrode measured after 300 cycles between 3.7 V and 2.0 V and at a current of 1 $mA \cdot cm^{-2}$ for discharging and 0.5 $mA \cdot cm^{-2}$ for charging: (a) at the end of charge and (b) at the end of discharge.

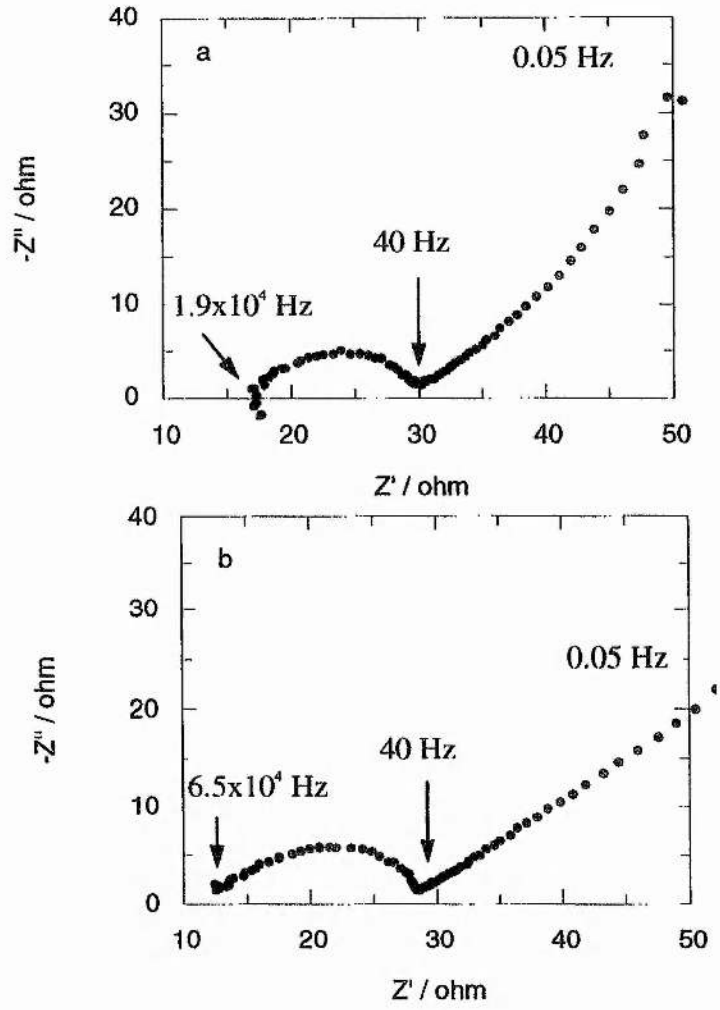

Fig 7-4-3 Ac impedance spectra of scMn200 electrode measured after 300 cycles between 3.7 V and 2.0 V and at a current of 1 $mA \cdot cm^{-2}$ for discharging and 0.5 $mA \cdot cm^{-2}$ for charging: (a) at the end of charge and (b) at the end of discharge.

7-4-2 Cyclic voltammetry

Fig 7-4-4 presents the cyclic voltammograms for the sMn200 and scMn200 electrodes used in Fig 7-2-5, displaying no apparent change except for a decrease in magnitude of peak current after 300 cycles. Such results are consistent with a loss of active substance as cycling proceeds but otherwise no change.

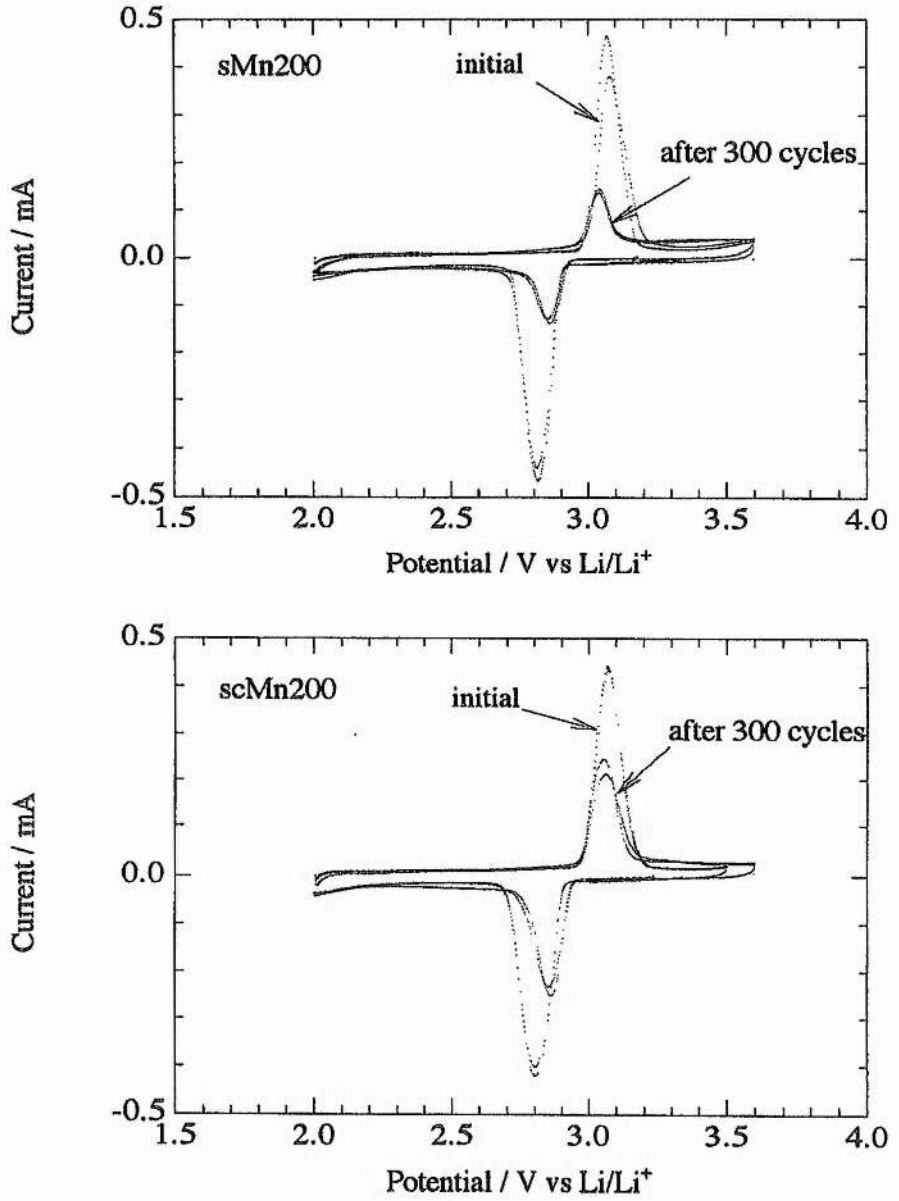

Fig 7-4-4 Cyclic voltammograms of sMn200 and scMn200 composite cathodes at initial and after 300 cycles between 3.7 V and 2.0 V and under a current of 1 $mA \cdot cm^{-2}$ for discharging and 0.5 $mA \cdot cm^{-2}$ for charging.

7-4-3 Stability of the spinel at the end of discharge

In addition to the loss of contact between particles as a result of the Jahn-Teller effect, this section explores other possible causes of capacity fade related in particular to the stability of the electrode in contact with the electrolyte. In the discharge state the

spinel possesses a high proportion of Mn^{3+} and possible even some Mn^{2+} whereas when fully charged less than 50 % of the manganese is in the 3+ state the rest being 4+. Mn^{3+} is known to disproportionate readily into Mn^{4+} and Mn^{2+} for example when dissolved in an aqueous solution. In order first to study the stability of a fully charged electrode, a sMn200 electrode was left on open circuit for 1300 hours after it had undergone voltammetric cycle from 2.0 V to 4.3 V then ending at 3 V. Subsequently, this electrode was cycled between 2.0 V and 4.3 V and showed only a small change in peak height and shape (Fig 7-4-5). In conclusion, the spinel is stable in contact with the electrolyte when in the charged state.

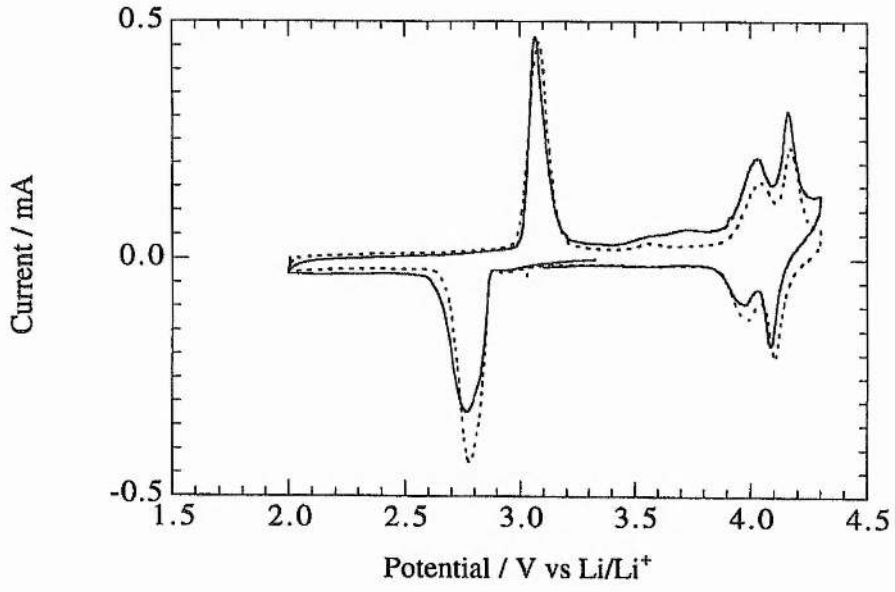

Fig 7-4-5 Cyclic voltammograms for a sMn200 composite electrode before (---) and after (—) standing in open circuit for 1300 hours. (10 $\mu V \cdot s^{-1}$).

Considering now the stability in the discharged state, another sMn200 electrode was discharged by a slow potential sweep to 2.0V at 10 $\mu V \cdot s^{-1}$, (discharge capacity ~ 164 $mAhg^{-1}$), and then left on open circuit. After standing for a period of time, the open circuit potential of the electrode was recorded and then the electrode was cycled again between 3.5 V and 2.0 V at the same scan rate (10 $\mu V \cdot s^{-1}$). After one or two cycles the scan was terminated at 2.0 V and then the cell left on open circuit. These steps

were repeated on several occasions with different times on open circuit. It was found that the open circuit potential varied with time, see Fig 7-4-6. Also the heights of redox peaks in subsequent cyclic voltammograms decreased with increasing time on open circuit, see Fig 7-4-7. The peak currents remained low even after repeating cycling between 3.5 V and 2.0 V. The electrode was then swept to the much higher potential of 4.3 V and cycled twice between 2.0 and 4.3 V. Fig 7-4-8 presents the cyclic voltammogram indicating that the peaks associated with the 3 V redox process (i.e. at 2.75 and 3.1 V) have now grown significantly in height compared with the corresponding peaks in Fig 7-4-7. However again the peak current diminish on subsequent cycling. Cell postmortems after cycling this wide voltage range showed the pads between electrodes to be red in colour indicating that some lithium manganese oxide dissolution had taken place. Similar tests were also done using the composite cathodes containing respectively scMn200 and ssMn850 materials, and gave similar results.

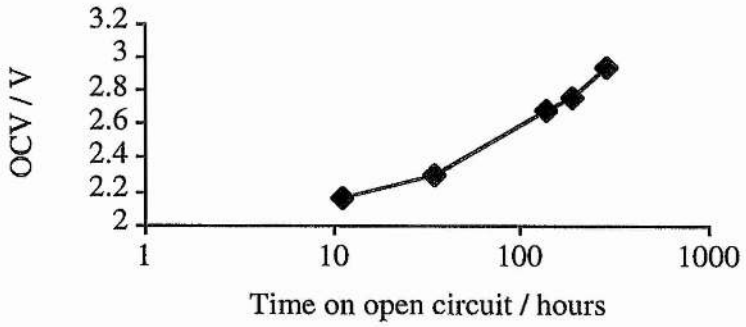

Fig 7-4-6 Variation of the potential of a fully discharged composite electrode containing the spinel from solution synthesis as a function of standing time at open circuit (1 M $LiAsF_6$/PC).

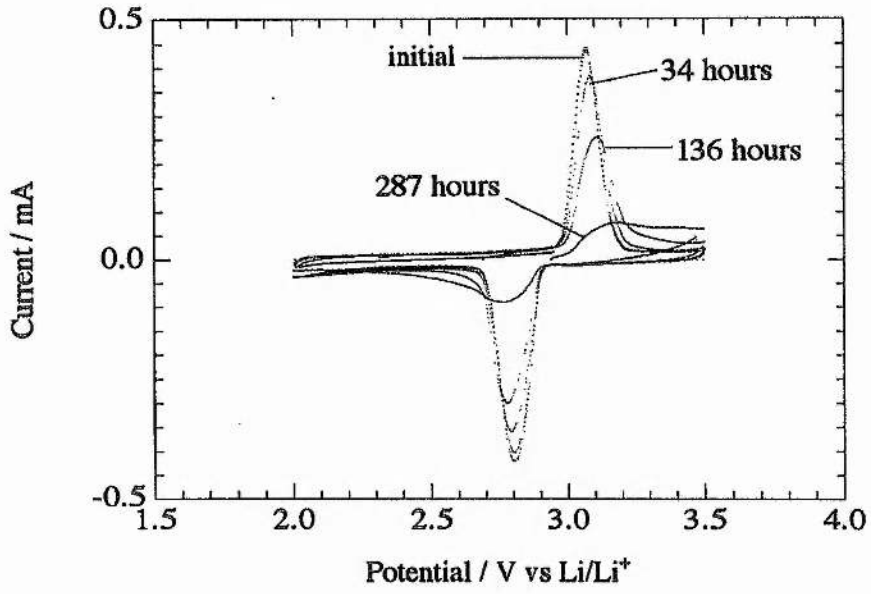

Fig 7-4-7 Cyclic voltammograms for the sMn200 electrode. The values in the figure represent the periods of time left standing on open circuit ($10\ \mu V \cdot s^{-1}$, 1 M $LiAsF_6$/PC)

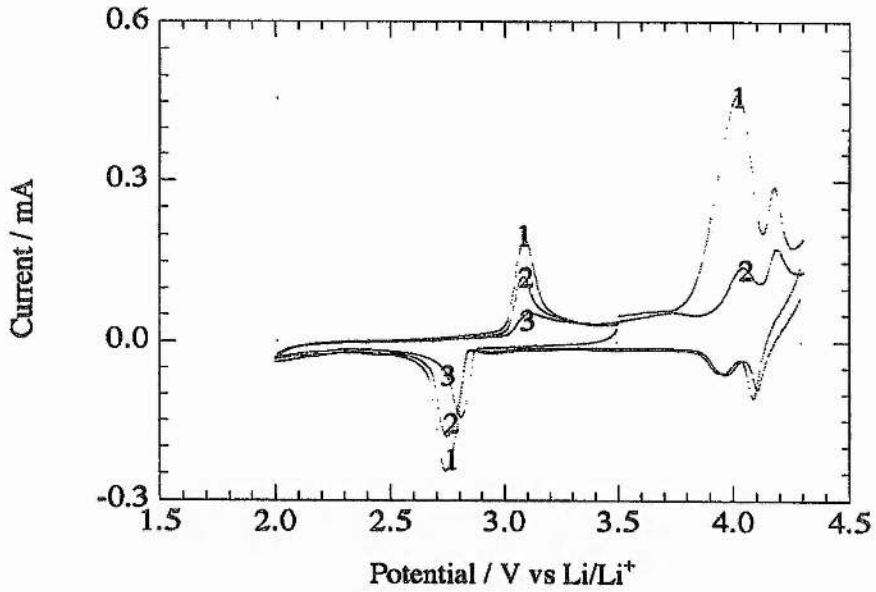

Fig 7-4-8 Cyclic voltammograms for a sMn200 electrode after standing in the discharged state for 287 hours. The values in the figure represent the cycle number. ($10\ \mu V \cdot s^{-1}$, 1 M $LiAsF_6$/PC).

It is evident that the spinel is not stable in the discharged state. This has important consequence for its use in 3 V rechargeable lithium batteries. The experimental

results suggest possible Mn(III) disproportionation leading to the decomposition of spinels which causes a permanent loss of capacity of the spinel electrodes. In view of the fact that oxidation to 4.3 V induces some at least temporary recovery of the capacity at 3V, we may qualitatively conclude that the loss of performance on standing at the discharged state is associated with a layer of disproportionated material at the electrode surface. Two possible mechanism for the disproportionation are assumed:

$$Li_2Mn_2O_4 \rightarrow MnO_2 + Li_2MnO_2 \rightarrow MnO_2 + MnO + Li_2O$$

or

$$Li_2Mn_2O_4 \rightarrow Li_2MnO_3 + MnO$$

However, many others could be postulated. The exact nature of the dissolution occurring in the discharged state needs further work. Nevertheless the disproportionation reaction of Mn(III) is time dependent if it occurs.

7-5 Conclusions

Low temperature spinel $LiMn_2O_{4.1}$ prepared by solution synthesis with the addition of carbon and fired at 200 °C exhibits excellent performance as a 3 volt cathode. This material yields a discharge capacity of 145 $mAhg^{-1}$ at a discharge rate of C/2 between the voltage limits of 3.7 V and 2.0 V, nearly twice that of the spinel prepared by conventional solid state reaction at high temperature (80 $mAhg^{-1}$). Compared with the spinel prepared by the same solution route but without carbon, an enhancement of 50 % in capacity retention after 300 cycles at a discharge rate of C/2 is observed. After 300 cycles at a discharge rate of C/2, 65 % of initial capacity remains.

The main factor responsible for capacity fade in 3 V lithium manganese oxide spinels has been shown to be the build up of cubic material on the discharge cycles. This arises from the cubic to tetragonal phase transition and the associated volume increase which leads to isolation of particles when the cathode is recharged. Such cubic

particles are not available for further intercalation. Carbon particles added during the synthesis result in more complete transformation between cubic and tetragonal phases throughout the electrode. This may be due to the extra flexibility of the composite electrode with dispersed carbon leading to a better accommodation of the expansion and contraction. The fully discharged electrode is not stable, storage time in the discharged state is critical to the performance of the electrode. Because the concentration of Mn (III) in spinel increases on discharge, the disproportionation of Mn (III) may occur and this could be the origin of the deterioration of the electrode on open circuit at the fully discharged potential.

References

[1] K.Brandt, Solid state Ionics, **69** 173 (1994).

[2] Tsutomu Ohzuku, and Atsushi Ueda, Solid State Ionics, **69** 201 (1994).

[3] Industrial Chemical Library, Volumn 5, Lithium Batteries New Materials, Development, and Perspectives, edited by G.Pistoia, ELSEVIER, (1994).

[4] C.Delmas, H.Cognac-Auradou, J.M.Cocciantelli, M.Ménétrier, and J.P.Doumerc, Solid State Ionics, **69** 257 (1994).

[5] M.M.Thackeray, W.I.F.David, P.G.Bruce, and J.B.Goodenough, Mater. Res. Bull., **18** 461 (1983).

[6] J.B.Goodenough, M.M.Thackeray, W.I.F.David and P.G.Bruce, Revue de Chimie Minerale, **21** 435 (1984).

[7] M.M.Thackeray, P.J.Johnson, L.A.de Picciotto, W.I.F.David, P.G.Bruce, and J.B.Goodenough, Mater. Res. Bull., **19** 179 (1984).

[8] G.Pistoia, G.Wang, and C.Wang, Solid State Ionics, **58** 285 (1992).

[9] W.J.Macklin, R.J.Neat, and R.J.Powell, J. Power Sources, **34** 39 (1991)

[10] A.de Kock, M.H.Rossouw, L.A.de Picciotto, M.M.Thackeray, W.I.F.David, and R.M.Ibberson, Mat. Res. Bull., **25** 657 (1990).

[11] M.H.Rossouw, A.de Kock, L.A.de Picciotto, M.M.Thackeray, W.I.F.David, and R.M.Ibberson, Mat. Res. Bull., **25** 173 (1990).

[12] M.M.Thackeray, A.de Kock, M.H.Rossouw, D.Liles, R.Bittihn, and D.Hoge, Preoc. Electrochem. Soc., **P1-3** 326 (1991).

[13] M.M.Thackeray, A.de Kock, M.H.Rossouw, D.Liles, R.Bittihn, and D.Hoge, J. Electrochem. Soc., **139** 363 (1992).

[14] M.M.Thackeray, M.H.Rossouw, A. de Kock, A.P.de la Harpe, R.J.Gummow, K.Pearce, and D.C.Liles, J. Power sources, **43-44** 289 (1993).

[15] R.J.Gummow, A.de Kock, and M.M.Thackeray, Solid State Ionics, **69** 59 (1994).

[16] T.Nohma, Y.Yamamoto, I.Nakane, and N.Furukawa, J. Power Sources, **39** 51 (1992).

[17] T.Nohma, and N.Furukawa, Proc. Electrochem. Soc., **P1-3**, 311 (1991).

[18] T.Nohma, T.Saito, N.Furukawa, and H.Ikeda, J. Power Sources, **26** 389 (1989).

[19] G.Pistoia, and G.Wang, Solid State Ionics, **66** 135 (1993).

[20] T. Takada, H.Hayakawa, and E.Akiba, J. Solid State Chem. **115** 420 (1995).

[21] H. Huang, and P.G.Bruce, J. Power Sources, **54** 52 (1995).

[22] H.Huang, and P. G.Bruce, J. Electrochem. Soc., **141** L76 (1994).

[23] G.Pistoia, M.Pasquali, L.A.De Picciotto, and M.M.Thackeray, Solid State Ionics, **28** 879 (1988).

[24] G.Pistoia, M.Pasquali, G.Wang, and L.Li, J. Electrochem. Soc., **137** 2366 (1990).

[25] J.R.Dahn,U von Sacken, and C.A.Michal, Solid State Ionics, **44** 87 (1990).

[26] T.Ohzuku, A.Ueda, and M.Nagayama, J. Electrochem. Soc., **140** 1862 (1993).

[27] J.N.Reimers, and J.R.Dahn, J. Electrochem. Soc., **139** 2091 (1992).

{28] T.Ohzuku, M.Kitagawa, and T.Hirai, J. Electrochem. Soc., **137** 769 (1990).

[29] C.Lampe-Onnerud, J.O.Thomas, M.Hardgrave, and Steen Yde-Andersen, J. Electrochem. Soc., **142** 3648 (1995).

[30] C.Levy-Clement, Chemical Physics of Intercalation, edited by A.P.Legrand, and S.Flandrois, NATO ASI Series, Series B;Physis, **172** 447 (1987).

[31] Ken-ichi Machida, and M.Enyo, J. Electrochem. Soc., **137** 1169 (1990).

[32] J.M.Tarascon, and D.Guyomard, J. Electrochem. Soc., **138** 2864 (1991).

CHAPTER EIGHT

Summary and Conclusions

8-1 Lithium manganese oxides prepared by a new solution synthesis

8-1-1 Synthesis

A new procedure for the synthesis of lithium manganese oxide spinels has been developed. The following diagram describes the procedure.

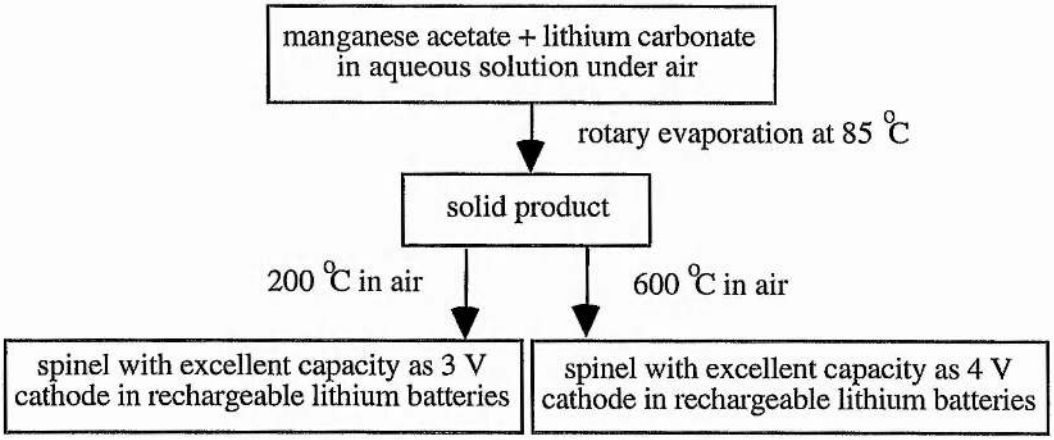

Powder X-ray diffraction studies demonstrate the formation of a single phase spinel even at 200 °C. Formation of the spinel involves γ-Mn_2O_3 phase as an intermediate. The spinel product at 200 °C is a super 3 V cathode material, while raising heating temperature to 600 °C a suitable cathode material for use in 4 V rechargeable lithium batteries is obtained. In addition, adding a small amount of carbon into the solution reaction was performed. This shows an effect of improving the cyclability of the 3 V cathode based on the 200 °C spinel.

This solution route uses Li_2CO_3 instead of LiOH which is employed in alternative sol-gel approaches [1]. As a result there is no need for protection from air using the solution method makes the solution method simpler than the sol-gel. Compared with other literature methods [2, 3], the solution based synthesis reduces preparation temperature of the 4 V spinel materials from over 750 °C to 600 °C.

8-1-2 Characterisation

Chemical analysis, using potentiometric titration, suggests that the spinel obtained from the solution synthesis possesses a variable oxygen content depending on the firing temperature. For example, the spinel fired at 200 °C has the composition $LiMn_2O_{4.1}$, that fired at 600 °C $LiMn_2O_{4.02}$. When the firing temperature exceeds 700 °C, the stoichiometric spinel $LiMn_2O_4$ is obtained.

TEM indicates that the spinel formed at 200 °C possesses a very small particle size, around several hundreds angstroms. It was also found from TEM that the 600 °C spinel has a similarly small particle size, when pre-fired at 200 °C.

Spinels have been prepared by addition of a few percent of carbon to the solution during synthesis. This has no effect on the structure or composition but does influence the electrochemical performance at a substantial degree.

8-2 Electrochemical study of the 600 °C spinel as a 4 V cathode in rechargeable lithium batteries

8-2-1 Performance

The 600 °C spinel obtained from the solution synthesis performs very well as a 4 V cathode in rechargeable lithium cells. This spinel cathode was subjected to galvanostatic cycling at high discharge rate of C/2. Charging was carried out at half that rate in 1 M

$LiClO_4$/PC electrolyte. The spinel based cathode exhibits an initial capacity of 115 $mAhg^{-1}$. This value is ~60 % high than that of the spinel prepared by solid state reaction at 850 °C. Around 90 % of the initial capacity remains after 100 cycles, ~78 % after 200 cycles and ~74 % after 300 cycles. This is very good capacity retention particularly in view of the relatively high discharge rate of C/2 (equivalent to 1 $mAcm^{-2}$) and the deep discharge depth (~80 % of theoretical capacity being discharged initially). The high cycling performance may relate to the fact that this solution spinel has a small particle size and is slightly defect ($LiMn_2O_{4.02}$). When cycled in a 1 M $LiPF_6$/EC+DMC electrolyte, further improvement in capacity is achieved. For example, 133 $mAhg^{-1}$ of capacity was obtained between voltage limits of 4.7 V and 3.3 V and at C/2. This is better than the best result reported in literature (134 $mAhg^{-1}$ at C/3). However, capacity retention strongly depends on the voltage limits used for charging and discharging. Preliminary tests indicate that cycling between the voltage limits of 4.3 V and 3.1 V results in the cathode exhibiting an initial capacity in excess of 120 $mAhg^{-1}$ and retaining a capacity of 110 $mAhg^{-1}$ after 100 cycles. Therefore, a capacity enhancement of at least 5 % is obtained by replacing 1 M $LiClO_4$/PC electrolyte with 1 M $LiPF_6$/EC+DMC.

8-2-2 Origin of capacity decline

Cell postmortems and ac impedance experiments reveal that in $LiClO_4$/PC dissolution of the manganese spinel is in part responsible for the deterioration of spinel cathodes in performance, whereas in $LiPF_6$/EC+DMC the formation of a surface layer may affect the cycle life of the cathode. A surface layer often increases interface resistance and lowers electrode kinetics. The formation and growth of the surface layer in the $LiPF_6$ based electrolyte may arise from (i) chemical reaction between the electrolyte and the spinel, (ii) evaporation of the liquid solvent (DMC is highly volatile). The purity of the $LiPF_6$ salt used should be also considered. In addition, the passivation of the aluminium current collector should not be neglected since the resulting film increases

the contact resistance between cathode material and the metal. These interfacial properties always relate to the chemistry of electrolytes so that optimisation of electrolyte composition is of great importance to minimise these problems.

8-3 Electrochemical study of the 200 °C spinel as a 3 V cathode in rechargeable lithium batteries

8-3-1 Performance

The spinel prepared by the solution synthesis and fired at 200 °C ($LiMn_2O_{4.1}$) is an excellent 3 V cathode. Under galvanostatic cycling between 3.7 V and 2.0 V and at a high discharge rate of C/2 (1 $mAcm^{-2}$), the cathode based on this solution spinel can deliver an initial discharge capacity as high as 140 $mAhg^{-1}$ (charging at C/4). In contrast only 80 $mAhg^{-1}$ of capacity is obtained under identical conditions from the spinel prepared by solid state reaction at 850 °C. Furthermore, the solution based spinel also exhibits a higher capacity retention. After 100 cycles, the cathode retains a capacity in excess of 100 $mAhg^{-1}$ but the capacity of the cathode based on solid state spinel declines to less than 50 $mAhg^{-1}$. The high performance is likely to be associated with the fact that the solution based spinel has small particle size, several hundred angstroms, (giving good cyclability) and a high oxidation state ($Mn^{+3.6}$ in $LiMn_2O_{4.1}$) (giving high capacity). However, a very significant improvement in capacity retention is achieved by adding a small amount of carbon (less than 1 % of starting materials) during the synthesis of the spinel. The 200 °C spinel prepared with carbon yields initially a capacity of over 140 $mAhg^{-1}$, and 125 $mAhg^{-1}$ remains at 100 cycles, 100 $mAhg^{-1}$ at 200 cycles and 90 $mAhg^{-1}$ at 300 cycles. Compared with the spinel without carbon, there is an enhancement of ~50 % in capacity retention after 300 cycles!

8-3-2 Capacity decline

Although the solution based preparation and in particular the addition of carbon during synthesis improve the cycle life of the spinel cathode, capacity declines on cycling on the 3 V plateau much more rapidly than does the 4 V material when cycled at 4 V. In order to understand the capacity loss at 3 V, X-ray diffraction measurements were carried out during cycling of the 3 V cathode. Ex-situ X-ray diffraction experiments indicate that the phase transition from cubic to tetragonal spinel is incomplete during discharge, resulting in capacity decrease. The transformation from cubic to tetragonal phases arises from the Jahn-Teller distortion associated with lithium insertion into spinel and reduction of Mn^{4+} to Mn^{3+}. This is accompanied by an increase of unit cell volume of 6.5 %. As a result, contact is likely to be lost between particles in the spinel cathode under repeated charge and discharge cycles. Compared to the spinel prepared by high-temperature solid state reaction, the 200 °C spinel ($LiMn_2O_{4.1}$) exhibits a relatively slow development of cubic material at the end of discharge on cycling. As a result its capacity declines relatively slowly. It may be that the small particle size reduces the effect of the volume change. The 200 °C spinel prepared with carbon shows no significant cubic phase present at the end of discharge within the first 100 cycles. Perhaps the highly dispersed carbon particles raise the flexibility of the spinel electrode permitting it to accommodate the contract and expansion.

It was also found that the fully discharged cathode is not stable in contact with electrolyte. This may be due to the tendency of Mn^{3+} to disproportionation, another factor which will reduce capacity retention on cycling.

8-4 Future work

Although the spinel fired at 600 °C possesses a performance at least as good as anything currently available, there remain problems of self discharge which can also influence cyclability. Optimisation of the electrolyte composition containing $LiPF_6$ and EC plus DMC solvents will be expected. An recent study of $LiMn_2O_4$ corrosion in various electrolytes such as $LiClO_4$, $LiPF_6$ and $LiBF_4$ has found that $LiClO_4$ is the

most corrosive and $LiBF_4$ the least. The study concluded that the dissolution of manganese oxides is a major factor of capacity decline on cycling [4]. A defect spinel such as $LiMn_{2-x}Li_xO_4$ has been also reported to be of benefit of improving the cyclability of the cathode [5, 6]. A systematic study of the mechanism of self discharge and consequent capacity loss, in particular separating reversible from irreversible self-discharge, would form important future work. Careful studies of the reaction between electrolyte and electrode, of Mn dissolution and of any change in the defect structure will be necessary. Finally, one of the purposes of studying the 4 V lithium manganese oxide spinel is to construct a lithium ion battery. This would form part of a future programme of work. The variation of cycling and self discharge with temperature has not be studied but is important and would be examined in any future investigation.

The cyclability of the 3 V spinel cathode has been investigated by ex-situ X-ray diffraction but the study was limited to 100 cycles. It would be interesting in future work to monitor the cubic/tetragonal phase transformation during long term cycling. In particular, the stability of the tetragonal phase in contact with different electrolytes is worth further studying. Uses of other techniques than those employed here would be important in future work. For example, EPR to distinguish Mn^{2+} from Mn^{4+} in the electrolyte solution following dissolution.

Reference

[1] P.Barboux, J.M.Tarascon, and F.K.Shokoohi, J. Solid State Chem., **94** 185 (1991).

[2] V.Manev, A.Momchilov, A.Nassalevska, and A.Sato, J. Power Sourse, **54** 323 (1995).

[3] J.M.Tarascon, W.R.Mckinnon, F.Coowar, T.N.Bowmer, G.Amatucci, and D.Guyomard, J. Electrochem. Soc., **141** 1421 (1994).

[4] H. Mao, J.N.Reamers, Q.Zhong, and U von Sacken, Electrochem. Soc. Proceedings, **94-28** 245 (1994).

[5] A.Yamada, J. Solid State Chem., **122** 160 (1996).

[6] M.M.Thacheray, J. Electrochem. Soc., **142** 2558 (1995).

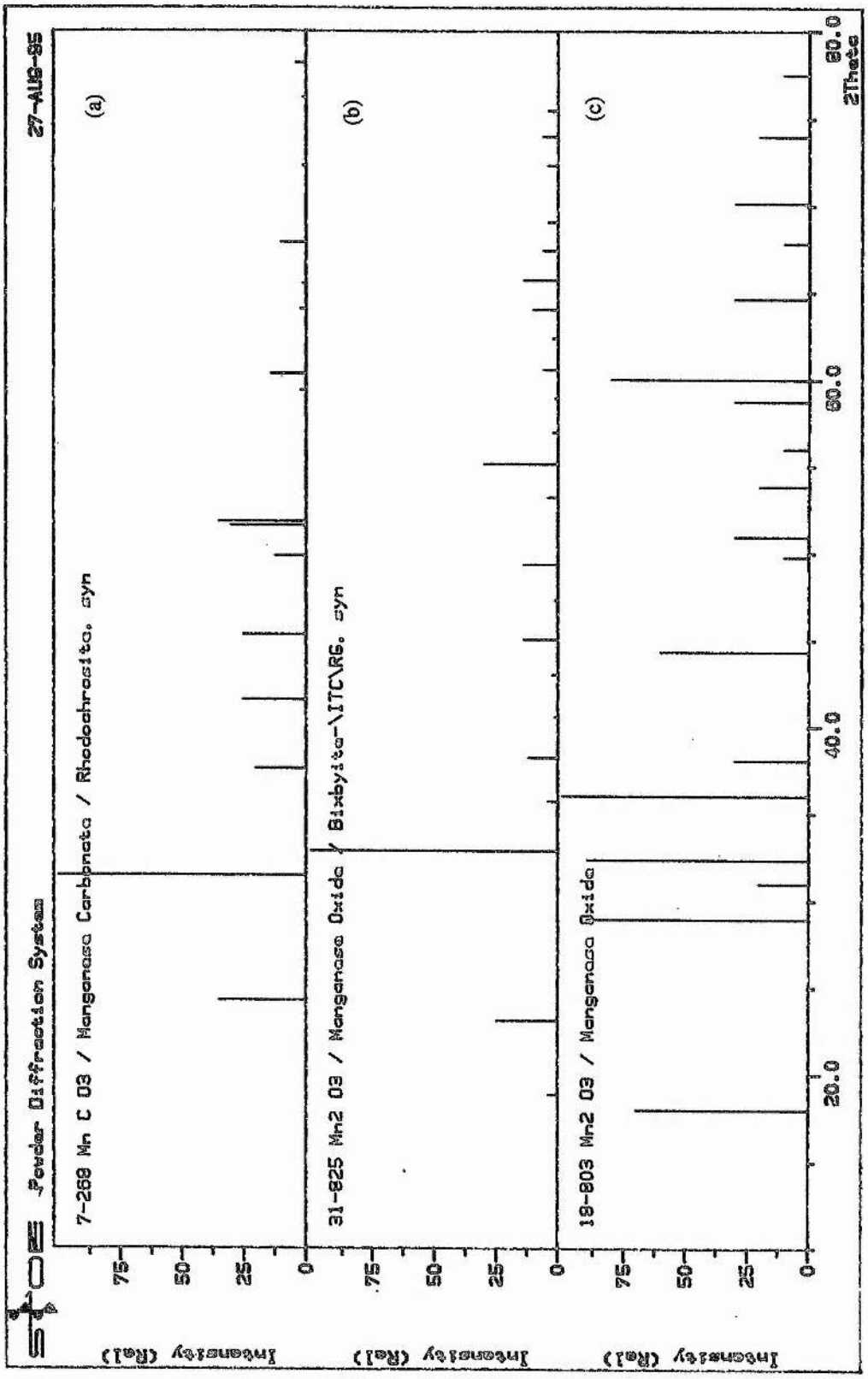

Appendix I Standard patterns from ICDD powder diffraction files: (a) $MnCO_3$, (b) α-Mn_2O_3 and (c) γ-Mn_2O_3

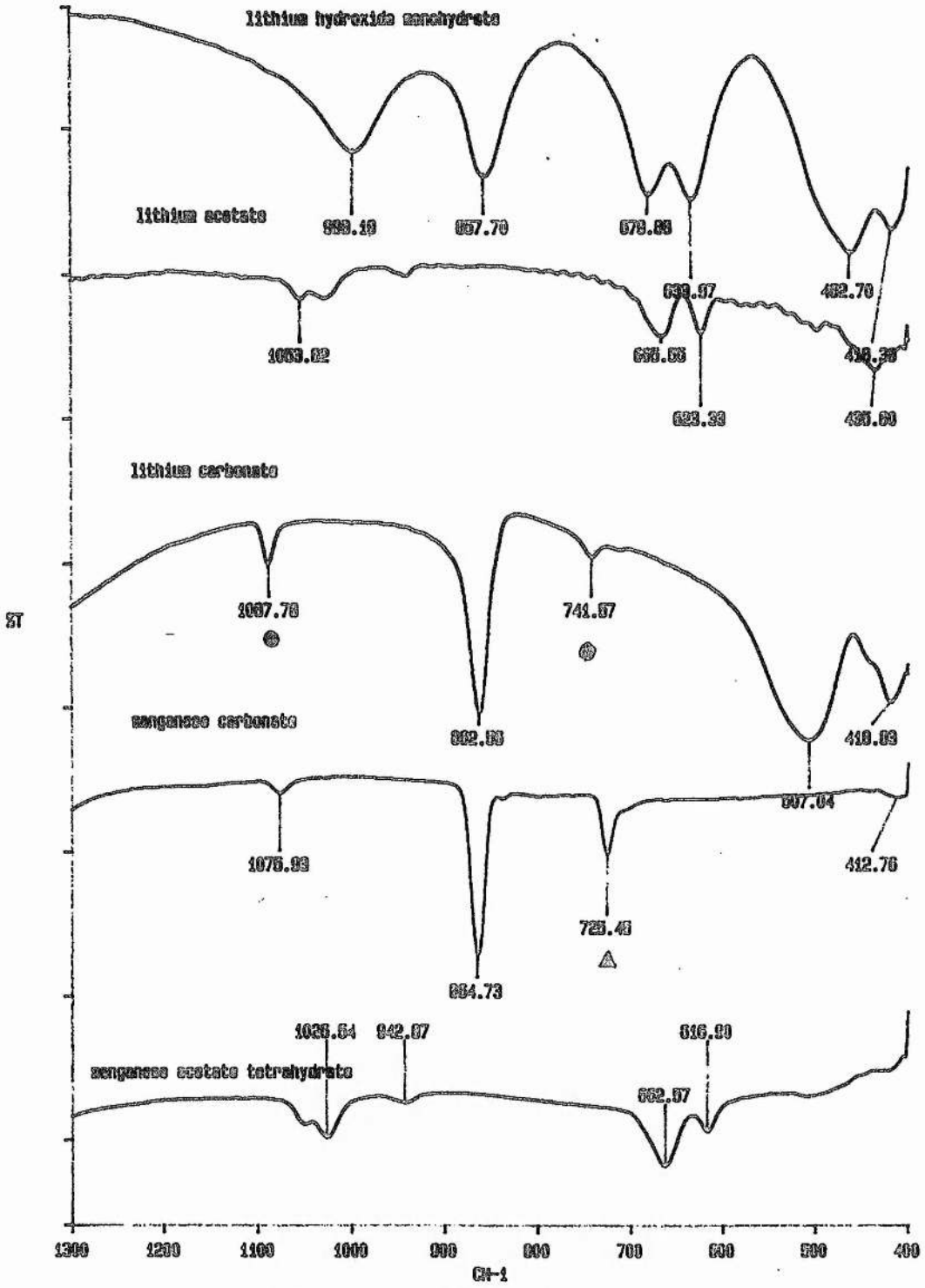

Appendix II FTIR spectra for $LiOH{\cdot}H_2O$, CH_3CO_2Li, Li_2CO_3, $MnCO_3$, and $Mn(CH_3CO_2)_2{\cdot}4H_2O$ compounds.